

**Western Australia School of Mines: Minerals, Energy and Chemical Engineering
Exploration Geophysics**

**On the Onset of Hydrothermal Convection in Porous Media in the
Presence of Creeping Faults: Numerical Stability Analysis and
Geological Applications**

Rebecca Li Jia Tung

**This thesis is presented for the Degree of
Doctor of Philosophy
of
Curtin University**

June 2018

Declaration

"To the best of my knowledge and belief this thesis contains no material previously published by any other person except where due acknowledgment has been made. This thesis contains no material which has been accepted for the award of any other degree or diploma in any university."



Signature:
(Rebecca Li Jia Tung)

Date: 05 July 2018

*To Jeremy, Margaret, Rachel, and Martin
For being my pillars of strength,
support, encouragement, and courage*

Abstract

In geothermal reservoirs, geological faults are known to play a major role affecting fluid flow patterns. Creeping faults are generally regarded as static at engineering timescales but can experience considerable deformation at geological timescales. Their frictional resistance to motion generates shear heating, and its impact on the temperature-sensitive fluid flow processes has not yet been fully understood. This thesis demonstrates the influence of creeping faults on the onset and pattern of hydrothermal convection, applied to geothermal reservoirs.

The effect of shear heating from creeping faults is shown to play a significant role in lowering the critical permeability conditions required for the onset of convection, suggesting that convection could be occurring in reservoirs containing such faults when other parameters suggest a purely diffusive solution without taking these faults into account. Shear heating is also found to play a role in altering steady state convective patterns, as heat can localise along the fault in unexpected ways.

A mathematical formulation to couple mechanical deformation with the classical formulation of hydrothermal convection is presented using the REDBACK geomechanics simulator. This code is used to build a framework which combines the mathematical rigour of analytical methods and the power of numerical simulators, through the implementation of a numerical bifurcation analysis tool based on the pseudo-arclength continuation method. The use of this workflow enables quantitative assessment of the conditions required for the onset of convection, and can be extended to determine the critical value governing the stability of any system of interest.

One particularly interesting result from this approach is the ambiguous definition of the onset of convection in specific cases. This challenges the misleading but widely accepted view that convection always starts at a precise threshold of parameter values. Perfect bifurcation curves are obtained for scenarios of symmetrical geometry. However in this thesis, it has been demonstrated that novel imperfect bifurcation curves are derived from non-symmetrical geometries. The comparison between the perfect and imperfect bifurcations shows that the onset of convection is subject to a visual analysis for cases of non-symmetrical geometries, where the steady state solution transforms asymptotically from convective to diffusive regimes.

Subsequently, the workflow presented above is applied to a specific fracture zone at Soultz-sous-Forêts with the aim of characterising its behaviour and impact on the surrounding fluid flow. It is established that purely hydrothermal (TH) processes are inadequate to fully characterise the system. The coupling of mechanical deformation with hydrothermal processes (THM) through shear heating is also found to be insufficient, which demonstrates the need to consider chemical processes and highlights the necessity for a fully coupled multiphysics approach. This study will benefit current and future considerations in the field of geothermal reservoir modelling.

Acknowledgements

I would like express my deepest gratitude to my supervisors Dr. Thomas Poulet, Dr. Manolis Veveakis, and Prof. Klaus Regenauer-Lieb for being awesome. I am extremely grateful for their constant support and guidance, and for shaping me into the person I am today. Thank you for always being (extremely) patient and welcoming me into your lives. I have gained much wisdom from our frequent 'meaning-of-life' conversations.

I greatly thank Dr. Sotiris Alevizos for his patience, guidance, and help with the understanding of theoretical mathematical concepts. Thank you for being my math guru and jazz buddy.

I also thank Dr. Max Peters for his invaluable contribution to my inquiries and data regarding Sultz-sous-Forêts, and for his hospitality towards me while I was at KIT.

I thank my Curtin supervisor Dr. Andrew Squelch for his support in facilitating my thesis from day one.

I wish to gratefully acknowledge the Australian Government Research Training Program Scholarship, and funding provided by the Australian Technology Network's Industrial Doctoral Training Centre (ATN-IDTC Scholarship), in partnership with the Commonwealth Scientific and Industrial Research Organisation (CSIRO). I also acknowledge the Pawsey Supercomputing Centre for its supercomputing support and resources.

I express my heartfelt gratitude to my family; Jeremy, Margaret, and Rachel for their unconditional love, support, encouragement, patience, and constant prayers.

I thank my friends and colleagues; Alex Guevel, Hadrien Rattiez, James Gilgannon, Jessie Chen, Lisa Tannock, Manman Hu, Martin Lesueur, Mustafa Sari, and Victor Boussange for being my guinea pigs when I stress bake, conference buddies, FunRoom shenanigans, mountain hikes, burgers, pizza, goon, and everything in between.

"Hop, supplies, and fly lice!"

Table of contents

List of figures	ix
List of tables	xiv
1 Introduction	1
1.1 A Review of Hydrothermal Convection	1
1.2 Hydrothermal Convection in Geothermal Settings	2
1.2.1 Numerical Modelling Approaches	3
1.3 Thesis Motivation	5
1.4 Key Objectives	6
1.5 Approach	6
1.6 Thesis Outline	7
2 Theory and Methods	10
2.1 Mathematical Model	10
2.2 Formulation for Classical Convection in Porous Media	13
2.2.1 Horton-Rogers-Lapwood Equations	13
2.3 Formulation for Convection in Faulted Reservoirs	15
2.3.1 Normalisation of Parameters	17
2.3.2 Definition of Dimensionless Terms	18
2.3.3 Linear Stability Analysis	20
2.3.4 Numerical Bifurcation Analysis	21
3 Numerical implementation	22
3.1 REDBACK	23
3.1.1 Code Structure	23
3.2 Implementation of the Pseudo-Arclength Continuation Method	27
3.2.1 System of Equations	27
3.2.2 MOOSE Scalar Kernel	28
3.2.3 Initial Guess and Iterative Calculations	29
3.3 Benchmark for numerical bifurcation algorithm: The Bratu Problem	30
3.3.1 Scaling Factor	32

TABLE OF CONTENTS

3.4	Mesh Sensitivity Analysis	33
3.4.1	Homogeneous Mesh	33
3.4.2	Mesh with Curved Layer	34
3.5	Effect of Geometry on Stability	34
4	TH: Classical Hydrothermal Convection in Rigid Porous Media	41
4.1	The Horton-Rogers-Lapwood Model: Benchmark Studies	42
4.1.1	Methodology	42
4.1.2	Non-Uniqueness of Results	43
4.1.3	Results	44
4.2	Effect of Fluid Compressibility	46
4.2.1	Discussion	46
4.3	Effect of Non-Homogeneous Geometry and Material Properties	48
4.3.1	Discussion	50
5	THM: Effect of Creeping Faults on Hydrothermal Convection	52
5.1	Model Construction	53
5.2	Shear Heating Changes the Onset of Convection	54
5.3	Shear Heating Changes the Pattern of Convection	60
5.4	Discussion	64
6	Towards THMC: A Soultz-sous-Forêts Case Study	66
6.1	Geological Setting and Geothermal Observations	66
6.1.1	Evidence of Mechanical Deformation	66
6.1.2	Evidence of Hydrothermal Convection	67
6.1.3	Convection in the Upper Reservoir	69
6.2	Compilation of Previous Models	69
6.2.1	Homogeneous vs. Fractured Approaches	70
6.3	Motivation and Aim for This Study	70
6.4	Materials and Methods	71
6.4.1	Model Parameterisation	71
6.4.2	Mesh Sensitivity Analysis	73
6.5	Results	74
6.5.1	TH Model	74
6.5.2	Fault Width and Permeability Analysis	75
6.5.3	THM Model	80
6.6	Discussion	82
6.6.1	Evidence of Hydrothermal Alterations	82
6.6.2	Towards a THMC-Coupled Approach in Geothermal Settings	82

TABLE OF CONTENTS

7	Conclusions and Future Outlook	85
	References	88
	Appendices	97
A	Copyright Consent	97

List of figures

1.1	Schematic flow chart of the thesis. The colours represent structural elements of the thesis; purple = introduction and providing a general overview, yellow = theory and model formulation, green = numerical aspects for code validation and implementation, blue = results and pilot case study of coupled multiphysics processes, pink = discussion and conclusion, providing a summary of the thesis.	9
2.1	Schematic representative elementary volume of a fully saturated porous medium, from a CT-scan sandpack (Imperial College Consortium On Pore-Scale Modelling, 2014). The rigid solid grains (A) are indicated in white and a single fluid phase (B) is in black.	11
2.2	a) Rayleigh-Bénard convection cells obtained from experiments (van Dyke and White, 1982), and b) Result of steady state convection cells with normalised temperature values obtained from a numerical simulator, REDBACK.	13
2.3	Schematic diagram of fault, showing the definitions of stresses. In this diagram, σ_h represents a horizontal, compressive stress, σ_n the normal stress, τ_n the deviatoric (shear) stress, and θ the angle of dip.	15
2.4	Conceptual evolution of the Nusselt number with respect to the Rayleigh number in the case documented by Bories (1987) , where the solid line indicates the steady state solution of convection, and the dotted line is the unstable branch. Convection occurs above the critical Rayleigh number Ra_c indicated by $Nu > 1$, and increases in strength for values of $Ra > Ra_c$. Another mode of convection is visible for larger values of Ra . The box highlights the focus of this study on the onset of convection.	20
3.1	Example input file solving only the diffusion of temperature in a generated square mesh. Input blocks can be added as the problem of interest increases in complexity.	26

LIST OF FIGURES

3.2	Schematic representation of the pseudo-arclength continuation scheme, marching along the arc-length S of the curve. At every iteration step (n) of the pseudo-arclength continuation algorithm (see Fig. 3.3), the initial guess (subscript IG) is computed from the previous two solutions at steps $(n - 1)$ and $(n - 2)$	28
3.3	Summary of pseudo-arclength continuation algorithm (Keller, 1979) for a continuation parameter λ . A Python wrapper is used to generate and run REDBACK simulations for all steady-state calculations. . . .	31
3.4	Bifurcation analysis on 1D Bratu problem, highlighting the critical turning point C_c	32
3.5	Stability plot displaying a result of high residual error of the λ -term, resulting in a nonsensical result and negative Lewis numbers. This result can be easily identified as unrealistic since theoretical solutions have been previously obtained (see Figure 17 in (Combarous and Bories, 1975), for instance).	33
3.6	Geometry (a) and graph showing the minimum number of elements needed for the mesh so that the solution does not vary (b).	35
3.7	Geometry (a) and graph showing the stability curves for varying mesh elements. Numerical convergence is reached at approximately 11,000 elements (b).	36
3.8	Geometry of varying amplitudes, ranging from a perfectly horizontal middle layer (a) to a larger amplitude of the middle layer (d).	38
3.9	Stability curves for varying amplitudes in the middle layer. A perfect bifurcation is observed for the layer of zero amplitude. However with increasing amplitude, stability curves diverge further away from this point.	39
3.10	Stability curves displaying examples of perfect and imperfect bifurcations, obtained from symmetrical and non-symmetrical geometries respectively. The grey dotted lines indicate changes in the behaviour of bifurcation curves, at which the onset could be identified. The location of point P1 is on the saddle-node of the unstable bifurcation curve, which translates to a steady state solution indicated by P2 . The gradient grey region is indicative of the probability at which the onset could be identified, with the darkest grey indicating the highest probability. As such, the solution for the onset of convection is rendered to a visual analysis of steady state results, and cannot be identified as a crisp value for non-symmetrical geometries. Points P3 and P4 are indicative of such points at which a user-defined onset could be resolved, noting the change in Le_c	40

LIST OF FIGURES

4.1	Steady state results illustrating non-uniqueness for the same value of Lewis ($Le = 3.14 \times 10^{-8}$), showing equivalent mathematical solutions. Temperature isotherms are represented by the faint white lines.	43
4.2	Benchmark results showing the expected values for Le_c in both scenarios, as listed in Table 4.2. Note the mirrored plots of Nu against Le compared to Fig 2.4.	45
4.3	Effect of fluid compressibility on the critical Lewis number. In Figure (c), an exponential relationship is identified for critical Lewis numbers with increasing fluid compressibility values. Fluid compressibility is not recognised to influence the onset of convection until past a certain critical value, which lies within the range of $10^{-4} < \beta_f^* < 10^{-3}$	47
4.4	a) Visualisation of the distribution of perturbed permeability in a model with folded geometry. A and B represent the material properties of the layer, which are listed in Table 4.3. b) Numerical stability analysis for the model, highlighting the critical Lewis number marking the onset of convection. In this particular case of a folded layer and small perturbations of permeability, the critical Lewis value is 1.09×10^{-7}	49
5.1	Modelling result of 3D faulted aquifer, showing the fault displacement and shear heating effect. The fault is moving under constant velocity loading with far-field isothermal boundaries at the top and bottom of the block, and a $10\times$ exaggeration is applied to illustrate the displacement in the fault. The box outlined in red is the representation of the 2D model used to study the onset of convection (see Section 5.2).	53
5.2	Impact of the Gruntfest number on onset of convection. a) Continuation curves for various Gr values. The critical permeability required for the onset of convection is lowered with increasing Gr values. b) Exponential fit of Le_c with Gr , providing an analytical solution where the Le_c can be obtained for any Gr value.	56
5.3	Simulation results showing the effect of shear heating in a conceptual reservoir with model dimensions $x=1000m$, $y=500m$ containing a horizontal fault 20m thick in the centre of the model (outlined in white). At the same critical Lewis number, a purely diffusive scenario becomes convective when shear heating is present ($Gr = 3e-03$) in the fault. The fluid and material properties used in this simulation can be found in Table 5.1.	57

LIST OF FIGURES

- 5.4 Map of Grunfest number as a function of the fault shear stress τ_n and yield stress for a reference strain rate of $\dot{\gamma}_0 = 10^{-16} s^{-1}$. Indicative values for this scenario are described in the text. Note that the range of yield stress values encompasses reservoir rocks as hard as consolidated sandstone (usually having a yield in shear of around 60 – 100 MPa) down to unconsolidated sand having a yield value of around 0.1 – 1 MPa. The white zone denotes the parameter space where $Gr = 0$, and the dotted line highlights the specific value $Gr = 1 \times 10^{-2}$, the maximum Gr used in Figure 5.2. 60
- 5.5 Convection patterns for a horizontal fault in the middle of the reservoir for Grunfest values of 0, 1×10^{-3} , 5×10^{-3} , and 1×10^{-2} respectively. The fault is outlined in white. Shear heating is seen to change steady state convection patterns, where the heat generated exceeds the given temperature boundary conditions and localises around the fault for higher Gr values. 61
- 5.6 Temperature profiles illustrating different convection patterns and normalised temperature isotherms with and without the presence of shear heating. The white gap between the reservoirs outline the fault of thickness 10m, and isotherms follow the temperature profiles. a) Convection profile for the case of no shear heating (i.e. $Gr = 0$). In this solution, the geometry of the fault is not acknowledged. b) Steady state temperature for $Gr = 1 \times 10^{-2}$. Note the non-symmetrical convection cells due to heat localising along the fault, as well as the upwelling plumes rising closer to the surface of the model. 63
- 6.1 Local temperature scale of Soultz; 1km scale, 500m depth. (Coloured version from (Bächler et al., 2003), personal communication.) 68
- 6.2 Temperature profile obtained from well GPK2, data source from Genter et al. (2010). 68
- 6.3 Conceptual mesh geometry used in this study. Three rock lithologies represented in the model are: the granitic host rock (A), fault network (B) with the centre of the fault zone marked in red, and granitic basement (C). Model dimensions are 5km in depth and 5.2km in length, indicated by dimensionless values. 72
- 6.4 Mesh sensitivity analyses performed on the mesh with geometrical dimensions listed in Table 6.1, plotted against the recorded temperature profile of GPK2. Numerical convergence of the solution is reached at approximately 11,000 elements. 74

LIST OF FIGURES

6.5	Temperature profiles obtained using values provided in Table 6.1. a) Steady state simulation result using designated mesh geometry, displaying normalised temperature values and isotherms in the entire domain. Temperature values are taken along a digitised well bore, represented by the black line. b) Temperature profile of (a) plotted against GPK2 showing an adequate fit.	76
6.6	Temperature profiles of decreasing permeability are plotted against the original well data of GPK2 (in black). In this scenario, the fault width is fixed at 370m and temperature data points are taken at the centre of the fault (see Figure 6.5a). With decreasing permeability, it can be observed that the behaviour of temperature tends towards the standard geothermal gradient, matching that of the [black] lower branch.	77
6.7	Relationship of varying fault width to required permeability for sustainable convection. Data points obtained from simulations are indicated in dark blue and approximated permeability values are displayed in light blue, obtained using a power law relationship. Trendline and R-squared coefficient are displayed on the graph.	79
6.8	Temperature profiles of varying fault widths and permeabilities. GPK2 temperature profile is displayed in black, and it is noted that the higher permeabilities required for narrower fault zones are numerically impossible to attain without upwinding schemes.	81

List of tables

1.1	This table lists several numerical codes used in geothermal reservoir modelling.	4
2.1	The terms IMP and FRE for the pressure boundary conditions (BC) correspond to impermeable (Neumann BC) and constant pressure (Dirichlet BC), where CONST and CHF are constant temperature (Dirichlet BC) and constant heat flux (Neumann BC) respectively. It can be observed that different Ra_c exist from varying the BC of temperature and pressure.	15
3.1	Mesh sensitivity analysis of the numerical continuation algorithm for the 1D Bratu problem (Korkine, 1869). The number N of mesh elements is varied and the value of the critical turning point C_c^N is compared with the reference solution $C_c^{ref} \simeq 3.513830719$ (Mohsen, 2014).	30
4.1	Table of input parameters for Scenarios 1 and 2, solving the classical case of hydrothermal convection. Both scenarios have identical geometries, fluid and solid properties. However, the boundary conditions for Scenario 2 vary slightly; this is shown in blue. This table lists the dimensionless values used in REDBACK, which are then converted to its corresponding real values. The fluid viscosity and solid specific heat values are defined in the Lewis number and the same real values are used in the simulations.	42
4.2	Benchmark table, adapted from Nield and Bejan (2013), showing the boundary conditions for temperature T and pore pressure P at the upper (subscript u) and lower (subscript l) boundaries, along with the corresponding critical values of Ra_c for the incompressible case. IMP = impermeable; FRE = free; CON = conducting. The terms free and conducting are equivalent to constant pressure and constant temperature (e.g. Dirichlet boundary conditions), respectively. The critical Lewis values Le_c for the compressible case can be translated back to Rayleigh numbers, listed in the column 'compressible Ra_c '.	45

LIST OF TABLES

4.3	Table of input parameters for the example of varying permeability and material properties. The solid properties are identical in all layers, except for permeability. The permeability value of Layer A is converted from Le_c	50
5.1	Table of input parameters for the example of observing the effect of shear heating in a horizontal fault, listing the real values which correspond to the dimensionless values used in REDBACK. The real values for the viscosity of the fluid and specific heat values of both the fluid and solid materials are used in the simulations. The solid properties are identical in all layers, except for permeability which is varied in the study.	54
5.2	Table of indicative parameters for the scenario produced in the map of Gruntfest with a reference strain rate of $\dot{\gamma}_0 = 10^{-16} s^{-1}$ (see Figure 5.4).	59
5.3	Table of input parameters for the example of observing the effect of shear heating in a reservoir containing a dipping fault, listing the real values which correspond to the dimensionless values used in REDBACK.	62
6.1	Table of parameters used for the best fitting temperature profile, matching that of GPK2 (see Figure 6.5).	73
6.2	Table displaying data points obtained from simulations (black) and calculated permeability values (grey) using a power law fit. Fault width values range from what was used in the model (370m) to realistic values observed in well logs (8m). Permeability values obtained for widths below 100m are unrealistic.	79
6.3	Table of mechanical parameters used to calculate values for Gruntfest. Values used in this study are representative and an averaged from those documented in literature.	80

Chapter 1

Introduction

1.1 A Review of Hydrothermal Convection

Hydrothermal convection plays an essential role in geological settings, transporting heated fluids at depth up to the surface. These fluids often contain precious metals and minerals which can be precipitated along faults, and the heat from these fluids could be used for energy generation. The phenomenon of hydrothermal convection has been extensively studied since the early 1900's and is driven by the changes of fluid buoyancy with temperature. First observed and explained by [Bénard \(1901\)](#), [Rayleigh \(1916\)](#), and [Jeffreys \(1926\)](#), the driving parameters of the system are expressed through the Rayleigh number (Ra). The Rayleigh number is a dimensionless group which contains information of the boundary conditions, coefficients of volume expansion, thermal conductivity, kinematic viscosity, and the height (or depth) of the layer of interest ([Rayleigh, 1916](#)). The onset of convection is predicted to occur past a critical Rayleigh number (Ra_c), and has been investigated in diverse fields including linear and non-linear problems, stability regimes dependent on material properties and boundary conditions, and convection in varied geometrical environments ([Elder, 1967](#); [Horton and Rogers, 1945](#); [Lapwood, 1948](#); [Morrison, 1947](#); [Rayleigh, 1916](#)), amongst others. A comprehensive review can be found in [Nield and Bejan \(2013\)](#), for instance. This onset of convection was identified as an instability arising from varying temperature gradients; hence the evolution of convection can be studied using stability analyses. In particular, linear stability analyses have been extensively used to analytically pinpoint the critical Rayleigh numbers at which convection is predicted to occur for very specific geometries and boundary conditions (eg [Bories, 1987](#)).

In the last century, the best approaches to investigate the onset and behaviour of convection included comprehensive analytical equations and laboratory experiments ([Bénard, 1901](#); [Elder, 1967](#); [Horton and Rogers, 1945](#); [Jeffreys, 1926](#); [Lapwood, 1948](#); [Morrison, 1947](#); [Rayleigh, 1916](#)). However, due to mathematical limitations, such investigations were mostly limited to simplified equations, simple geometries, and uniform material properties, and were hence unable to account for the complexities of

1.2 Hydrothermal Convection in Geothermal Settings

realistic geological systems (Horton and Rogers, 1945). Building on previous analytical discoveries, the availability of increased computing power and in recent years and exponential use of numerical methods have led to a shift in the way that convection is investigated.

1.2 Hydrothermal Convection in Geothermal Settings

Advances in computer technologies and data collection techniques have allowed the incorporation of more extensive and representative geological and geophysical data into numerical models. The results of these simulations contribute to a better understanding of the evolution of hydrothermal convection in the context of complex geological systems. In particular, hydrothermal convection plays a significant role in geothermal reservoirs as it can be one of the main drivers of heat and fluid flow under certain conditions (eg Pribnow and Schellschmidt, 2000).

Whilst hydrothermal convection is preponderant in hot sedimentary aquifers (HSA), it could also be present in other geothermal systems. Such systems can be classified under three main categories: conventional geothermal (volcanic) systems, enhanced geothermal systems (EGS), and hot sedimentary aquifers. Conventional geothermal environments are usually located in volcanic, porous media. These systems often experience high temperatures and rely on pre-existing permeable pathways which allow easy access to hot fluid/steam for energy generation. Some examples of natural volcanic geothermal sites include New Zealand, Iceland, and Hawaii.

Enhanced geothermal systems (EGS) are different to conventional geothermal systems as they rely on a mechanical interaction with the reservoir where permeability pathways are engineered to access heat from the host rock. Permeability creation and sustainability are often obtained by hydraulic stimulation, in contrast to the classical reservoirs where heat and mass extraction rely primarily on pre-existing permeable pathways. EGS can be found in most parts of the world including China, France, Germany, Indonesia, Philippines, Switzerland, United States, and are presumably the most common setting in geothermal systems worldwide. Unlike EGS and volcanic systems, hot sedimentary aquifers are often located in naturally thick, porous sedimentary basins. These systems rely mostly on natural fluid flow processes which carry heated fluids up to the surface of the porous aquifer.

In all settings, geothermal reservoirs rely on pre-existing permeable pathways which allow natural heat and mass transfer. Initially, convection studies started with the approach of modelling a purely physical hydrothermal process. The increase of information from geophysical surveys and geological field data resulted in the extension of this approach to include more physical processes, for instance the phenomenon of double diffusive convection. This form of convection is driven by different density gradients and can be applied to the interaction between fresh and saline fluids, for

1.2 Hydrothermal Convection in Geothermal Settings

example (Charrier-Mojtabi and Mojtabi, 2005; Elder, 1967; Huppert and Turner, 1981; Stommel et al., 1956).

In addition to varying density gradients, chemical reactions have been observed to play a vital role particularly in geothermal reservoirs. Such systems can often experience high pressures and temperatures, resulting in the alteration of mechanical properties of the reservoir. The extreme temperature and pressure conditions can cause dissolution and precipitation of existing and new minerals, thus creating new porosity and permeability channels in the host rock. Some example sites of highly altered geothermal fields include Chile, Iceland, Italy, Japan, New Zealand, and California and Wyoming in the United States (Browne, 1978).

Additional physical processes which could be considered to better explain the geological and geophysical data, include: varying density gradients, chemical reactions, and mechanical deformation. However, the incorporation of these physical processes coupled with hydrothermal convection can be extremely complex and challenging to solve using analytical methods. These difficulties have been partly overcome by advances in computing technologies.

1.2.1 Numerical Modelling Approaches

Technological advancements have led to the possible incorporation of more realistic material properties and boundary conditions into numerical models. These data have been able to provide more information of the in situ geological structures and conditions over multiple length-scales, obtained from geological field data, geophysical surveys, laboratory experiments, and micro-CT data. The exponential growth of data has led to the simulation of multiscale multiphysics with more realistic geometry and material properties.

To simulate such complex processes, many numerical simulators have been developed which incorporate multiphysical couplings, namely thermo-hydro-mechanical-chemical (THMC) processes. These numerical simulators need to be calibrated and validated against analytical solutions, field data, and laboratory experiments. As a result, international initiatives such as DECOVALEX were formed to provide numerical benchmarks for THMC processes in geological systems (Tsang et al., 2008). Based on the corresponding advantages and limitations of various numerical implementations, several THMC implementations have been developed. For example, hydrothermal flow in porous media is commonly modelled using the finite difference/volume method (e.g. TOUGH2, (Pruess, 1991; Pruess et al., 1999), ECLIPSE (Schlumberger, 2018)), whilst mechanical deformation usually involves the finite element method (e.g. OPEN-GEOSYS, (Kolditz et al., 2012)).

In particular, the widespread application of geothermal reservoir modelling has contributed to the formation of the International Partnership for Geothermal Technologies (IPGT) in 2008, involving modelling teams from participating countries including

1.2 Hydrothermal Convection in Geothermal Settings

Summary of Numerical Codes used in Geothermal Modelling					
Name	Author(s)	Numerical Method	Hydrothermal Processes (TH)	Mechanical Deformation (M)	Reactive Transport (C)
FEFLOW	Diersch (2013)	FE	✓		✓
MODFLOW	Hughes et al. (2017); McDonald and Harbaugh (1988)	IFD	✓		
HYDROTHERM	Hayba and Ingebritsen (1994); Kipp et al. (2008)	FD	✓		✓
SHEMAT	Bartels et al. (2003); Clauser and Bartels (2002)	FD	✓		✓
FRACTURE	Kohl et al. (1995b)	FE	✓	✓	
FALCON	Podgorney et al. (2010, 2011); Xia et al. (2016)	FE-DEM	✓	✓	
FEHM	Bower and Zyvoloski (1997); Zyvoloski et al. (1988, 1997)	FE	✓	✓	
TOUGH2	Pruess et al. (1999)	IFD	✓	✓	
OPENGEOSYS	Kolditz et al. (2012)	FE	✓	✓	

Table 1.1 This table lists several numerical codes used in geothermal reservoir modelling.

Australia, Iceland, New Zealand, Switzerland, and the United States. As a result of this initiative, along with many others, various codes incorporating fluid flow processes with mechanics and chemical reactions have already been developed or are under development. A compilation is summarised in Table 1.1, modified after IPGT (2012).

The numerical simulators listed in Table 1.1 are state-of-the-art codes, often industry standards. They are capable of incorporating realistic 3-dimensional (3D) geometries, coupling multiple physical processes, and can be computationally efficient and scalable. These codes were developed particularly to understand specific problems related to geothermal reservoirs. For example, some codes focus on the reactive transport of constituents coupled with fluid flow (SHEMAT, TOUGH2, TOUGHREACT), while others investigate flow in predominantly fractured reservoirs (FRACTURE, FALCON), and have all been invaluable in contributing to the understanding of multiphysics in geothermal reservoirs.

The abundance of data, however, can cause challenges if only processed in a retrospective manner. To resolve this, prospective studies can help understand the underlying physics with the aim of identifying the driving parameters of the system. Specifically, numerical simulators which couple chemical and mechanical processes with hydrothermal fluid flow exist, but the full impact of multiphysics on hydrothermal convection has yet to be fully understood.

1.3 Thesis Motivation

The motivation of this research is to understand the fundamental processes that govern multiphysics in geothermal settings by identifying and quantifying the critical parameters characterising the reservoir towards extreme conditions (high ambient temperature, high pressure, and chemical reactions).

Hydrothermal convection is an interesting example where multiphysical processes interact in a complex manner. In particular, convection cells have been shown to be constrained by geological features such as faults and fracture zones (Reid et al., 2012), which are characteristic in HSA basins. These faults can also experience deformation and could be seen as steadily creeping when considered at geological timescales. The resistance to motion generates shear heating (Regenauer-Lieb and Yuen, 2003; Scholz, 1980; Yuen et al., 1978), and is expected to influence the overall heat equilibrium of the system. However, the interaction between shear heating and other processes (e.g. heat and mass transport) in the reservoir has not yet been studied in depth, and could potentially provide interesting outcomes. In addition to mechanical deformation, heated fluids can precipitate and/or dissolve minerals along faults, depending on the composition of the fluid and ambient temperature conditions.

Hence, to understand the fundamental processes which govern THMC processes in hot sedimentary aquifers, a workflow is required which incorporates geophysical and geological field data into a numerical model and a fully coupled THMC solution must be sought. This point has been identified in 2012, when the IPGT issued a report detailing the research and development plans for the future of geothermal modelling by the year 2020: *"to have a fully coupled THMC reservoir simulation code to describe the complex non-linear interactions and feedbacks associated with multiphase fluid flow, energy transport, regional- and local-scale geomechanical deformation (and fracturing), and geochemical interactions between the working fluid and host reservoir rock; all at highly variable timescales."* (IPGT, 2012).

From this vision came an abundance of numerical simulators (see Section 1.2.1 with the ability to couple physical processes not only in a sequential manner, but also in a tightly coupled way. However, the mechanical and chemical processes in geothermal settings are particularly complex and have not yet been fully understood. Readily available information provided in various scales by geophysical and geological field data, laboratory experiments and micro-CT scans have contributed to an abundance of information ("Big Data"). The ability to determine the key driving parameters of a system can be promoted by efficiently processing and analysing this wealth of data.

1.4 Key Objectives

The main objective of this thesis is to understand the impact of creeping faults on the onset and behaviour of hydrothermal convection, applied to geothermal settings. In numerically coupled THMC systems, considerable ambiguities are present due to subsurface heterogeneity, potentially stemming from geological conditions, the physics of the processes considered, or numerical implementations. To date, the onset of convection in realistic reservoirs is typically determined through a parameter sensitivity analysis where different values of permeability are tested in a given reservoir, for a given scenario. Uncertainty quantifications can reduce both computational and realistic ambiguities by determining outcome probabilities. Techniques such as reduced-order modelling for example, allow uncertainty models to be obtained in a small amount of time whilst retaining accuracy (Degen et al., 2017). The issue with this methodology is that it still takes a prolonged time for convection to establish and reach a steady state, particularly when the system is close to criticality, as demonstrated in (Reid et al., 2012, , Figure 5.10), for example. Thus it is impossible to determine if the parameters chosen are below the convective threshold, or if the simulation suffered from insufficient running time. However, this problem can be resolved using mathematically rigorous methods through the use of analytical linear stability analyses (LSA). Nonetheless, these analytical approaches have limitations and using such analyses on realistic geometries and inhomogeneous material properties can be extremely laborious.

The second key objective is to develop a tool which harnesses the strengths of both analytical and numerical methods, by integrating the mathematical rigour of the analytical stability analysis with the power of multiscale, multiphysics numerical simulators. This will allow the identification of key parameters which contribute to the criticality of a given system, and can be extended to study more complex geometries and material properties. In particular, the impact of creeping faults on the onset of convection in faulted reservoirs is first investigated.

1.5 Approach

The approach of this thesis contributes to the goal of numerically fully coupled THMC simulators to aid modelling and optimising geothermal reservoirs (IPGT, 2012).

When the processes occurring at long geodynamic timescales are coupled with the short (engineering) timescale processes of the geothermal reservoir, explicit THMC-feedback processes are considered in the evolution of material properties. The multiscale feedbacks between chemistry, fluid flow, temperature, and mechanics can give rise to different critical localisation phenomena and can be characterised by dimensionless numbers expressing the ratios of the rates of competitive physical processes.

1.6 Thesis Outline

In this thesis, the focus is particularly on the Lewis and Gruntfest numbers, which describe the ratio of heat and mass transfer, and the mechanical dissipative work present the system respectively. At critical conditions, mechanical localisation phenomena can manifest themselves as shear and/or fracture zones, which can have a fundamental influence on the fluid dynamics processes in the reservoir. In this thesis, I have chosen to first understand the fundamental processes occurring at elevated temperatures and pressures under specific tectonic stress regimes.

The numerical tool used in this thesis is REDBACK, a geomechanical simulator specifically designed to study tightly coupled multiphysical effects in various geological settings (Poulet et al., 2016; Poulet and Veveakis, 2016). Building on the flexibility and power of numerical simulators, a bifurcation analysis using a pseudo-arclength continuation method is implemented and benchmarked in REDBACK. This method preserves the rigorous mathematical approach, and can be applied to determine the stability of any given system.

1.6 Thesis Outline

This thesis is organised into seven chapters, graphically illustrated in Figure 1.1. It is structured as follows:

Chapter 2 presents the theory and methods for the classical derivation and formulation of equations for hydrothermal convection in porous media, along with the new approach used in this thesis. The underlying theory and model assumptions used to characterise the system for convection in mechanically-deforming porous media are discussed in this chapter, along with the derivation of equations, definition of dimensionless groups, and the need for a numerical stability analysis.

Chapter 3 contains the implementation of the system of equations defined in Chapter 2 and the numerical bifurcation method into the geomechanical simulator, REDBACK. To determine the stability of a system, a bifurcation analysis using a numerically-assisted technique - a pseudo-arclength continuation method - is implemented and benchmarked. Various sensitivity analyses exploring the effects of mesh discretisation and geometry on the onset of convection are also discussed.

Chapter 4 utilises the equations described in Chapter 2 with the new numerical bifurcation tool to derive results of hydrothermal convection in rigid porous media. The methodology of the workflow is discussed, acknowledging potential non-unique results which could be obtained. Furthermore, the effects non-homogeneous geometry, material properties, and fluid compressibility are investigated with respect to the critical value required for the onset of convection.

Chapter 5 highlights the effect of shear heating on the onset and pattern of convection, describing the physical model and assumptions used in this investigation. The

1.6 Thesis Outline

results and proposals for future work are discussed with implications to geothermal engineering operations.

Chapter 6 builds on the workflow and results of Chapter 5 and applies the current approach to a case study of Soultz-sous-Forêts. The objective of this chapter is to investigate a specific fracture zone and its influence on the surrounding fluid flow.

Chapter 7 concludes the thesis with the key findings obtained from Chapters 4, 5, and 6. This chapter highlights new knowledge on the impact of creeping faults in reservoirs where hydrothermal convection is present, as well as the implementation of a numerical bifurcation method. Results and suggestions for future work are discussed in the context of impacting geothermal energy production.

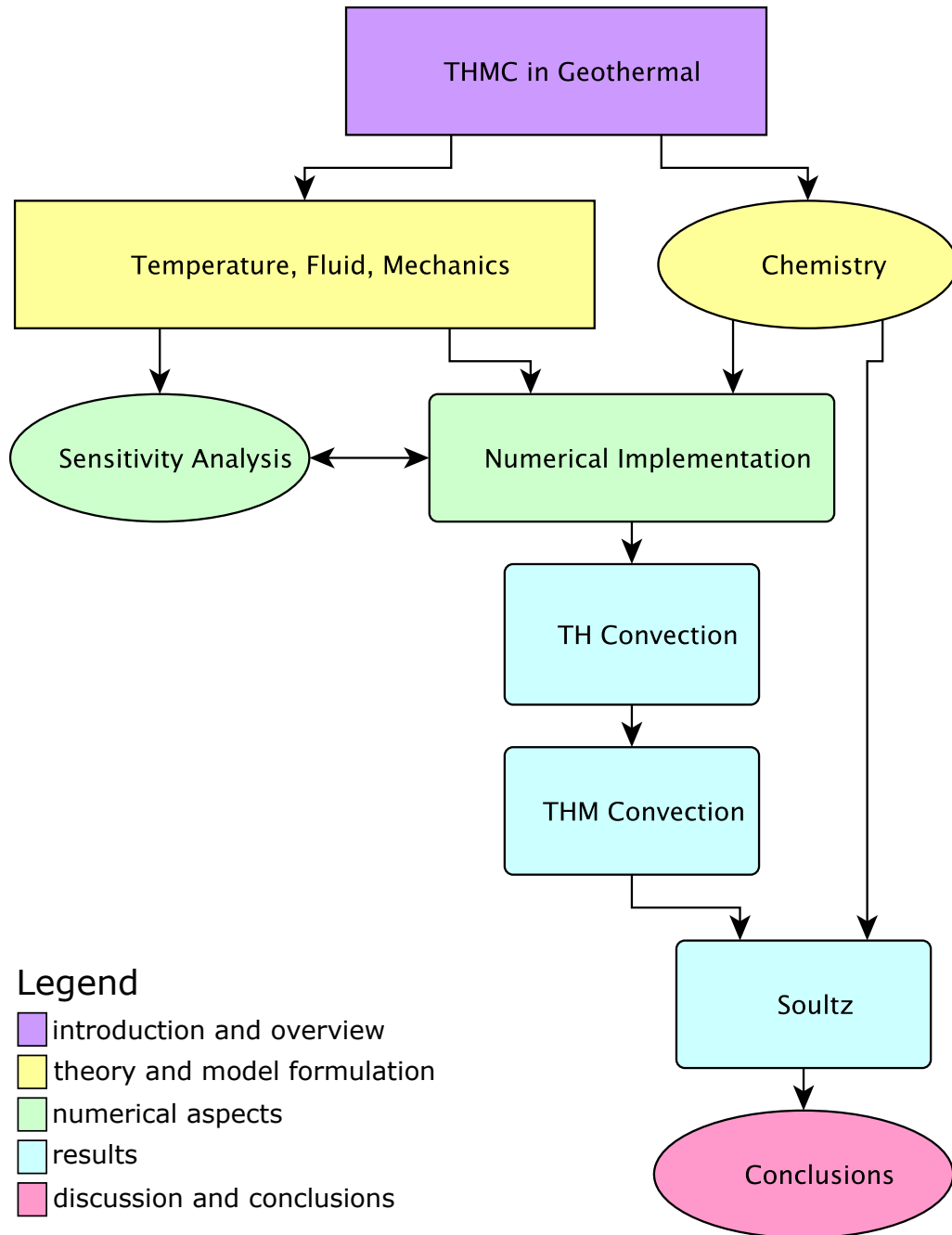


Fig. 1.1 Schematic flow chart of the thesis. The colours represent structural elements of the thesis; purple = introduction and providing a general overview, yellow = theory and model formulation, green = numerical aspects for code validation and implementation, blue = results and pilot case study of coupled multi-physics processes, pink = discussion and conclusion, providing a summary of the thesis.

Chapter 2

Theory and Methods

The aim of this thesis is to investigate the behaviour and response of hydrothermal convection in geological reservoirs hosting creeping faults. In geothermal settings, hydrothermal convection is a particularly important phenomena as it can be a major driver of heat and fluid transport which can be utilised for energy generation. Geothermal reservoirs often encompass highly fractured porous media, which allow heated fluid to flow. At geological timescales, such reservoirs can be subjected to considerable deformation, in which faults can deform at constant creep. The fault's frictional resistance to motion generates shear heating, which has been documented to play a significant role in various geological settings, ranging from crustal faults (e.g. [Lachenbruch and Sass, 1980](#); [Leloup et al., 1999](#); [Regenauer-Lieb and Yuen, 1998](#); [Sibson, 1982](#)) to Saturn's moon ([Nimmo et al., 2007](#)). However, the effects of shear heating has not yet been fully investigated in geothermal environments. Heat generation from creeping faults can potentially impact the heat equilibrium of the system ([Tung et al., 2017](#)). Specifically of interest is the influence of shear heating on the onset of hydrothermal convection, applied to geothermal reservoirs.

This chapter presents the physical and mathematical model used to simulate hydrothermal convection in deformable porous media. It then compares the classical derivation of convection in porous media with the formulation used in this thesis.

2.1 Mathematical Model

The mathematical model describing the problem of hydrothermal convection in the presence of faults comprises the standard governing laws of physics (momentum, mass, energy and entropy balance), together with appropriate constitutive laws for the materials involved. In order to derive the system of equations, a representative elementary volume (REV) is defined of a fully saturated porous medium consisting of a solid skeleton A , saturated by a single fluid phase B (see [Figure 2.1](#)).

2.1 Mathematical Model

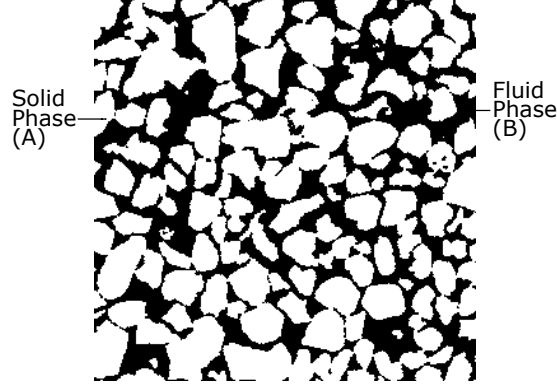


Fig. 2.1 Schematic representative elementary volume of a fully saturated porous medium, from a CT-scan sandpack ([Imperial College Consortium On Pore-Scale Modelling, 2014](#)). The rigid solid grains (A) are indicated in white and a single fluid phase (B) is in black.

Let the rock be subject to stress (σ) and temperature (T) conditions, where Terzaghi's decomposition of the stress tensor $\sigma_{ij} = \sigma'_{ij} - p_f \delta_{ij}$ is introduced into an effective stress part σ'_{ij} and the pore fluid pressure p_f (δ_{ij} being Kronecker's delta). Neglecting inertia terms at equilibrium, the momentum balance for the mixture reads where the notation of implicit summation is used:

$$\partial_j \sigma'_{ji} - \partial_j p_f \delta_{ji} + \bar{\rho} g_i = 0 \quad (2.1)$$

where $\partial_j \sigma'_{ji}$ is the divergence of effective stress, $\bar{\rho}$ the density of the mixture, and g_i the acceleration of gravity vector.

In order to define the density of the mixture $\bar{\rho} = \rho_1 + \rho_2$ in a porous medium, partial densities are introduced for the solid (1) and fluid phase (2),

$$\begin{aligned} \rho_1 &= (1 - \phi) \rho_s \\ \rho_2 &= \phi \rho_f \end{aligned}$$

where ϕ is the porosity, and $\rho_{s,f}$ are the densities of the solid skeleton and fluid, respectively. The mass balance equation per phase is expressed as

$$\partial_t \rho_a + \partial_k \rho_a v_k^{(a)} = 0 \quad (2.2)$$

where $a = 1, 2$ for solid and fluid phase, respectively.

An equation of state is assumed relating the densities with the pore fluid pressure p_f and temperature T :

$$\frac{d\rho_i}{\rho_i} = \beta_i dp_f - \lambda_i dT \quad (2.3)$$

where β_i the compressibility, λ_i the thermal expansion, ρ_i the density of the constituent i where $i = f, s$. It is acknowledged that the properties of water and steam are depen-

2.1 Mathematical Model

dent on the conditions of temperature and pressure with more complex dependencies (IAPWS, 2007), however within the scope of this thesis, scenarios are restricted to simple cases thus adopting a linearised expression for the fluid density is sufficient (Tung et al., 2017): $\rho_f = (1 + \beta_f(p_f - p_0) - \lambda_f(T - T_0))$.

A constitutive model is taken for the fluid migration written for the filtration velocity using Darcy's law Coussy (2003):

$$q_k^{filter} = \phi(v_k^{(f)} - v_k^{(s)}) = -\frac{k_\pi}{\mu_f} (\partial_k p_f + \rho_f g_i \delta_{i3}) \quad (2.4)$$

where $v_k^{(f)}$ is the fluid velocity, $v_k^{(s)}$ the solid velocity, k_π the permeability and, μ_f the fluid viscosity.

Based on these assumptions, the mass balance equation for the mixture reads:

$$\bar{\beta} \partial_t p_f = -\partial_k q_k^{filter} + \bar{\lambda} \partial_t T - \beta_{con} \partial_k p_f + \lambda_{con} \partial_k T - \dot{\epsilon}_{kk} \quad (2.5)$$

where $\bar{\beta} = (1 - \phi)\beta_s + \phi\beta_f$, is the compressibility of the mixture, $\bar{\lambda} = (1 - \phi)\lambda_s + \phi\lambda_f$ the thermal expansion of the mixture, while $\beta_{con} = \left[(1 - \phi)\beta_s v_k^{(s)} - \phi\beta_f v_k^{(f)} \right]$ and $\lambda_{con} = \left[(1 - \phi)\lambda_s v_k^{(s)} + \phi\lambda_f v_k^{(f)} \right]$ are the expressions of compressibility and thermal expansion coefficients respectively appearing in the convective terms of the equation. The total volumetric strain rate of the solid phase is expressed by the term $\dot{\epsilon}_{kk} = \dot{\epsilon}_{kk}^e + \dot{\epsilon}_{kk}^p = \partial_k v_k^{(1)}$, which is decomposed into elastic ($\dot{\epsilon}^e$) and plastic ($\dot{\epsilon}^p$) parts.

The derivation of the final governing law combines the energy-entropy balance equation with Fourier's law of thermal conduction to give:

$$\overline{\rho C_p} (\partial_t T + \bar{v}_k \partial_k T) = \kappa \partial_{ii}^2 T + \chi \sigma'_{ij} \dot{\epsilon}_{ij}^p \quad (2.6)$$

where \bar{x} denotes the property x of the mixture, where in this case, $\overline{\rho C_p}$ is the mixture average of the product of density and heat capacity, $\bar{v}_k = \left[(1 - \phi)\rho_s v_k^{(s)} + \phi\rho_f v_k^{(f)} \right] \bar{\rho}^{-1}$ the mixture's barycentric velocity, and κ the mixture's thermal conductivity. The last term, $\chi \sigma'_{ij} \dot{\epsilon}_{ij}^p$, represents the mechanical dissipation with χ expressing the part of the mechanical work which is converted into heat. As such, the Taylor-Quinney coefficient χ lies between 0 (when none of the mechanical work is converted into heat) and 1 (when all of the mechanical work is converted into heat) and represents the aforementioned ratio. This source term in the energy equation is usually very low and can be neglected, except in areas of localised deformation such as faults.

The final system of equations describing hydrothermal convection in faulted environments consists of Equations (2.1, 2.5, 2.6), together with appropriate constitutive laws for the mechanical deformation relating the strain rate to the stress tensor. In the following sections, two cases of hydrothermal convection will be explored, first

2.2 Formulation for Classical Convection in Porous Media

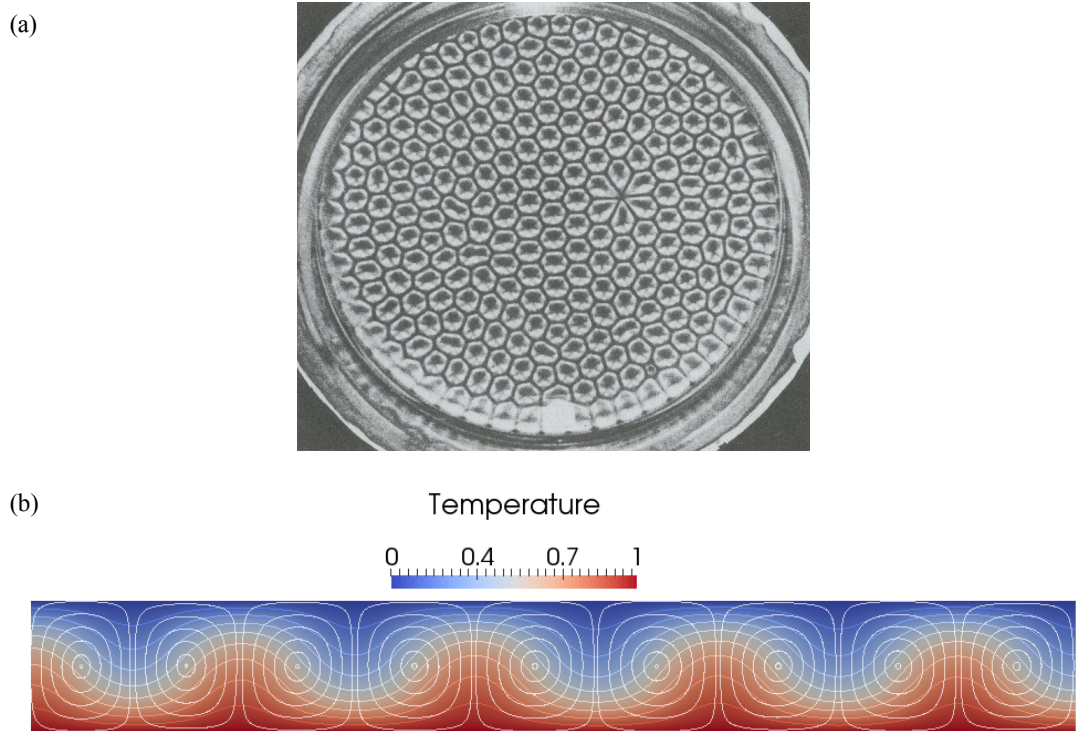


Fig. 2.2 a) Rayleigh-Bénard convection cells obtained from experiments (van Dyke and White, 1982), and b) Result of steady state convection cells with normalised temperature values obtained from a numerical simulator, REDBACK.

retrieving the classical formulation in the absence of mechanical deformation, and later introducing mechanical deformation in a given class of faulted environments.

2.2 Formulation for Classical Convection in Porous Media

Hydrothermal convection has been studied since the early 1900's and is driven by the change of buoyancy of fluid with temperature. The phenomenon was first observed and explained by Bénard (1901), Rayleigh (1916), and Jeffreys (1926), and a comprehensive review of the subject can be found in Nield and Bejan (2013) for instance. Figure 2.2 illustrates convection cells obtained in experiments and results from numerical modelling. The critical value of the driving parameter for the system, known as the critical Rayleigh number (Ra_c), contains information of the boundary conditions, coefficients of volume expansion, thermal conductivity, kinematic viscosity, and the height (or depth) of the layer (Rayleigh, 1916).

2.2.1 Horton-Rogers-Lapwood Equations

One of the best known models to describe hydrothermal convection in porous media is the Horton-Rogers-Lapwood system of equations, where the Boussinesq approximation, incompressible fluid and solid ($\beta_f = \beta_s = \bar{\beta} = 0$), and rigid solid skeleton ($v_k^{(s)} = 0$)

2.2 Formulation for Classical Convection in Porous Media

are assumed (Horton and Rogers, 1945), for which β_f is the fluid compressibility, β_s the solid compressibility, and $\bar{\beta}$ the compressibility of the mixture. The Boussinesq approximation assumes that density is only prevalent in the buoyancy term, therefore the temperature- and pressure-dependent density is replaced by a constant density term. In this case, Equations (2.1, 2.5, 2.6, 2.4) reduce to the classical equations for hydrothermal convection:

$$\begin{aligned} \partial_k v_k^{(f)} &= 0 \\ v_k^{(f)} &= -\frac{k_\pi}{\phi \mu_f} [\partial_k p_f + \rho_f g_i \delta_{i3} - \rho_f \lambda_f (T - T_0) g_i \delta_{i3}] \\ \overline{\rho C_p} (\partial_t T) + (\rho C_p)_f (v_k^{(f)} \partial_k T) &= \kappa \partial_{ii}^2 T \end{aligned} \quad (2.7)$$

where T_0 is a reference temperature.

In order to observe the behaviour of hydrothermal convection, the above equations can be normalised, leading to the introduction of the Rayleigh number (Ra), a dimensionless number encompassing properties from the fluid, solid matrix, as well as geometrical considerations and boundary conditions. This number, specific to the system of equations solved, is typically used to determine the occurrence of convection in a rigid porous media. Specifically, the definition of the Rayleigh number used to describe a scenario consisting of a horizontal two-dimensional homogeneous block is:

$$Ra = \frac{k_\pi \Delta T g H \lambda_f \rho_0^2 C_m}{\alpha \mu_f} \quad (2.8)$$

where k_π is the permeability, ΔT the temperature difference between the top and bottom of the geometry considered, g the gravitational constant, H the thickness of the model, λ_f the thermal expansion of the pore fluid, ρ_0 the reference fluid density, C_m the specific heat capacity of the mixture, α the thermal conductivity of the fluid-saturated medium, and μ_f the viscosity of the fluid. Considering all the parameters defined in the Rayleigh number, permeability is of particular interest as it can vary by several orders of magnitude in a given system. It is the most poorly constrained parameter in reservoir scale applications and as a result, could arguably be considered as the most influential parameter in the Rayleigh number definition.

The value of Ra is dependent on the geometry and boundary conditions of the problem considered, and the critical Rayleigh number (Ra_c) defines the value at which convection is predicted to occur. The most famous value of Ra_c is perhaps $Ra_c = 4\pi^2$, obtained in the case of a horizontal aquifer under fixed temperature and impermeable pressure boundary conditions at its top and bottom. Various other values of Ra_c were

2.3 Formulation for Convection in Faulted Reservoirs

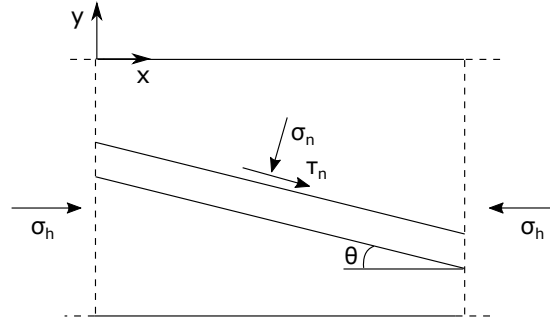


Fig. 2.3 Schematic diagram of fault, showing the definitions of stresses. In this diagram, σ_h represents a horizontal, compressive stress, σ_n the normal stress, τ_n the deviatoric (shear) stress, and θ the angle of dip.

derived analytically by [Nield \(1968\)](#) for other sets of boundary conditions and are listed in [Table 2.1](#).

P_b	P_t	T_b	T_t	Ra_c
IMP	IMP	CONST	CONST	$4\pi^2 = 39.48$
IMP	IMP	CONST	CHF	27.10
IMP	IMP	CHF	CHF	12
IMP	FRE	CHF	CHF	3
FRE	FRE	CHF	CHF	0

Table 2.1 The terms IMP and FRE for the pressure boundary conditions (BC) correspond to impermeable (Neumann BC) and constant pressure (Dirichlet BC), where CONST and CHF are constant temperature (Dirichlet BC) and constant heat flux (Neumann BC) respectively. It can be observed that different Ra_c exist from varying the BC of temperature and pressure.

2.3 Formulation for Convection in Faulted Reservoirs

In this thesis, the role of shear heating is investigated in a conceptual model, consisting of a planar fault dipping at shallow angles in a reservoir experiencing constant far-field stresses (see [Fig 2.3](#)). The assumption for the domain (reservoir) is to be rigid (infinite elastic modulus), and the fault viscoplastic. The domain boundaries are subjected to a horizontal, compressive (tectonic) stress, σ_h , which is transferred on the fault boundaries due to the rigid body assumption. This assumption strongly relies on the fact that any faults in the area will be creeping aseismically, as slip events will affect surrounding stresses which therefore invalidates the rigid body assumption.

Considering that faults are usually thin compared to the over- and under-burden structures, recent studies have shown that stresses across the fault can be considered constant inside the fault and only varying along the fault [Alevizos et al. \(2014\)](#); [Rice \(2006\)](#); [Veveakis et al. \(2010\)](#). In this case, the stress equilibrium in the momentum balance equation ([Equation 2.1](#)) yields $\sigma_{xx} = \sigma_h$ and $\sigma_{yy} = -\rho_m g |y| = -\rho g x \tan \theta$.

2.3 Formulation for Convection in Faulted Reservoirs

Therefore, the deviatoric stress τ_n varies with the dipping angle θ of the fault (see Fig. 2.3) as follows:

$$\tau_n = \sqrt{\frac{1}{2}(\sigma_{xx} - \sigma_{yy})^2} = \frac{|\sigma_h + \rho g x \tan \theta|}{\sqrt{2}} \quad (2.9)$$

Here σ_h is identified as the tectonic loading stress, and is usually of the order of several hundred MPa (typically $\sigma_h \sim 200$ MPa in active tectonic environments). Hence, the gravitational contribution $\rho g x \tan \theta$ can be considered negligible in the case of a fault dipping at shallow angles.

The fault is also assumed to be past its yield threshold and steadily creeping at critical state, i.e. without any volume changes (Alevizos et al., 2014). Therefore the last term on the right side of Equation 2.5 is set to zero ($\dot{\epsilon}_{kk} = 0$), due to the prolonged shear state of the fault. With these assumptions, the set of equations for convection in reservoirs including creeping faults can be reduced to the following:

$$\bar{\beta} \partial_t p_f = \partial_k \left[\frac{k_\pi}{\mu_f} (\partial_k p_f + \rho_f g_i \delta_{i3}) \right] + \bar{\lambda} \partial_t T - \beta_{con} \partial_k p_f + \lambda_{con} \partial_k T \quad (2.10a)$$

$$\overline{\rho C_p} (\partial_t T + \bar{v}_i \partial_i T) = \kappa \partial_{ii}^2 T + \chi \tau_n \dot{\gamma} \quad (2.10b)$$

where $\dot{\gamma}$ is the deviatoric plastic strain rate, assumed to obey a visco-plastic law of the form:

$$\dot{\gamma} = \dot{\gamma}_0 \left\langle \frac{\tau_n - \tau_Y}{\sigma_{ref}} \right\rangle \exp \left(- \frac{Q_{mech}}{RT} \right) \quad (2.11)$$

In this expression $\dot{\gamma}_0$ is a reference strain rate, τ_n the fault shear stress, τ_Y the deviatoric yield stress, assumed to obey a pressure sensitive (Drucker-Prager) relationship $\tau_Y = c + f \sigma_Y$, where c is the cohesion, f friction coefficient, and σ_Y the mean stress at yield, σ_{ref} a reference stress, and $\frac{Q_{mech}}{R}$ is the thermal sensitivity coefficient (activation enthalpy over gas constant) of the plastic flow law. The symbol $\langle . \rangle$ denotes the MacAulay brackets ensuring zero plastic strain before yield. With the above considerations, when zero dilatancy is set to respect the requirement of the fault being at critical state (i.e. no volume change) from prolonged creep, the flow law (Equation 2.11) represents a non-associative plastic law to the yield surface assumed.

In order to observe ratios of competitive processes in the system, dimensionless parameters can be defined. The normalisation of parameters become important especially in multiphysics calculations where various physical processes can be occurring simultaneously. Using a dimensionless formulation provides analytical formulae of the parameters which characterise the competition of rates of all physical processes involved. The formulation of a hydrothermal convection system by Rayleigh (1916) led to the derivation of the Rayleigh number which proved such an important concept to quantify in a single number the occurrence of convection. In the same way, the approach

2.3 Formulation for Convection in Faulted Reservoirs

used in this Thesis is also using a dimensionless formulation to explicitly define the relevant parameters that account for the multiphysics of the problem. Hence, working in a dimensionless space enables the definition of an appropriate mathematical system of equations, which can then be customised to any scenario. Specifically, when mechanics is considered, the Lewis and Gruntfest numbers become the critical parameters and are presented below in Section 2.3.1.

2.3.1 Normalisation of Parameters

In this thesis, normalised variables are defined using the following quantities:

$$\begin{aligned} p_f^* &= \frac{P_f}{\sigma_{ref}} \\ T^* &= \frac{T - T_{ref}}{\delta T_{ref}} \\ x_i^* &= \frac{x}{x_{ref}} \\ t^* &= \frac{c_{th,ref} t}{x_{ref}^2} \\ \tau^* &= \frac{\tau}{\sigma_{ref}} \end{aligned}$$

where δ a scaling factor, for example computed as $\delta = \frac{T_{bottom} - T_{top}}{T_{bottom}}$ in the case of a rectangular domain with top and bottom temperatures fixed, $c_{th,ref} = \frac{\alpha}{(\rho C_p)_m}$ the thermal diffusivity of the mixture, and T_{ref} , x_{ref} , σ_{ref} are reference quantities. Substituting these dimensionless parameters into Equations 2.10 give the final system of equations where the asterisks are dropped for convenience:

$$0 = \partial_t p_f - \Lambda \partial_t T + v_i^p \partial_i p_f - v_i^T \partial_i T - \partial_i \left[\frac{1}{Le} (\partial_i p_f + \rho_f g_i \delta_{i3}) \right] \quad (2.12a)$$

$$0 = \partial_t T + \bar{v}_i \partial_i T - \partial_{ii}^2 T - Gr e^{\frac{Ar \delta T}{1 + \delta T}} \quad (2.12b)$$

where Λ is the thermal pressurisation coefficient, defined as the ratio of thermal expansion to the compressibility of the mixture $\Lambda = \frac{\lambda_m}{\beta_m}$. The normalisation process results in various dimensionless parameters (Le , Gr), present in Equations 2.12. The values of these parameters are investigated to understand the physical processes occurring in the system.

2.3.2 Definition of Dimensionless Terms

Lewis Number

From a geological perspective, the parameter which governs the onset of convection is often thought to be permeability, since it is the least constrained parameter. Traditionally, permeability is accounted for in the definition of the Rayleigh number, a dimensionless term used to describe the evolution of classical hydrothermal convection. However in this Thesis, a different approach is taken which supersedes the concept of the Rayleigh number, and is presented in Section 2.3.4. In this approach, the effect of permeability (k_π) is accounted for through the definition of a different dimensionless group: the Lewis number.

$$Le = \frac{c_{th}}{c_{hy}} = \frac{\mu_f c_{th} \bar{\beta}^*}{k_\pi \sigma_{ref}} \quad (2.13)$$

where $\bar{\beta}^* = \bar{\beta} \sigma_{ref}$ is the normalised compressibility of the medium. Based on the definition of the Rayleigh number (Equation 2.8), note that the Lewis and Rayleigh numbers are inversely proportional to each other:

$$Le \propto \frac{\alpha \bar{\beta}^*}{Ra} \quad (2.14)$$

As such, compared to the classical formulation of the convection problem in terms of Ra , the system of Eq. (2.12) convects when the Lewis number is below a critical value Le_c .

Gruntfest Number

The Gruntfest number (Gr) describes the ratio of the mechanical dissipative work to the heat dissipated in the system, initially discovered by Gruntfest (1963). The normalised thermal dissipation of the steady creep can be expressed as

$$Gr = Gr_0 \tau_n \langle \tau_n - \tau_Y \rangle e^{-Ar} \quad (2.15)$$

$$Gr_0 = \frac{\chi \sigma_{ref} \dot{\epsilon}_{ref} x_{ref}^2}{\kappa \delta T_{ref}} \quad (2.16)$$

Gr encompasses the model of plasticity used, hence the results presented as a function of Gr are independent of the yield envelope or flow law assumed. The only dependence on the mechanical model considered is through the Arrhenius-type exponential dependence of the flow law (Equation 2.11) to temperature Paesold et al. (2016). However it has been shown in previous studies that any non-linear dependence of the flow law on temperature would have the same qualitative effects on the system's stability Veveakis et al. (2010).

Nusselt Number

The Nusselt number Nu characterises the ratio of convective to conductive heat transfer and therefore indicates whether a system is convecting or not. Various definitions of the Nusselt number have been used over time and modified according to the problem at hand (e.g. [Christensen, 2002](#); [Christensen and Aubert, 2006](#)). Traditionally, it is defined as the ratio of convective to conductive heat transfer across a boundary. This definition is most appropriate in scenarios of simple geometry having a pure diffusion temperature gradient within the boundaries of the convecting layer. However, for scenarios encompassing various layers containing non-diffusive profiles as initial conditions, the traditional definition of the Nusselt number is less meaningful in such cases. For example, the initial non-convecting state may consist of various temperature profiles corresponding to different geological units (e.g. a localised hot granite), and convection could solely occur in a specific formation. For such scenarios, no analytical solution exists for the diffusive (or non-convecting) temperature profile hence making it difficult to determine the possibility and location of convection occurring in the model, particularly if heat transfer is measured at a given point or boundary.

In order to track the effect of convection over the whole domain, a modified Nusselt number is defined in this study to be

$$Nu = 1 + \frac{\max \| k \nabla T_{conv} \|_{\Omega}}{\max \| k \nabla T_{diff} \|_{\Omega}} \quad (2.17)$$

where $\max \| k \nabla T \|_{\Omega}$ is the maximum over the entire domain Ω of the norm of the heat flux, expressed as the product of the thermal conductivity and the temperature gradient. $T_{conv} = T - T_{diff}$ denotes the convective part of the temperature when convection is modelled, while T_{diff} represents the temperature computed in a purely diffusive case. Although this formulation requires the computation of two separate simulations (with and without convection), it ensures $Nu = 1$ in the diffusive state, even when the solution of diffusion cannot be computed analytically. This volumetric definition of the Nusselt number allows the determination of the onset of convection in the domain, regardless of the geometry or initial conditions considered.

In order to analyse the onset and behaviour of hydrothermal convection, stability studies have been performed using results from both laboratory experiments and numerical methods ([Bories, 1987](#); [Combarrous and Bories, 1975](#); [Elder, 1967](#)). It was discovered that numerically solving the fluid flow equations took a prolonged time for the solution to converge, especially when the system was close to criticality ([Elder, 1967](#)). Since the focus of this thesis is on the onset of convection, this makes the numerical identification of the critical Rayleigh number Ra_c extremely difficult. Therefore, stability analyses can be used to effectively track the evolution of convection from its diffusive to convective state.

2.3 Formulation for Convection in Faulted Reservoirs

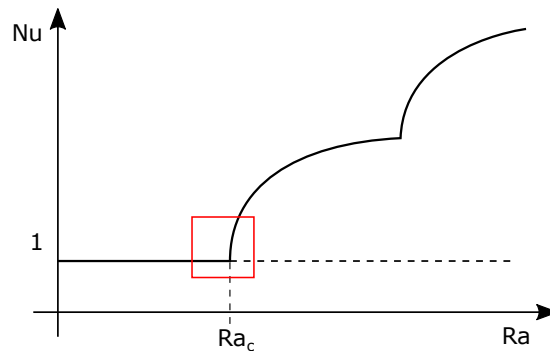


Fig. 2.4 Conceptual evolution of the Nusselt number with respect to the Rayleigh number in the case documented by [Bories \(1987\)](#), where the solid line indicates the steady state solution of convection, and the dotted line is the unstable branch. Convection occurs above the critical Rayleigh number Ra_c indicated by $Nu > 1$, and increases in strength for values of $Ra > Ra_c$. Another mode of convection is visible for larger values of Ra . The box highlights the focus of this study on the onset of convection.

2.3.3 Linear Stability Analysis

When a physical problem is mathematically described by a set of differential equations, its stability is usually analysed through a linear stability analysis (LSA) to identify the parameter space leading to the various regimes of the system and their respective stabilities. Linearising the problem by taking the first order of a Taylor expansion series of the solution is the simplest way to provide a mathematical solution. Linear stability analyses have therefore been proven extremely useful in systems which are simple enough to remain mathematically tractable ([Elder, 1967](#); [Rayleigh, 1916](#)). The main advantage of using a LSA for hydrothermal convection in porous media is to accurately determine the definition and critical value of the Rayleigh number, Ra_c , required for the system to convect. Another advantage is the ability to not only track the steady state behaviour of convection at lower [near-critical] Rayleigh numbers, but also the behaviour of the system for higher values of $Ra > Ra_c$.

The stability of a convective system in a non-deformable porous medium is generally studied with respect to the Rayleigh number. Conventionally, such stability analyses were described by plotting the steady state solution of the problem in a 2D diagram representing the Nusselt number (Nu) evolution against the Rayleigh number (Ra). Studies have shown that convective systems can evolve into different modes with increasing Ra numbers (e.g. [Combarous and Bories, 1975](#); [Florio, 2013](#); [Florio et al., 2015, 2017a,b](#)), marked by characteristic segments on the stability curve (see Figure 2.4).

Linear stability analyses have been successfully performed using analytical approaches ([Elder, 1967](#); [Rayleigh, 1916](#)) but were restricted to homogeneous cases. When confronted with complex geometries, distributions of material properties and coupled physical processes, numerical simulators are often the more convenient choice. However, running a direct sensitivity analysis using a numerical simulator is insufficient

2.3 Formulation for Convection in Faulted Reservoirs

to accurately investigate the onset of convection. Compared to a LSA, direct sensitivity analyses do not provide the same amount of information as they are unable to identify the critical parameters, nature of the solution, and the respective threshold values of the critical parameters marking changes in behaviour. Numerical simulators have limitations and results can be inconclusive for systems that are close to criticality, as observed with recent numerical simulations by [Schilling et al. \(2013\)](#) for instance. This point had been already established by [Elder \(1967\)](#), who showed it takes an increasingly prolonged amount of time for the convection to establish in a transient simulation when the system approaches criticality. As such, it is impossible to confidently determine from a numerical simulation of a non-convective system if the Lewis number is above the predicted critical value (Ra below Ra_c , conversely), or if the simulation suffered from insufficient running time. For this reason, a numerical bifurcation analysis is much more suitable and can also be extended to the case of numerical simulators.

2.3.4 Numerical Bifurcation Analysis

In this work, the stability and onset of convection in deformable media is studied using a pseudo-arclength continuation method ([Keller, 1979](#)). The focus of this thesis is purely on the onset of convection, and therefore only the response of the system close to criticality will be investigated. This study is performed with respect to the Lewis number Le (which accounts for permeability) and a modified Nusselt number Nu (see Equation 2.17). The advantage of a numerical bifurcation analysis is the achievable tracking of the evolution of convection in any domain despite varying material properties and non-homogeneous geometries. The numerical implementation of the mathematical model, equations used, and the pseudo-arclength continuation method are detailed in the following chapter.

Chapter 3

Numerical implementation

The abundance of numerical codes created to investigate fluid and mass transfer in groundwater aquifers and geothermal settings have given users a large variety of choices. These state-of-the-art codes are industry-standard and have the capability to solve multi-phase flow with reactive transport in the context of a porous medium. Some codes include FEFLOW, which is still being developed since 1979 (Diersch, 2013), MODFLOW (McDonald and Harbaugh, 1988) which is also still in development (Hughes et al., 2017), HYDROTHERM (Hayba and Ingebritsen, 1994; Kipp et al., 2008), or SHEMAT (Bartels et al., 2003). More recently, some codes used for fluid flow in porous media have coupled mechanical processes, some of which include FRACTURE (Kohl et al., 1995b), FALCON (Podgorney et al., 2010, 2011; Xia et al., 2016), FEHM (Bower and Zyvoloski, 1997; Zyvoloski et al., 1988, 1997), TOUGH2 (Pruess et al., 1999) or OPENGEOSYS (Kolditz et al., 2012). Table 1.1 lists some of the codes mentioned along with their capabilities in solving multiphysics.

At engineering timescales, the assumption of undeformable porous media can be appropriate, however this can be a drastic simplification when geological timescales are considered, as basins can deform quite considerably over time. Some numerical simulators are able to account for deformation and are aiming at handling fully coupled thermal-hydraulic-mechanical-chemical (THMC) processes. The numerical simulators FEHM and OPENGEOSYS, for instance, have incredible capabilities to simulate coupled THMC processes, but do not however accommodate a numerical bifurcation analysis. As such, this functionality had to be enveloped, which prompted to the selection of an open source platform.

One particularly suitable solution is the Multi-physics Object Oriented Simulation Environment (Gaston et al., 2009). This open source finite element, parallel platform was specifically developed to solve tightly-coupled systems of equations and provides great flexibility in terms of programming modularity and functionalities, such as the ability to run on unstructured meshes. By default, MOOSE also comes with a series of physics modules which can be easily extend to model more complex behaviours. When such irregular geometrical configurations are considered, the use of a finite element

3.1 REDBACK

method (FEM) over the finite difference method (FDM) is preferred as it generally results in minimized errors since FDM is an approximation of a Taylor series expansion, whilst FEM performs integration in each element. Another advantage of MOOSE is that it is specialised for tightly-coupled problems where all variables are highly dependent on each other, as opposed to sequential or loose-coupling where the relationship between variables are mostly independent.

3.1 REDBACK

One existing MOOSE module is REDBACK, targeted at **R**ock **m**Echanics with **D**issipative **f**eed**B**ACKs. This code was specifically designed as a geomechanics simulator to study coupled multi physical effects (Poulet et al., 2016; Poulet and Veveakis, 2016) and in particular, provides the ability to simulate elasto-visco-plastic deformation coupled with advective flow and chemical reactions.

3.1.1 Code Structure

MOOSE is written in C++ making it extremely flexible and powerful, incorporating various functionalities that can be applied to different applications. Its input files are written in a hierarchical, block structured syntax, which provide users with the flexibility to tackle their problem of interest, ranging from simple equations (e.g. solving a diffusion equation with simple geometries), or having multiscale, fully coupled THMC equations with realistic geometries. An example input file solving the simple diffusion equation is displayed in Figure 3.1.

Since REDBACK is built on MOOSE, it inherits the MOOSE code architecture. The flexibility of solving various problems often results in a customised input file with varying input blocks. Listed below are the brief definitions of the main input blocks used in this thesis, not necessarily used concurrently.

- **Variables:** Mathematical variables of interest which are solved across the entire mesh, at nodes (quadrature points) (e.g. temperature, pore pressure, displacement, etc.)
- **Mesh:** Mesh used for the simulation. For simple geometries (e.g. perfectly homogeneous rectangular mesh), MOOSE provides the functionality to generate such meshes. Users can also load their own meshes in a variety of file formats (e.g. .msh), which can be created from external programs (e.g. gmsh)
- **Mesh Modifiers:** Various functionalities to modify the loaded mesh file, alleviating the need to re-mesh using an external program. Some functionalities include naming/identifying particular nodes/elements, creating new boundaries/regions within the same geometry, or splitting a surface/volume.

3.1 REDBACK

- **Kernels:** Building blocks of the system of equations to be solved. Each kernel represents "a piece of physics" and describes a term in the PDE. As an example, if diffusion is desired to be solved in a particular block, a *Diffusion Kernel* will be selected.
- **Materials:** Material properties representing a particular rock type, associated with of a particular surface (2D) or volume (3D) in the mesh. In REDBACK, input values for common parameters include (but are not limited to) fluid and solid density, porosity, gravitational force, reference Lewis number, and thermal expansion coefficient(s) of the solid and fluid.
- **Executioner:** The executioner has two functionalities; steady and transient. Steady requests a steady state solution and solves the nonlinear system in just one step, whereas transient solves it in multiple steps (used to observe the evolution of the problem, or if the problem is just too hard). In the Executioner block, we are able to fine-tune various parameters such as `dt`, the timestep size between solves; the end time of the simulation, or the number of steps in the simulation. In this block, the tolerance can also be specified, as well as more advanced options like `adaptive time stepper` where timesteps can be increased when the solution is converging, or decreased when it cannot converge.
- **Boundary Conditions:** Various boundary conditions available in MOOSE, most commonly used are Dirichlet and Neumann boundary conditions, but other functions (e.g. constant flux) are also available.
- **Initial Conditions:** Initial condition applied to the start of the simulation. Can be expressed using a function, or taking value(s) from a previous result file, at a specific time step for instance.
- **Functions:** Ability to input your own function with mathematical expressions using the predefined keywords `x`, `y`, `z`, `t`, to represent space and time. Can be used in other blocks such as boundary and initial conditions, and user objects for instance.
- **Post Processors:** Explicit calculations performed based on the results obtained from the simulation; for example, calculating the maximum fluid velocity at the end of each time step.
- **User Objects:** Provide data and calculation results which can be used by other MOOSE objects (e.g. function solution UO, to apply to IC).
- **Aux Variables:** Auxiliary variables that can be be solved at both nodes or elements, in addition to the system variables. Similar to variables, explicit calculations can be performed on auxiliary variables, and will also be displayed in the result file.

3.1 REDBACK

- **Aux Kernels:** Objects describing how to update the respective auxiliary variable. The calculations performed by auxiliary kernels have the flexibility to be coupled tightly or weakly, by defining the time of their computation (e.g. at linear/non-linear iteration, beginning/end iteration, etc.).
- **Outputs:** Define all outputs required for visualisation, both for the data computed over the whole mesh (exported natively in the Exodus file format (.e), or other formats like .vtk) and for post processors (exported in .csv files).

3.1 REDBACK

```
[Mesh]
  type = GeneratedMesh
  dim = 2
  nx = 10
  ny = 10
  xmax = 2
  ymax = 2
[]

[Variables]
  [./temp]
  [../]
[]

[Kernels]
  [./diff]
    type = Diffusion
    variable = temp
  [../]
[]

[BCs]
  [./temp_top]
    type = DirichletBC
    variable = temp
    boundary = top
    value = 0
  [../]
  [./temp_bott]
    type = DirichletBC
    variable = temp
    boundary = bottom
    value = 1
  [../]
[]

[Executioner]
  type = Steady
  solve_type = PJFNK
[]

[Outputs]
  execute_on = timestep_end
  exodus = true
[]
```

Fig. 3.1 Example input file solving only the diffusion of temperature in a generated square mesh. Input blocks can be added as the problem of interest increases in complexity.

3.2 Implementation of the Pseudo-Arclength Continuation Method

For a geothermal operation to have significant economic viability in the case of Hot Sedimentary Aquifers (HSA), an ideal reservoir would potentially be large (thick) in volume, unaltered, highly permeable, and free of any geometrical flow inhibitors. In reality however, to encounter a reservoir with such ideal settings is rather uncommon as most geological basins would have been subjected to deformation over time; what would have been perfectly deposited horizontal layers could be folded, stretched, and/or pinched out. The presence of faults could also contribute to another dimension of complexity as they can act as permeability enhancers or blockers (Reid et al., 2012), potentially decreasing the economic viability of the reservoir. Therefore, it is crucial to investigate and understand the hydrothermal processes and the potential presence of convection in such realistic scenarios. Numerical simulations can easily provide an approximation of the size and location of hot upwellings when simple idealistic scenarios are considered. However, the incorporation of information provided from realistic historical and existing field data, which can be expressed by irregular boundary conditions and inhomogeneous material properties, can certainly increase complexity and make numerical simulations more time consuming. This points to the necessity of a parameter sensitivity analysis of convective systems to constrain the underlying physical processes, particularly in geothermal settings. A pseudo-arclength continuation method (Keller, 1979) is chosen as the numerical continuation method in this thesis, leveraging the power of REDBACK through a Python wrapper. The purpose of this method is to numerically track the stability of the solution with respect to a parameter. This is done by considering the parameter itself as an extra variable in the system.

3.2.1 System of Equations

The numerical stability analysis presented here combines the pseudo-arclength continuation method from Keller (1979) with the REDBACK finite element simulator. While the aim of the study is to investigate the impact of permeability through the Lewis number (Equation 2.13), the approach itself is generic and can be applied to any continuation parameter (λ) present in the system of equations. It is assumed that the solution of the steady state problem follows a continuous curve with respect to λ , along the curve's length S (see also Figure 3.2). In this thesis, λ is specifically the Lewis number.

Let u_i denote the solution vector where $0 \leq i \leq N$, with N the number of degrees of freedom of the problem at hand. In the case of this thesis, it is equal to the number of temperature and pore pressure values at every node point of the entire mesh. Let F be the discretised version over the finite element mesh of the differential operator describing Equation 2.12. In this form, the system reads $\dot{u}_i = F_i(u_i, \lambda)$ where the dot notation is used for the time derivative. Then, given a solution of the steady state problem $(u_i^{(n-1)}, \lambda^{(n-1)})$ at iteration step $n - 1$, as well as the direction $(du_i^{(n-1)}/dS, d\lambda^{(n-1)}/dS)$

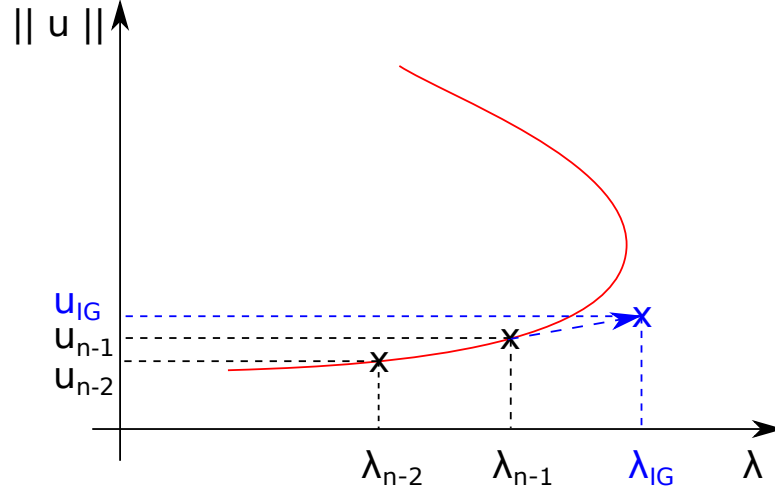


Fig. 3.2 Schematic representation of the pseudo-arclength continuation scheme, marching along the arc-length S of the curve. At every iteration step (n) of the pseudo-arclength continuation algorithm (see Fig. 3.3), the initial guess (subscript IG) is computed from the previous two solutions at steps ($n-1$) and ($n-2$).

of the solution at length $S^{(n-1)}$ we can compute the steady state solution at length $S^{(n)} = S^{(n-1)} + \Delta S$ as follows:

$$F_i(u_j^{(n)}, \lambda^{(n)}) = 0, \quad (3.1a)$$

$$(u_i^{(n)} - u_i^{(n-1)}) \frac{du_i^{(n-1)}}{dS} + (\lambda_i^{(n)} - \lambda_i^{(n-1)}) \frac{d\lambda^{(n-1)}}{dS} - \Delta S = 0, \quad (3.1b)$$

where ΔS is the marching step size along the curve. Note that λ becomes a variable in this formulation (Equation 3.1a), and its value is solved to track the stability curve of the whole system. This is the main difference with a traditional sensitivity analysis for which values of λ are selected as inputs and used to solve for the other variables (i.e. temperatures and pore pressures).

3.2.2 MOOSE Scalar Kernel

At each iteration step n , the system of equations (3.1) has $N+1$ unknowns: $(u_i)_{0 \leq i \leq N}$ and λ . The matrix of temperatures and pressures (u_j) may often be large as it dependent on mesh size; a mesh containing 1 million nodes will result in a matrix of size 2 million. In contrast, λ is a single unknown value being added to the system. The system (3.1) is solved within REDBACK by using a MOOSE `ScalarKernel` to solve Equation (3.1b), on top the normal implementation which solves Equation (3.1a). The `ScalarKernel` defines the residual for the `ScalarVariable` defined as Equation 3.1b. The `ScalarKernel` is expressed with respect to the variable λ . As such, the first term of Equation 3.1b, which only includes the other variables, appears as a single term which can be referred as a directional derivative.

3.2 Implementation of the Pseudo-Arclength Continuation Method

$$\left(T_1 \quad \dots \quad T_n, \quad p_{f_1} \quad \dots \quad p_{f_n} \right) \begin{pmatrix} \frac{dT_1}{dS} \\ \dots \\ \frac{dT_n}{dS} \\ \frac{dp_{f_1}}{dS} \\ \dots \\ \frac{dp_{f_n}}{dS} \end{pmatrix}$$

which can also be written as:

$$\underbrace{\sum_{nbmesh} (T_1 - T_1^{n-1}) \frac{dT}{dS} + (p_{f_1} - p_{f_1}^{n-1}) \frac{dp}{dS}}_{\text{directional derivative}}$$

3.2.3 Initial Guess and Iterative Calculations

At each iteration of the pseudo-arclength continuation method, an initial guess ϕ_0 is first calculated in the prolongation of the previous two solution points (at iterations $n - 1$ and $n - 2$), see Figure 3.2.

$$\phi_0 = 2T_{n-1} - T_{n-2} \quad (3.2)$$

$$\overrightarrow{M^{n-2}M^{n-1}} = \overrightarrow{M^{n-1}M^n} \quad (3.3)$$

$$\overrightarrow{M^h} = \overrightarrow{M^{n-1}} + \overrightarrow{M^{n-2}M^{n-1}} \quad (3.4)$$

$$x_{M_n} = x_{M^{n-1}} + (x_{M^{n-1}} - x_{M^{n-2}}) \quad (3.5)$$

$$x_{M_n} = 2x_{M^{n-1}} - x_{M^{n-2}} \quad (3.6)$$

where $M_n = (u_{i_n}, \lambda_n)$ are point locations on the stability curve and $\overrightarrow{M^iM^j}$ the vector between two points at iteration steps i and j .

An external iterative algorithm, shown in Figure 3.3, is implemented in Python to generate all corresponding input files for REDBACK at each step, run the simulations, and extract all information needed for the following step. This algorithm is initialised by running three simulations. Firstly, a reference simulation is performed with diffusion only (where the advective terms of Eq. (2.12) are neglected) to obtain the reference temperature T_{diff} needed to compute the Nusselt number as shown in Eq. (2.17). Next, we perform two REDBACK simulations for two initial values of λ (Le) to compute the initial direction of the solutions along the curve, using the secant method, which starts the iterative continuation algorithm. The algorithm starts from a convective system and moves towards a diffusive one, tracing the stable branch of the system. Currently, the pseudo arclength method has the capability to trace a branch of the system but does not yet have the functionality to identify branching points (e.g. the bifurcation point shown in Figure 2.4 for which there exists the stable and unstable branch at Ra_c). As

3.3 Benchmark for numerical bifurcation algorithm: The Bratu Problem

Table 3.1 Mesh sensitivity analysis of the numerical continuation algorithm for the 1D Bratu problem (Korkine, 1869). The number N of mesh elements is varied and the value of the critical turning point C_c^N is compared with the reference solution $C_c^{ref} \simeq 3.513830719$ (Mohsen, 2014).

N	C_c^N	Error	Accuracy
10	3.542501615	0.008159442	0.991840558
20	3.520943522	0.00202423	0.99797577
30	3.516977858	0.000895643	0.999104357
50	3.514945266	0.000317189	0.999682811
70	3.514403637	0.000163047	0.999836953
100	3.514115872	8.12E-05	0.999918848
200	3.513899356	1.95E-05	0.999980467
300	3.513861876	8.87E-06	0.999991133

such, if the first step of the continuation method is of a diffusive system (lower branch), the bifurcation point may not be detected and the algorithm will continue tracing the unstable branch for lower Lewis values. Therefore in this thesis, the first step of the continuation will always be of a convective system. This will ensure the transition from the convective steady state solution (higher branch) to a diffusive solution (lower branch), thus pinpointing the critical value required for the onset of convection.

3.3 Benchmark for numerical bifurcation algorithm: The Bratu Problem

A landmark boundary value problem for benchmarking numerical stability algorithms is the Bratu problem (Korkine, 1869), which is expressed for an unknown u on a domain Ω with boundary $\delta\Omega$ as

$$\partial_{ii}u + C e^u = 0 \quad \text{on } \Omega \quad (3.7a)$$

$$u = 0 \quad \text{on } \delta\Omega \quad (3.7b)$$

where $C > 0$ is a parameter. In one dimension, this problem can be written as

$$\frac{\partial^2 u}{\partial x^2} + C e^u = 0 \quad \text{for } 0 \leq x \leq 1 \quad (3.8a)$$

$$u(0) = u(1) = 0 \quad (3.8b)$$

This one dimensional (1D) version of the problem has been studied extensively and shows a critical value $C_c \simeq 3.513830719$ for the parameter C (e.g. Mohsen, 2014) such that the problem admits two solutions if $C < C_c$, a single solution for $C = C_c$, and no solution otherwise. We solve this problem using the numerical continuation algorithm presented in Figure 3.3 and obtain the expected continuation curve shown in Figure 3.4.

3.3 Benchmark for numerical bifurcation algorithm: The Bratu Problem

```

input:  $\lambda_1, \lambda_2, \Delta S_0, S_{max}$ , REDBACK simulation file
1 Parse REDBACK input file and store simulation object sim to generate other input files
2 Generate REDBACK input file for diffusion-only
3 Run steady-state diffusion-only simulation to get  $T_{diff}$  (see Eq. (19))
4  $S = 0$  (pseudo arclength initialisation)
5  $\lambda = \lambda_1$  (first initial guess)
6 Generate corresponding REDBACK input file
7 Run steady-state simulation to solve for  $p_f, T_{conv}$  over the whole mesh
8 Extract Nusselt number from output postprocessor
9  $\lambda = \lambda_2$  (second initial guess)
10 Generate corresponding REDBACK input file using previous values of  $p_f, T_{conv}$  as initial conditions
11 Run steady-state simulation to solve for  $p_f, T_{conv}$  over the whole mesh
12 Extract Nusselt number from output postprocessor
13 Update  $S$  by computing pseudo arclength between first two initial solutions
14 while  $S \leq S_{max}$  do
15      $\Delta S = \Delta S_0$ 
16     step_success = False
17     while step_success == False do
18         Compute the tangent vectors  $\frac{d\lambda}{dS}, \frac{dT}{dS}, \frac{dp_f}{dS}$  using secant method from the two previous solutions (see Fig. 2)
19          $\lambda_{IG} = \lambda^{(n-1)} + \frac{d\lambda}{dS} \Delta S$  (initial guess)
20          $T_{IG} = T^{(n-1)} + \frac{dT}{dS} \Delta S$ 
21          $p_{f(IG)} = p_f^{(n-1)} + \frac{dp_f}{dS} \Delta S$ 
22         Generate REDBACK input file for iteration step simulation using  $p_{f(IG)}, T_{IG}, \lambda_{IG}$  as initial guesses for the pore pressure, temperature and continuation parameter
23         Run extended steady-state simulation, Eq. (20), to solve for  $p_f, T$  over the whole mesh, as well as scalar value  $\lambda$ 
24         if simulation converged then
25             step_success = True
26              $\Delta S = \Delta S_0$ 
27         else
28              $\Delta S = \Delta S \times \textit{cutting\_step\_parameter}$ 
29         end
30     end
31     Extract  $\lambda$  and Nusselt number from simulation output postprocessors
32      $S = S + \Delta S$ 
33 end

```

Fig. 3.3 Summary of pseudo-arclength continuation algorithm (Keller, 1979) for a continuation parameter λ . A Python wrapper is used to generate and run REDBACK simulations for all steady-state calculations.

3.3 Benchmark for numerical bifurcation algorithm: The Bratu Problem

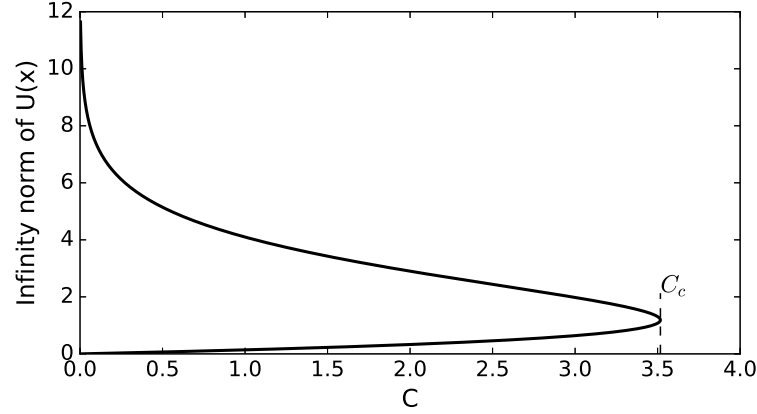


Fig. 3.4 Bifurcation analysis on 1D Bratu problem, highlighting the critical turning point C_c .

The accuracy of the numerical value obtained for the critical turning point value depends on the mesh refinement and table 3.1 shows the results of a mesh sensitivity analysis. These results validate the implementation of the continuation algorithm.

3.3.1 Scaling Factor

The numerical continuation presented above solves for $N + 1$ variables, with N (the number of degrees of freedom of the initial problem) being linearly proportional to the number of mesh nodes. In order to avoid a disproportional weight applied to the mesh variables, a balance should be considered between the numerical tolerances used for each of the variables and the scalar variable. As such, a scaling factor α is introduced to multiply the residual of the scalar kernel, so that the global residual can be expressed as:

$$\sum_{k=1}^{n_{var}} \sum_{i=1}^{n_{nodes}} \mathbb{R}_i^k + \alpha \mathbb{R}_\lambda < tol \quad (3.9)$$

where n_{var} is the number of variables (in this case $n_{var} = 2$ for T, p_f), n_{nodes} the number of mesh nodes, \mathbb{R}_i^k the residual at node i for variable k , and \mathbb{R}_{lambda} the residual of the scalar variable λ . The above equation highlights that α should scale with the mesh size ($\propto N$), in order to respect the balance of residuals and preserve enough accuracy in the calculation of the scalar variable λ .

In the context of this thesis, two variables are used (T, p_f), and a large error on the computation of the λ (Le) term has been occasionally obtained for larger meshes, as illustrated in Figure 3.5, which led to the introduction of this scaling factor. In this instance, the identification of the curve as a nonsensical result is obvious as the solution to this stability curve has been extensively studied and documented (Combarrous and Bories, 1975). However for more complex systems with multiple variables, the stability curve may not necessarily have been previously investigated, which points to

Example Result of High Residual Error for λ -term

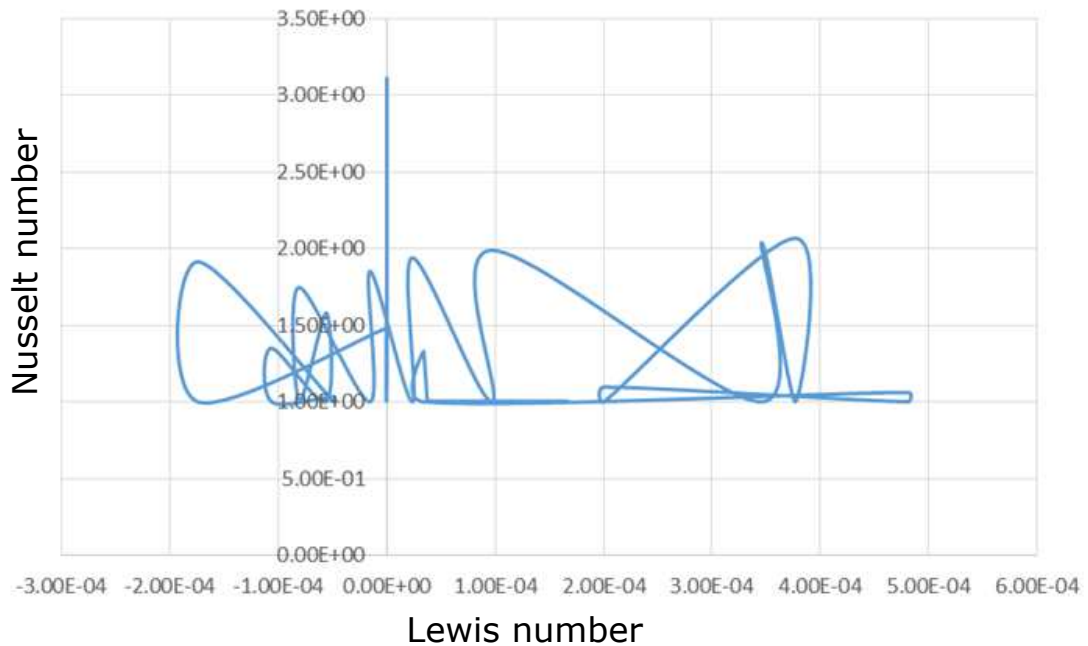


Fig. 3.5 Stability plot displaying a result of high residual error of the λ -term, resulting in a nonsensical result and negative Lewis numbers. This result can be easily identified as unrealistic since theoretical solutions have been previously obtained (see Figure 17 in (Combarous and Bories, 1975), for instance).

the inherent challenge to validate such curves. To circumvent this issue, a sensitivity analysis (detailed in Section 3.4) must always be performed to ensure the reproducibility of results regardless of the number of elements in the mesh.

3.4 Mesh Sensitivity Analysis

Numerical results can be highly dependent on mesh geometry and the number of elements in the mesh; users are forced to balance accuracy from finer meshes and computational costs. To verify simulation results, mesh sensitivity analyses are always performed. This section presents some mesh sensitivity analyses performed to understand the influence of mesh size when geometry is varied.

Two-dimensional (2D) examples are selected, based on the traditional example of hydrothermal convection in a rectangular domain. Note that throughout this thesis, different meshes are used in various simulations.

3.4.1 Homogeneous Mesh

In the scenario of the classical (Horton-Rogers-Lapwood) convection equations, a homogeneous mesh is used. In this case, a single material property is assigned and the sensitivity analysis is performed by running a simulation with identical parameters,

3.5 Effect of Geometry on Stability

only varying the number of elements. For this analysis, transient simulations are run until a steady state solution is reached. The steady state results are then visually examined using a visualisation package (Paraview ([Ahrens et al., 2005](#); [Ayachit, 2015](#))), comparing temperature isotherms and fluid velocities. The visual analyses confirm that the characteristics of the flow and location of convection cells for all the steady state results do not differ noticeably, instead only the resolution of temperature and flow vectors are better defined. This is expected since the geometrical dimensions of the mesh remain unchanged and only the number of elements is increased.

To quantify the numerical convergence, the Nusselt number is tracked as it describes the existence and strength of convection in the system. In this thesis, a modified version of the Nusselt number is used (see Equation 2.17), which is adapted to detect convection occurring in any localised area across the entire domain. This enables the extension to more realistic geometries where more than one inhomogeneous layer can be present.

Figure 3.6 displays the mesh and the results of the sensitivity analysis. Although it is observed that numerical convergence occurs at approximately 1500 elements, the number of elements chosen for simulations specifically using this mesh is 3000 to guarantee reliable results.

3.4.2 Mesh with Curved Layer

To introduce slightly more complex geometry, a folded (or curvy) layer is considered to observe the behaviour of the onset of convection in such cases. In the context of instabilities, sensitivity analyses are of greater significance as the results should be driven by the underlying physics and not numerical artefacts (e.g. corner effects). Thus, the geometrical impact and number of mesh elements are investigated in this section.

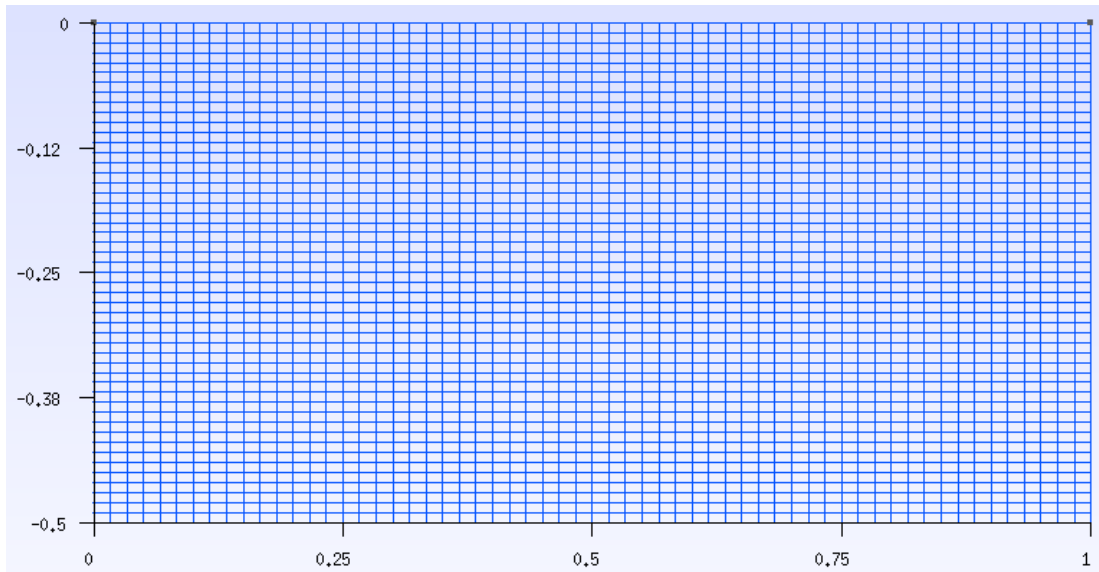
In addition to the following workflow described for the homogeneous mesh, a stability analysis is performed for this mesh and results are displayed in Figure 3.7. As expected with increasing elements, the fluctuation of results around the critical Lewis number predicted for the onset of convection is observed until convergence is reached at approximately 11,000 elements.

Interestingly however, there is no clear indication of the onset of convection, opposed to the theoretical curve derived by [Combarous and Bories \(1975\)](#) for homogeneous geometry. This signifies that the problem of varying geometry (this case being the amplitude of the middle layer) is more complex and is further investigated in the following section.

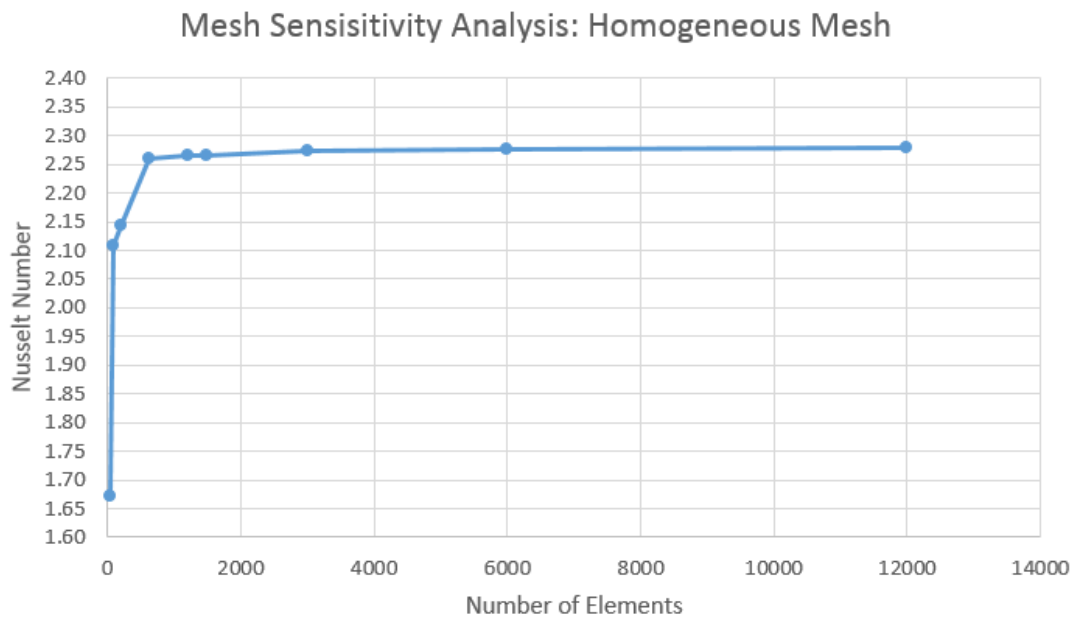
3.5 Effect of Geometry on Stability

This section investigates the impact of the amplitude of the layer curvature on the resulting continuation curve, as shown in Figure 3.7b. The results for a mesh sensitivity analysis for this mesh was shown in Section 3.4.2 and is representative of all the other

3.5 Effect of Geometry on Stability



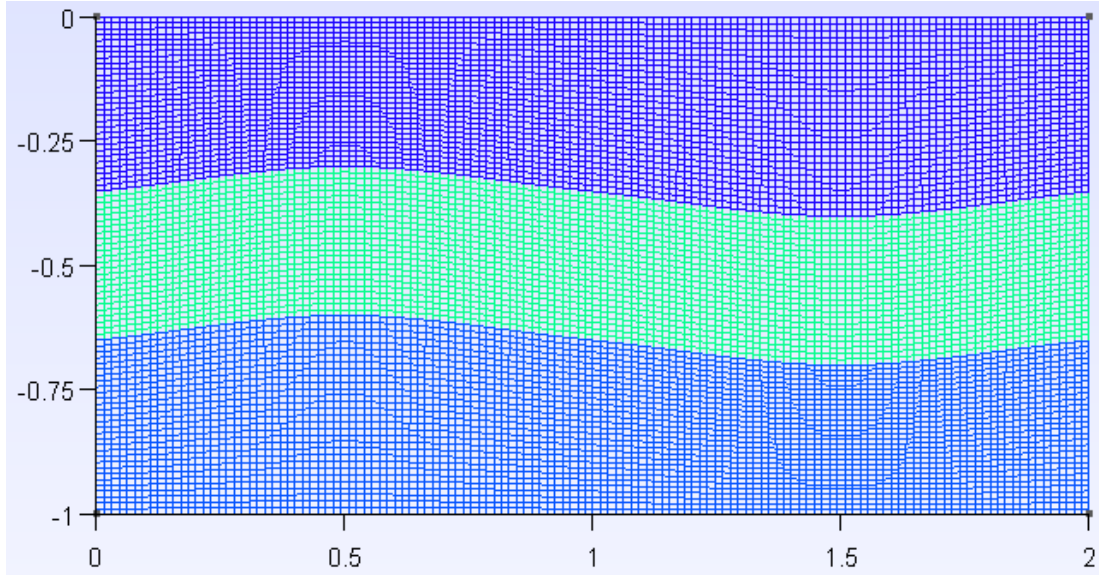
(a) Example of mesh used for the 'benchmark' simulations. The number of elements for this mesh is 1500.



(b) Graph of numerical convergence with increasing number of elements. The Nusselt number from the steady state result is plotted against the number of elements. Convergence is seen to occur approximately above 1500 elements.

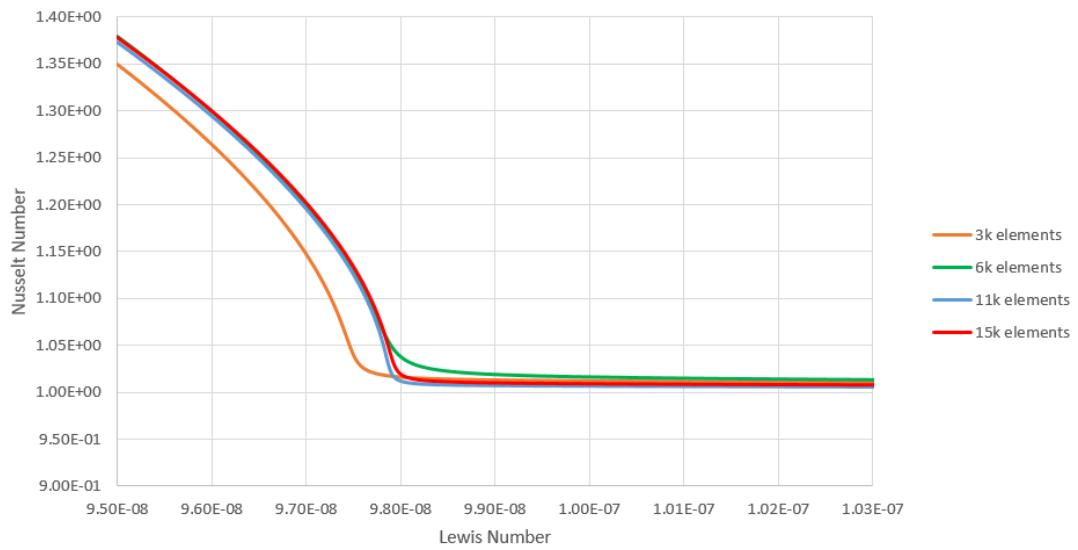
Fig. 3.6 Geometry (a) and graph showing the minimum number of elements needed for the mesh so that the solution does not vary (b).

3.5 Effect of Geometry on Stability



(a) Geometry for mesh sensitivity analysis of 0.05 amplitude.

Numerical Continuation Curves: Mesh Sensitivity Analysis for Folded Layer



(b) Continuation curves for varying elements in the corresponding mesh in (a).

Fig. 3.7 Geometry (a) and graph showing the stability curves for varying mesh elements. Numerical convergence is reached at approximately 11,000 elements (b).

3.5 Effect of Geometry on Stability

analyses performed for other meshes of varying amplitude(s). Figure 3.8 presents the geometry of increasing amplitude for this particular layer.

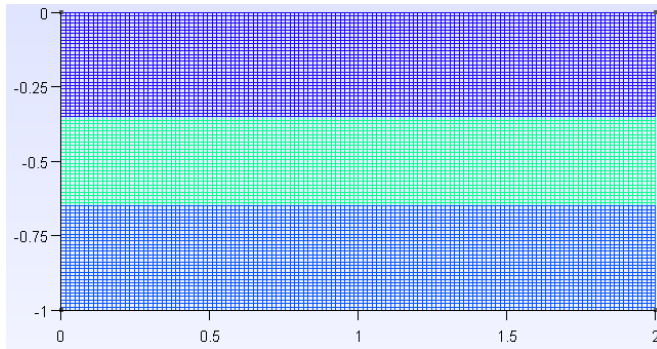
Stability curves are produced using the workflow presented in Figure 3.3 for each amplitude and results are displayed in Figure 3.9 which show an imperfect bifurcation on the onset of convection. Unlike the intersection between stable and unstable branches in the case of a perfect bifurcation (e.g. Figure 2.4), branches do not intersect in imperfect bifurcations. This signifies that no critical value can be determined for the onset of convection. In this case, the imperfect bifurcations are due to the geometrical break of symmetry. Similar findings have been previously observed in laboratory experiments (Hall and Walton, 1979; Schatz et al., 1995) where the imperfection (or perturbation) was related to the boundary conditions of a finite box.

In Figure 3.9, a perfect bifurcation is observed for the layer of zero amplitude, where Lewis values to the left of the bifurcation point ($Le_c = 9.785 \times 10^{-08}$) represents the unstable solution. Three behaviours are observed with increasing amplitudes. Firstly, it is noted that no exact point of the onset of convection can be determined for non-zero amplitudes. Secondly, the deviation away from the perfect bifurcation point (obtained with symmetrical geometry) increases significantly, and lastly, the mathematical solution for conduction is strictly $Nu > 1.00$ in these cases, compared to $Nu = 1.00$ in the case of symmetrical geometry. This then suggests a problem in determining a single clear-cut value for the onset of convection in non-symmetrical geometries.

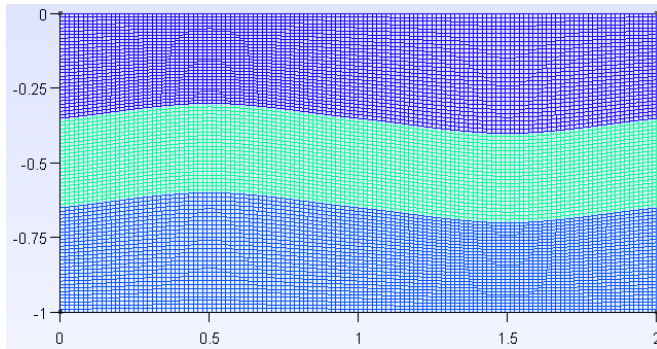
Figure 3.10 compares the behaviour of perfect and imperfect bifurcation curves. In the case of the 0.15 amplitude, the point **P1** is located at the saddle-node of the unstable branch, which corresponds to the stable steady state solution where a much high Nusselt value is obtained at $Nu = 1.13$. Depending on the other parameters of the system, convection might be already visually apparent in the system at this Nu and Le value thus making this an unlikely candidate as the value at which convection could occur. For the same **P1** Nu value, point **P3** is the corresponding steady solution at a lower Nusselt of approximately $Nu = 1.07$. Coincidentally, this point shares the same bifurcation point where $Le_c = 9.785 \times 10^{-08}$ in the case of symmetrical geometry. This points to an ambiguous zone for which the onset could occur, illustrated by the shaded grey zone in Figure 3.10, where the highest probabilities are indicated by the darker grey colours. A visual analysis of steady state results could be performed where the accuracy of Nu is preserved, but at the expense of lower permeability values (e.g. point **P4**) as the diffusive branch asymptotically tends to $Nu = 1.00$.

These interesting results demonstrate that there is no precise value for the onset of convection in scenarios containing non-symmetrical geometries. It suggests that a solution for the onset could be obtained by a visual analysis of the steady state solution, which should be performed away from the imperfect bifurcation points. This affirms the previously mentioned point of while it takes an increasingly prolonged amount of time for convection to establish in systems close to criticality, a diffusive solution of

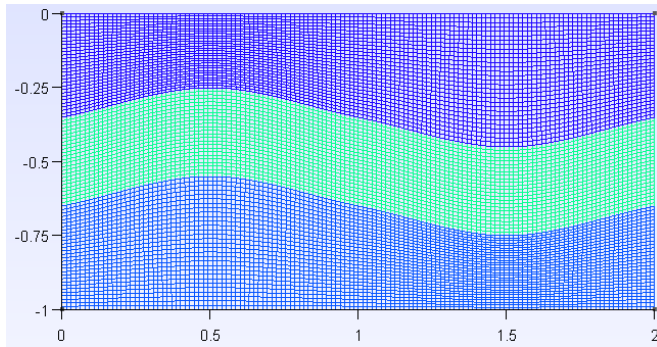
3.5 Effect of Geometry on Stability



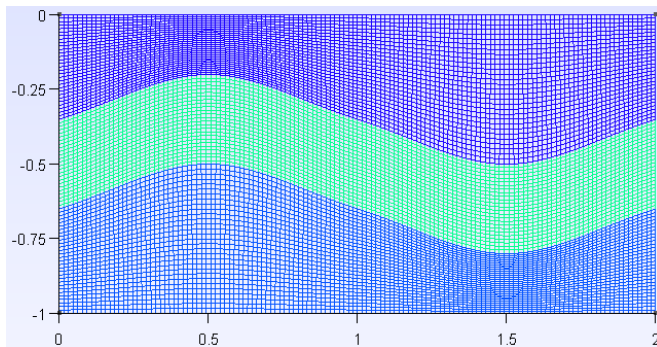
(a) 0 amplitude



(b) 0.05 amplitude



(c) 0.10 amplitude



(d) 0.15 amplitude

Fig. 3.8 Geometry of varying amplitudes, ranging from a perfectly horizontal middle layer (a) to a larger amplitude of the middle layer (d).

3.5 Effect of Geometry on Stability

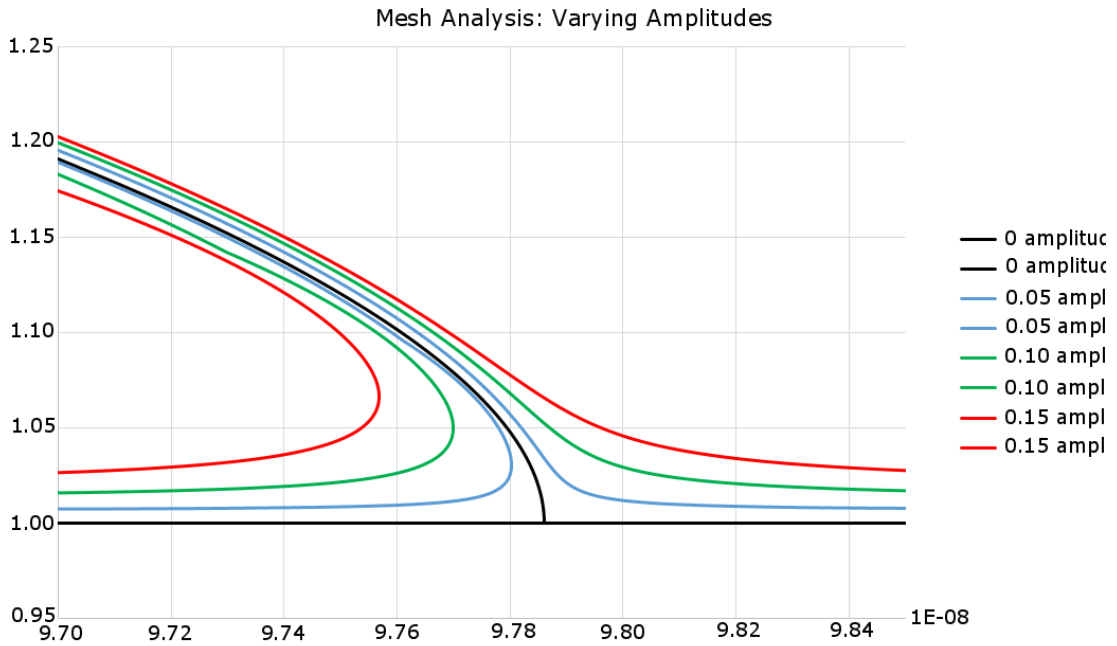


Fig. 3.9 Stability curves for varying amplitudes in the middle layer. A perfect bifurcation is observed for the layer of zero amplitude. However with increasing amplitude, stability curves diverge further away from this point.

value $Nu > 1.00$ can be obtained for cases where geometry is not perfectly horizontal. These results have substantial significance as they clearly demonstrate that the onset of convection is ambiguous with non-symmetrical geometry, and that no exact critical value can be determined at which convection is predicted to occur. Geometry and boundary conditions can be controlled in laboratory environments for instance, however are unconstrained when realistic conditions and geometries are taken into account. Therefore, the classical derivation where convection is predicted to occur past the critical Rayleigh number of $Ra_c = 4\pi^2$, for instance, cannot be applied to realistic geometries.

3.5 Effect of Geometry on Stability

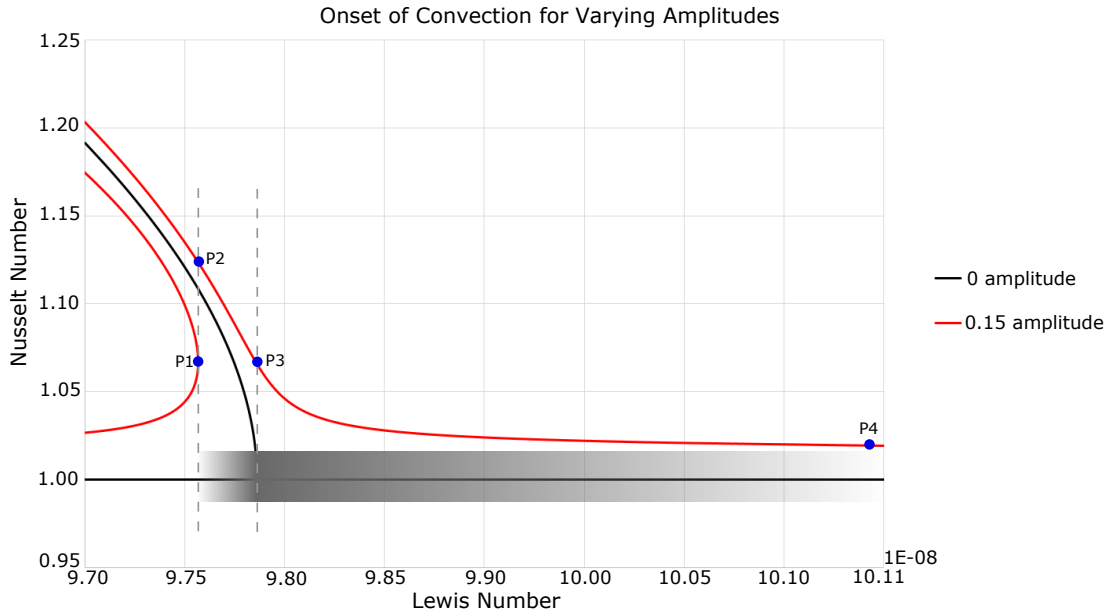


Fig. 3.10 Stability curves displaying examples of perfect and imperfect bifurcations, obtained from symmetrical and non-symmetrical geometries respectively. The grey dotted lines indicate changes in the behaviour of bifurcation curves, at which the onset could be identified. The location of point P1 is on the saddle-node of the unstable bifurcation curve, which translates to a steady state solution indicated by P2. The gradient grey region is indicative of the probability at which the onset could be identified, with the darkest grey indicating the highest probability. As such, the solution for the onset of convection is rendered to a visual analysis of steady state results, and cannot be identified as a crisp value for non-symmetrical geometries. Points P3 and P4 are indicative of such points at which a user-defined onset could be resolved, noting the change in Le_c .

Chapter 4

TH: Classical Hydrothermal Convection in Rigid Porous Media

This chapter presents an application to the workflow introduced in Chapter 2 to solve the classical Horton-Rogers-Lapwood equations (Equation 2.7) in the classical case of hydrothermal convection. In such a case, the Boussinesq approximation, Darcy's Law, incompressible solid and fluid, and rigid solid skeleton are assumed. The medium is also considered to be homogeneous. The onset of convection is customarily governed by a critical permeability (k_c), corresponding to a critical Rayleigh number (Ra_c). In the mathematical formulations for this thesis however, permeability is accounted for through the Lewis number (Le) and is approximately inverse to the Rayleigh number (see Chapter 2 for more details). Hence, the critical permeability required for the onset of convection corresponds to a critical Lewis number (Le_c), and the Lewis number will be the dimensionless group used to characterise convection from here on forth.

In this thesis, the onset of convection is investigated for various cases using the workflow described in Chapter 3, based on a pseudo-arclength continuation method. Such scenarios include the classical case of homogeneous media, varying material properties, and varying geometry. The advantage of using a numerical stability analysis is to harnesses the power of a stability analysis with the capabilities of numerical simulators. This enables the determination of critical points for the study of any system which is extremely difficult to be considered analytically, such as scenarios encompassing complex geometry and realistic material properties. While the focus of this thesis highlights the potential of using a pseudo-arclength continuation method in geothermal settings, this workflow is not limited to any geological setting. Indeed, it can be used to investigate the critical parameters responsible for the manifestation of physical phenomena in any geological system, thus opening doors to better understand the governing physical processes in many other systems.

4.1 The Horton-Rogers-Lapwood Model: Benchmark Studies

Input File Parameters for Hydrothermal Convection in Incompressible Media; Scenarios 1 and 2			
		Dimensionless Values	Real Values
Geometry	Height	0.5	500 (m)
	Length	1	1000 (m)
Boundary Conditions	Temperature top	0.0	300 (K)
	Temperature bottom	1.0	310 (K)
	Pressure top (for Scenario 2 only)	2e-02	1e+05 (Pa)
	Gravity	-1.96	9.81 (ms^{-1})
Fluid Properties	Thermal expansion coefficient	7E-04	7E-05 (K^{-1})
	Compressibility	2E-03	4E-10 (Pa^{-1})
	Viscosity	-	1.2E-04 ($Pa \cdot s$)
	Density	1.0	1000 (kgm^{-3})
	Specific heat	-	4186 ($J \cdot kg^{-1} \cdot K^{-1}$)
Solid Properties	Thermal expansion coefficient	1E-05	1E-06 (K^{-1})
	Specific heat	-	920 ($J \cdot kg^{-1} \cdot K^{-1}$)
	Compressibility	1E-03	2E-10 (Pa^{-1})
	Density	2.5	2500 (kgm^{-3})
	Porosity	0.3	0.3

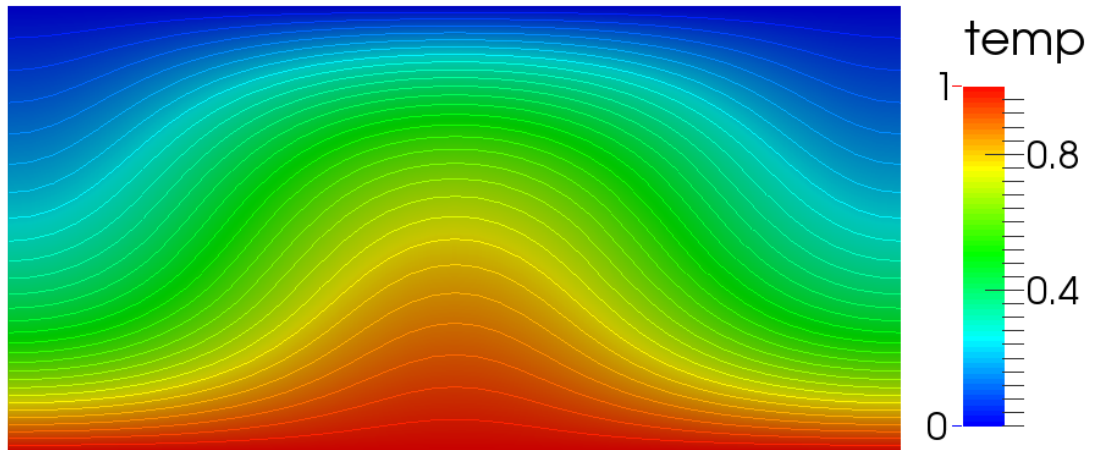
Table 4.1 Table of input parameters for Scenarios 1 and 2, solving the classical case of hydrothermal convection. Both scenarios have identical geometries, fluid and solid properties. However, the boundary conditions for Scenario 2 vary slightly; this is shown in blue. This table lists the dimensionless values used in REDBACK, which are then converted to its corresponding real values. The fluid viscosity and solid specific heat values are defined in the Lewis number and the same real values are used in the simulations.

4.1 The Horton-Rogers-Lapwood Model: Benchmark Studies

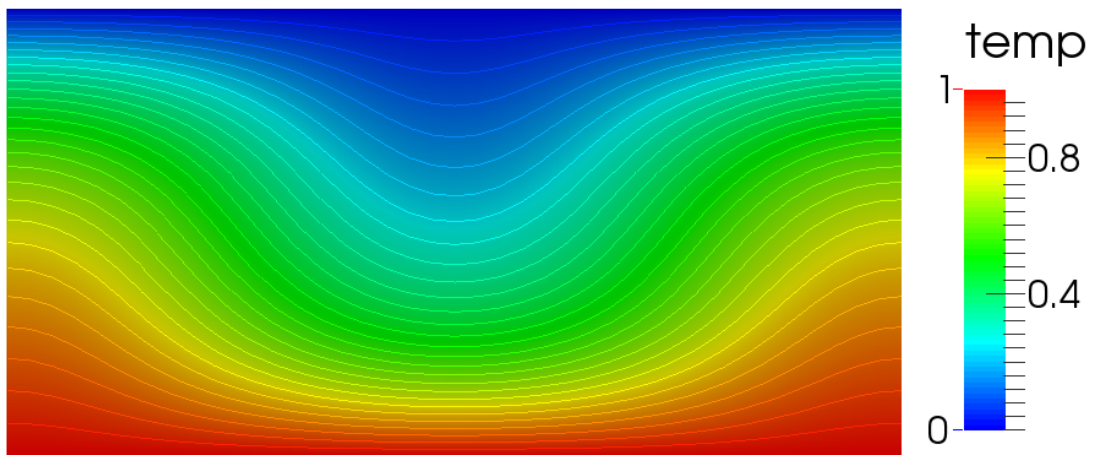
The onset of convection has been extensively studied through laboratory experiments and characterised by linear stability analyses (e.g. [Combarnous and Bories, 1975](#)). Such studies were commonly performed for a two-dimensional (2D) block subjected to specific boundary conditions and under the assumption of incompressible media. [Nield and Bejan \(2013\)](#) list various scenarios detailing the parameters required for convection to occur (e.g. Ra_c), specific to various boundary conditions. Two cases are taken as representative scenarios and listed in [Table 4.2](#) together with their corresponding critical Rayleigh numbers Ra_c , both based on the same geometry.

4.1.1 Methodology

The model considered is a 2D horizontal block with length and width of 1000m and 500m, respectively. The material properties for both Scenarios 1 and 2 are displayed in [Table 4.1](#). For Scenario 1, the boundary conditions for pressure are zero-flux (Neumann BC) on the top and bottom of the model. The temperature boundary conditions are fixed (Dirichlet BC) on both the bottom and top of the model. Scenario 2 has identical material properties and boundary conditions as Scenario 1, except for the top pressure boundary condition, for which a fixed value (Dirichlet BC) is assigned.



(a) Steady state convection result with a single upwelling in the centre of the model



(b) Steady state convection result with two upwellings at the sides of the model

Fig. 4.1 Steady state results illustrating non-uniqueness for the same value of Lewis ($Le = 3.14 \times 10^{-8}$), showing equivalent mathematical solutions. Temperature isotherms are represented by the faint white lines.

4.1.2 Non-Uniqueness of Results

In solving simple generic geometries, variations of visual results can develop despite a correct mathematical solution. This leads to the ambiguity of results and should be noted for numerical results.

For the specific case of hydrothermal convection in a square geometry with homogeneous properties (Scenario 1, see parameters in Table 4.1), the mathematical solution is not unique, as a horizontal translation of a solution by half the domain length provides another solution for instance, as shown in Figure 4.1a. Note that both cases however, are represented by the same value of the Nusselt number.

For a single material property representing a saturated porous medium in a homogeneous mesh, Figure 4.1a shows the steady state solution of the peak of the convection cell in the centre of the mesh, while 4.1b is on the sides. Although both steady state results share the same value of Nu , this leads to the fact that geometry can play a

4.1 The Horton-Rogers-Lapwood Model: Benchmark Studies

role; the more generic the geometry, the more possible symmetries in the solution, and therefore the more ambiguity involved in predicting the solution.

Studies by Florio et al. (2017b) illustrate this type of non-uniqueness of the solution and show that four different modes of convection can be obtained in a 2D rectangular geometry for the same critical parameter (Rayleigh number). They investigate the influence of the dimensions of the box (i.e. 3D volume made up of 2D planes) and conclude that the preferred mode for the onset of convection is sensitive to the geometry of the box. Detailed perturbation studies have also been performed and discussed in Florio (2013); Florio et al. (2015) and Florio et al. (2017a). While it is acknowledged that the physical manifestation of convection cells are dependent on box geometry, the focus of this Thesis is solely on determining the occurrence of convection for a given geometry, specified for each scenario investigated.

The pseudo-arclength continuation method is documented to be particularly useful in determining the onset and studying the evolution of convection, as shown in Combarnous and Bories (1975), for example. Thus, the following section presents the results for the onset of convection investigated using the implementation of this method in a numerical simulator, REDBACK.

4.1.3 Results

The steady-state temperature profile for Scenarios 1 and 2 are displayed in Figures 4.2a and 4.2b. For these results, the selected Lewis numbers are $Le_1 = 3 \times 10^{-8}$ and $Le_2 = 4 \times 10^{-8}$, with corresponding permeability values of $k_1 = 9.0 \times 10^{-13}$ and $k_2 = 6.8 \times 10^{-13}$ for Scenarios 1 and 2, respectively. The corresponding stability analysis for each case is run using the numerical continuation method presented in Chapter 3 and results are displayed in Figure 4.2c and 4.2d. Since the Lewis and Rayleigh numbers have an inverse relationship, increasing Rayleigh numbers/permeabilities correspond to decreasing Lewis numbers, and the stability curves will be symmetrical around the y-axis compared to the usual plots presented in traditional linear stability analyses. A Nusselt number of $Nu = 1$ on the stability curve defines a steady state solution of pure conduction and $Nu > 1$ indicates convection occurring in the system. The evolution of Nu with respect to Le obtained (see Figure 4.2) matches the expected theoretical behaviour (Combarnous and Bories, 1975), and the critical Lewis value (Le_c) calculated for the onset of convection is clearly determined in both cases.

For Scenario 1, the critical Lewis number required for convection is $Le_c = 3.66 \times 10^{-8}$. This translates to a critical Rayleigh number of $Ra_c = 35.59$, differing from the documented value of $Ra_c = 4\pi^2 = 39.48$ (Nield and Bejan, 2013). Similarly in the second scenario, the critical Lewis number obtained translates to a lower critical Rayleigh number $Ra_c = 26.31$ compared to the documented value of $Ra_c = 27.10$.

4.1 The Horton-Rogers-Lapwood Model: Benchmark Studies

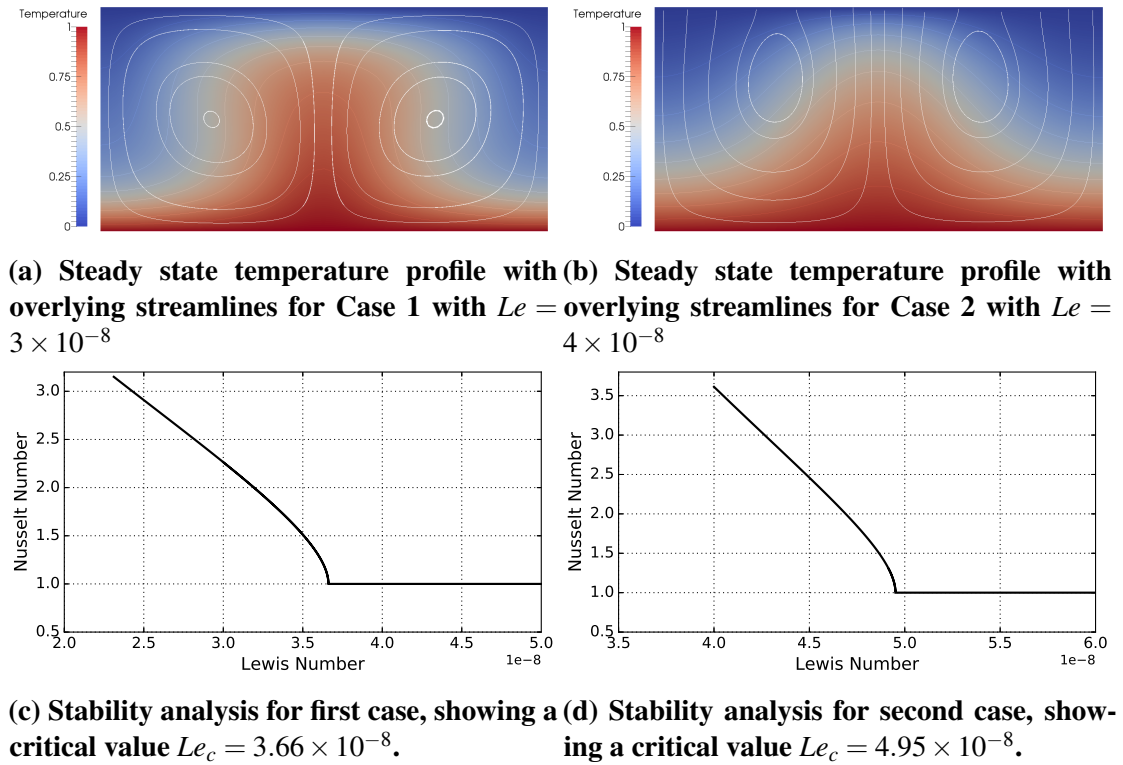


Fig. 4.2 Benchmark results showing the expected values for Le_c in both scenarios, as listed in Table 4.2. Note the mirrored plots of Nu against Le compared to Fig 2.4.

Case studies							
Scenario	P_l	P_u	T_l	T_u	Incompress. Ra_c	Le_c	compressible Ra_c
1	IMP	IMP	CON	CON	$39.48 = 4\pi^2$	3.66×10^{-8}	35.59
2	IMP	FRE	CON	CON	27.10	4.95×10^{-8}	26.31

Table 4.2 Benchmark table, adapted from [Nield and Bejan \(2013\)](#), showing the boundary conditions for temperature T and pore pressure P at the upper (subscript u) and lower (subscript l) boundaries, along with the corresponding critical values of Ra_c for the incompressible case. IMP = impermeable; FRE = free; CON = conducting. The terms free and conducting are equivalent to constant pressure and constant temperature (e.g. Dirichlet boundary conditions), respectively. The critical Lewis values Le_c for the compressible case can be translated back to Rayleigh numbers, listed in the column 'compressible Ra_c '.

4.2 Effect of Fluid Compressibility

This discrepancy is expected as the system of equations solved (Equations 2.12) accounts for fluid compressibility, whereas the documented values from [Nield and Bejan \(2013\)](#) are taken for the incompressible case.

4.2 Effect of Fluid Compressibility

To investigate the role of fluid compressibility, varying compressibility values for Scenario 2 are used in the numerical continuation method described in Chapter 3. The relationship between the critical value of the critical Lewis number Le_c and fluid compressibility is shown in Figure 4.3, which illustrates the impact of fluid compressibility.

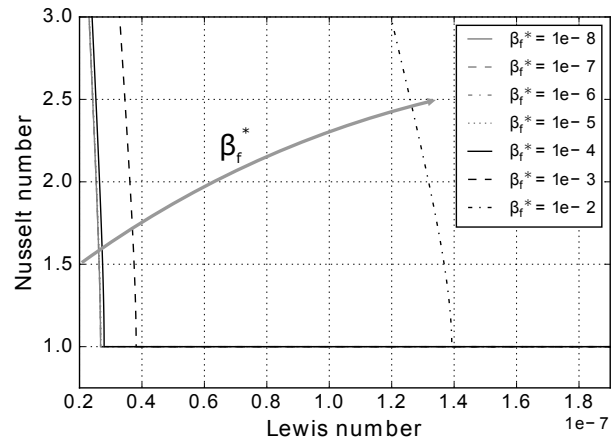
In Figure 4.3a, corresponding stability curves are plotted for increasing values of normalised fluid compressibility (β_f^*). It is observed that increasing fluid compressibility results in decreasing the critical Lewis number. With respect to the onset of convection, the permeability expected for convection to occur is lowered with high values of compressibility. A linear relationship is shown in Figure 4.3b where the data points of each Le_c and corresponding β_f^* are plotted. In this graph, the data points fit a linear relationship with a R-squared coefficient of $R^2 = 0.999$. This highlights the fact that a pseudo-analytical solution of $Le_c = 1.11e - 05 \times \beta_f^* - 2.7e - 08$ (see Figure 4.3b) can be obtained using numerical methods, where the onset of convection can be determined using any normalised value of fluid compressibility for this specific scenario. Figure 4.3c displays a semi-log plot of Le_c and β_f^* , where an exponential relationship is observed. It is seen that lower fluid compressibility values ($\beta_f^* < 10^{-4}$) do not impact the critical Lewis number, however there exists a critical value ($\beta_{fc}^* \approx 10^{-4}$) at which Le_c is affected and increases exponentially.

4.2.1 Discussion

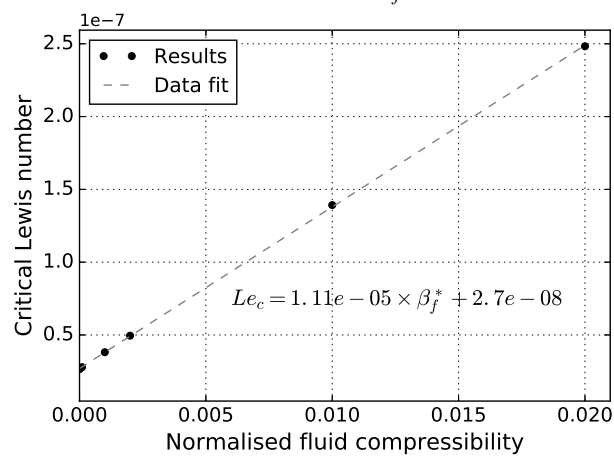
The fluid compressibility value selected in Scenarios 1 and 2 correspond to water and is $\beta_f = 4 \times 10^{-10} Pa^{-1}$, with its dimensionless form $\beta_f^* = 2 \times 10^{-3}$ (see Table 4.1). Variations of this value can be expected in realistic geothermal settings however, due to the effect of temperature, pressure, salinity, and chemical fluid composition in general. It is interesting to note that the presence of species in solution can contribute to increase the value of fluid compressibility. Thus, when simulating the occurrence of convection in geothermal reservoirs, fluid compressibility values above that of pure water could potentially cause convection to occur at lower permeabilities than previously established.

Building on the effects of fluid compressibility, slightly more complex geometry and material properties can be introduced to simulate more realistic parameters for geothermal reservoir modelling. The advancement of geophysical imaging techniques and computerised mesh generation provide more realistic geometries which better represent the problem at hand. In most modern fluid-flow software, additional material properties (not limited to key parameters found in the Lewis and Rayleigh numbers)

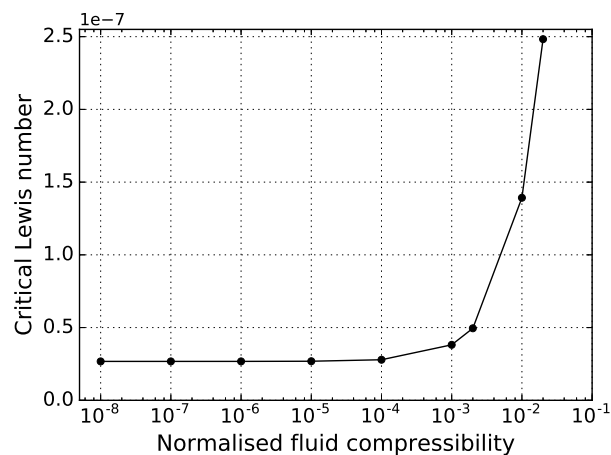
4.2 Effect of Fluid Compressibility



(a) Stability curves for various values of the normalised fluid compressibility β_f^*



(b) Critical Lewis number as a function of fluid compressibility (linear plot)



(c) Critical Lewis number as a function of fluid compressibility (semi-log plot)

Fig. 4.3 Effect of fluid compressibility on the critical Lewis number. In Figure (c), an exponential relationship is identified for critical Lewis numbers with increasing fluid compressibility values. Fluid compressibility is not recognised to influence the onset of convection until past a certain critical value, which lies within the range of $10^{-4} < \beta_f^* < 10^{-3}$.

4.3 Effect of Non-Homogeneous Geometry and Material Properties

obtained from geophysical and geological samples can also be included to observe its effects with the evolution of convection. However, whilst the improvement of geometrical data and additional material properties provide a better understanding of reality, it also modifies the critical values traditionally derived from the analytical solutions of simple geometries and material properties, as previously shown by the effects of varying fluid compressibility (Section 4.2). Finding the analytical solution(s) for scenarios containing such complex geometries and material properties can be extremely tedious and nearly impossible with an analytical approach.

The pseudo-arclength continuation method has shown to be particularly useful in determining the onset and studying the evolution of convection. The advantage to this method is that it enables the study of convection in models which are not limited by geometry and distribution of material properties. Thus, the onset of convection is investigated in a scenario containing non-homogeneous geometry and material properties.

4.3 Effect of Non-Homogeneous Geometry and Material Properties

In this scenario, a 2D model containing three layers is assumed. The middle layer is the aquifer of interest which is bounded by less permeable units above and below. Specifically, the minimum permeability required for convection to occur in this target aquifer is investigated.

To introduce geometrical heterogeneity, the middle layer is slightly folded and its bounding layers consist of marginally different material properties. In addition, random perturbations of permeability are applied over the entire model, using a log-normal distribution of standard deviation 0.5 to simulate perturbations over a constant baseline. The focus of this study is to show that this framework can handle any distribution (e.g. a beta distribution studied by Ricciardi et al. (2005)), hence the choice of a log-normal is purely illustrative. Figure 4.4a depicts the geometry and perturbed permeability range for this scenario. The boundary conditions for temperature are fixed at the top and bottom boundaries (Dirichlet BC), with a fixed pore pressure at the top, and an impermeable boundary (Neumann BC) at the bottom, similar to the conditions of Scenario 2 in Table 4.1. All values for the geometry, material properties, boundary conditions, and fluid properties used in this model are listed in Table 4.3.

In this scenario, permeability of the middle layer is varied through the evolution of a baseline Lewis number, starting with identical values in all three layers (Figure 4.4a). Figure 4.4b shows the continuation curve for this system and highlights the onset of convection, obtained for a base value permeability of $2.5 \times 10^{-13} (m^2)$ for the top and bottom layers. The corresponding critical Lewis number is approximately $Le_c = 1.1 \times 10^{-7}$. This analysis shows the potential of this numerical method to extend traditional linear stability analyses to scenarios which can handle more complex

4.3 Effect of Non-Homogeneous Geometry and Material Properties

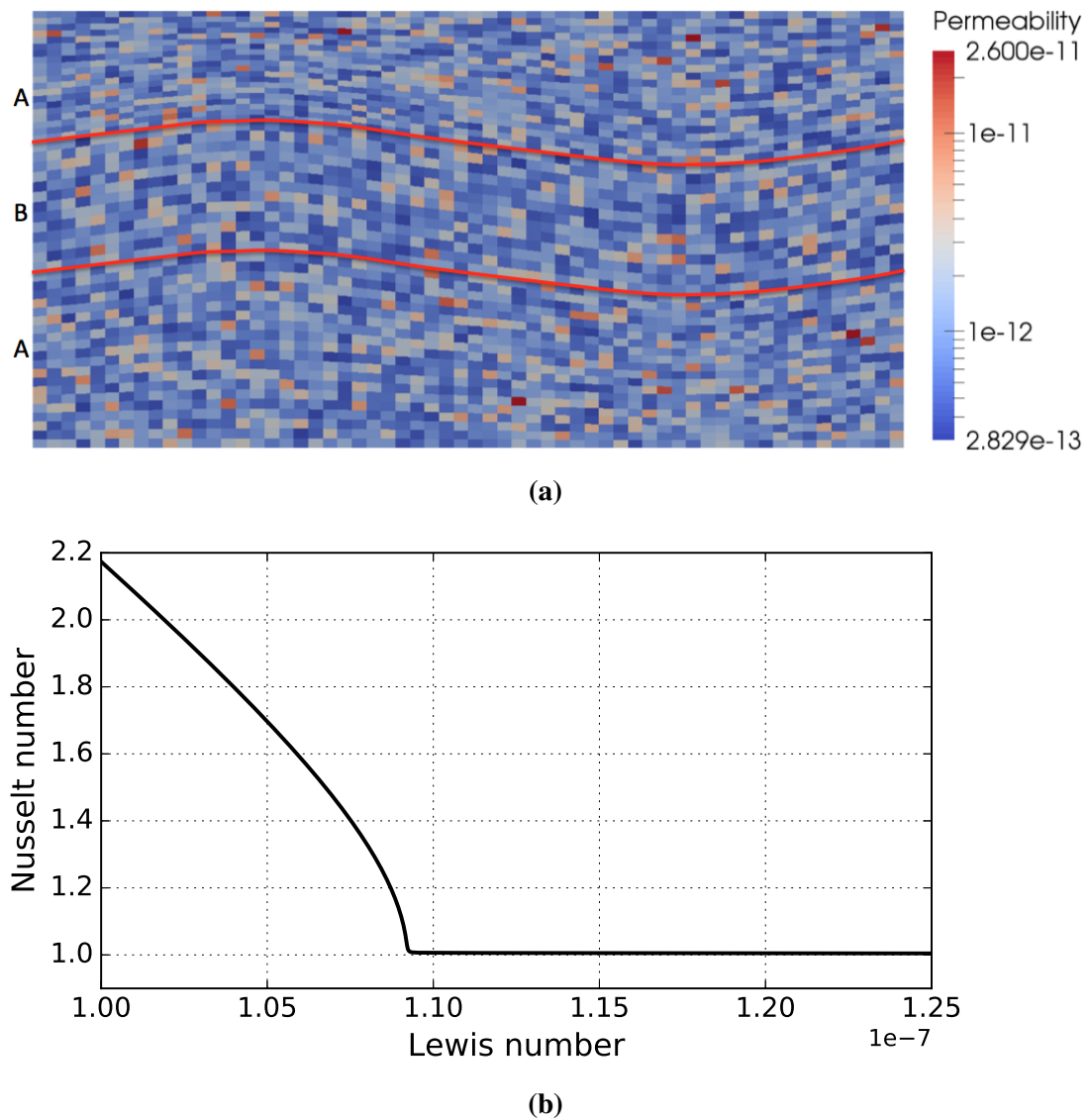


Fig. 4.4 a) Visualisation of the distribution of perturbed permeability in a model with folded geometry. A and B represent the material properties of the layer, which are listed in Table 4.3. b) Numerical stability analysis for the model, highlighting the critical Lewis number marking the onset of convection. In this particular case of a folded layer and small perturbations of permeability, the critical Lewis value is 1.09×10^{-7} .

4.3 Effect of Non-Homogeneous Geometry and Material Properties

Input File Parameters for the example of Folded Geometry and Perturbed Permeability			
		Real Values	Dimensionless Values
Geometry	Height	500 (m)	1
	Length	1250 (m)	2.5
Boundary Conditions	Temperature top	300 (K)	0.0
	Temperature bottom	310 (K)	1.0
	Pressure top	1E+05 (Pa)	2E-02
	Gravity	9.8 (ms ⁻¹)	-1.96
Fluid Properties	Thermal expansion coefficient	7E-05 (K ⁻¹)	7E-04
	Compressibility	4E-10 (Pa ⁻¹)	2E-03
	Viscosity	1.2E-04 (Pa·s)	-
	Density	1000 (kgm ⁻³)	1.0
	Specific heat	4186 (J·kg ⁻¹ ·K ⁻¹)	-
Solid Properties	Thermal expansion coefficient	1E-06 (K ⁻¹)	1E-05
	Specific heat	920 (J·kg ⁻¹ ·K ⁻¹)	-
	Compressibility	2E-10 (Pa ⁻¹)	1E-03
	Density	2500 (kgm ⁻³)	2.5
	Porosity	0.3	0.3
	Permeability A	2.72E-13 (m ²)	1.0E-07
	Perturbed permeability range	2.06E-11 - 2.83E-13 (m ²)	9.45E+08 - 3.95E+05

Table 4.3 Table of input parameters for the example of varying permeability and material properties. The solid properties are identical in all layers, except for permeability. The permeability value of Layer A is converted from Le_c .

geometries or distributions of material properties compared to the traditional analytical approaches.

4.3.1 Discussion

The behaviour of the stability curve close to Le_c reflects similar characteristics as the study performed in Chapter 3 with non-symmetrical geometry. For this particular case of a folded layer with perturbations of permeability, the response of the stability curve around Le_c does not show a clearly pronounced threshold, sharing similar characteristics to that of the folded layer scenario (Figure 3.9). Indeed, the non-symmetry of the geometry yields this result, as described in Section 3.5. It is anticipated that the distribution of perturbed permeability could compound the results of non-symmetry, therefore causing an asymptotic behaviour of the stability curve around Le_c . Since no single value of Le_c can be determined in such cases, an *effective* Le_c for the onset could be obtained through a visual analysis of the steady state solution, and could be bounded by the maximum Le value of the unstable branch (e.g. point **P2** in Figure 3.10).

This approach can be extended to investigate the extent of influence and the behaviour of varying permeability on the onset of convection in a specific geological unit, as well as the coupled effects of increased amplitudes discussed in Section 3.5. The methodology demonstrated in study has led to the discovery of the impact of non-homogeneous geometry and material properties (See Section 4.3 and Figure 4.4b) on the onset of convection. Subsequently, the flexibility of this method can promote further research where specific questions regarding the behaviour of convection in more realistic geometries and material properties can be explored, thus contributing to

4.3 Effect of Non-Homogeneous Geometry and Material Properties

understanding underlying physical processes in geothermal settings. Such investigations are outside the scope of this thesis but are within reach, accredited to the development of this novel numerical stability analysis method.

Chapter 5

THM: Effect of Creeping Faults on Hydrothermal Convection

Having previously investigated various scenarios of classical hydrothermal convection in the context of non-deformable porous media, these concepts are now extended to include the effects of creeping faults in porous media. Geological reservoirs are often characterised by fractures and faults, and can experience notable deformation at geological timescales. Fault mechanical behaviour in such reservoirs can range from one end member of seismic slip (e.g. stick slip) to the other with aseismic creep (e.g. continuous creep), and could exhibit both behaviours. In stick slip environments, fault movements are discrete and fast (m/yr) and can often have severe repercussions in human society and engineering operations. Detailed studies have been performed to understand such mechanisms (e.g. [Dieterich, 1978b](#); [Scholz, 1998](#)) in order to anticipate destructive earthquakes and prevent production well loss, for example. In contrast, faults which exhibit steadily creeping behaviour are characterised by slow and continuous movements (mm/yr), and are often thought to have less drastic repercussions in engineering operations. These faults experience shear heating, defined as the frictional heat generated from its resistance to shear. Shear heating effects of creeping faults have been shown to play a critical role in various geological settings as they were identified as triggers for earthquakes (e.g. [Dieterich, 1978a](#)), in the context of ice melt in glaciers ([Yuen et al., 1986](#)) or lithospheric tectonic movement ([Leloup et al., 1999](#); [Regenauer-Lieb and Yuen, 1998](#)), for example. However, the effects of shear heating in faults have not yet been fully understood in geothermal environments.

The impact of shear heating in creeping faults on hydrothermal convection is investigated by initially studying the impact on convection of a single creeping fault. This chapter presents the effects of shear heating on both the onset and pattern of convection, investigated using REDBACK and the framework presented in Chapter 3.

5.1 Model Construction

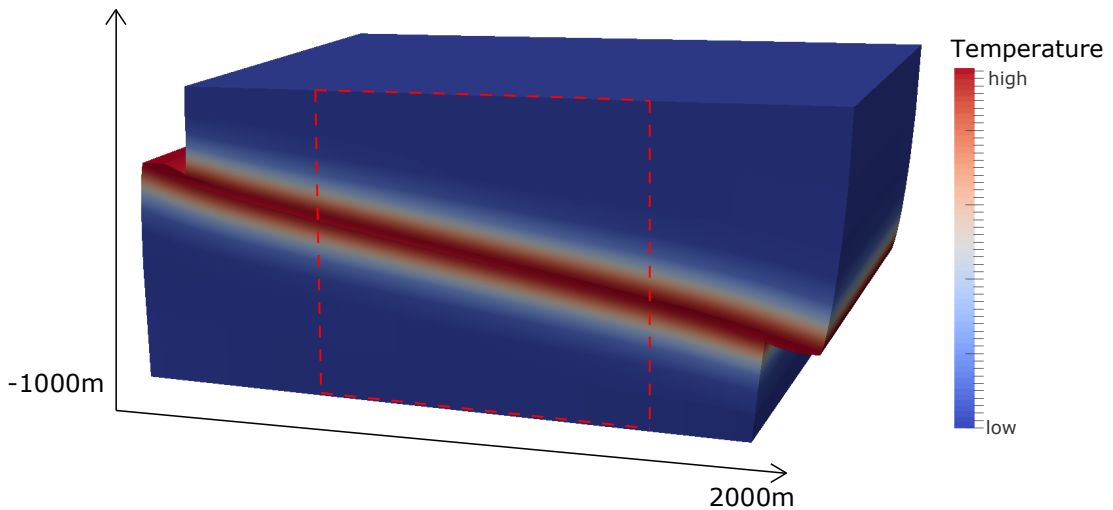


Fig. 5.1 Modelling result of 3D faulted aquifer, showing the fault displacement and shear heating effect. The fault is moving under constant velocity loading with far-field isothermal boundaries at the top and bottom of the block, and a $10\times$ exaggeration is applied to illustrate the displacement in the fault. The box outlined in red is the representation of the 2D model used to study the onset of convection (see Section 5.2).

5.1 Model Construction

Using the equations derived in Section 2.3, an end member scenario of an aquifer containing a single creeping fault is considered. One of the major assumptions used in this Thesis for underlying steady creep is that the fault displacement is negligible compared to the length of the reservoir considered. This translates to the assumption that a very large reservoir (e.g. kilometres in diameter) is considered and the total distance in which the fault has steadily moved over time is minute (i.e. a few metres). As such, the overall fault displacement is not as important as its thermal footprint, and the mechanical deformation can be accounted for through the heat dissipated from the mechanical work only. This can be illustrated in Figure 5.1, where the dissipation of temperature is more prominent than the displacement of the fault (note the $10\times$ exaggeration to observe displacement). The heat generated from the constant shear can be expressed using the Gruntfest number (encompassing the model of plasticity used, velocity, etc., see Equation 2.16), which is the parameter used to characterise the magnitude of deformation experienced by the fault. It is also assumed that the creeping rate is slow enough as to not noticeably displace the mesh in the reservoir. Therefore the effect of mechanical deformation is expressed as a heat source term in the temperature equation, and its effects on the onset and pattern of convection are investigated in a representative 2D space. The consideration of a 2D model is advantageous as similar physical processes can be solved in less computational time.

This problem can be solved in a 2D space using REDBACK, which has been developed specifically as a geomechanics simulator (described in Chapter 3) and has recently

5.2 Shear Heating Changes the Onset of Convection

Input File Parameters for Observing the Effects of Shear Heating in a Horizontal Fault			
		Real Values	Dimensionless Values
Geometry	Height	500 (m)	0.5
	Length	1000 (m)	1.0
	Fault thickness	20 (m)	2e-02
Boundary Conditions	Temperature top	300 (K)	0.0
	Temperature bottom	310 (K)	1.0
	Pressure top	1e+05 (Pa)	2e-02
	Gravity	9.81 ($m \cdot s^{-1}$)	1.96
Fluid Properties	Thermal expansion coefficient	7e-05 (K^{-1})	7e-04
	Compressibility	4e-10 (Pa^{-1})	2e-03
	Viscosity	1.2e-04 ($Pa \cdot s$)	–
	Density	1000 ($kg \cdot m^{-3}$)	1.0
	Specific heat	4186 ($J \cdot kg^{-1} \cdot K^{-1}$)	–
Solid Properties	Thermal expansion coefficient	1e-06 (K^{-1})	1e-05
	Specific heat	920 ($J \cdot kg^{-1} \cdot K^{-1}$)	–
	Compressibility	2e-10 (Pa^{-1})	1e-03
	Density	2500 ($kg \cdot m^{-3}$)	2.5
	Porosity	0.3	0.3

Table 5.1 Table of input parameters for the example of observing the effect of shear heating in a horizontal fault, listing the real values which correspond to the dimensionless values used in REDBACK. The real values for the viscosity of the fluid and specific heat values of both the fluid and solid materials are used in the simulations. The solid properties are identical in all layers, except for permeability which is varied in the study.

been used to investigate fault mechanics (Poulet et al., 2016). REDBACK is capable of solving fully coupled thermo-hydro-mechanical-chemical (THMC) processes in a 3D space. Figure 5.1 demonstrates a THM-simulation solved in 3D space which highlights the localised thermal contribution of a fault under far-field isothermal conditions. Despite REDBACK's capabilities, a 2D space is sufficient to represent the problem at hand as the focus of this study is purely to investigate the thermal effects of the fault to its surroundings. It is acknowledged that further studies could be performed with more realistic geometries and fault material properties, but lie outside the scope of this Thesis.

5.2 Shear Heating Changes the Onset of Convection

To study the impact of such a creeping fault on the onset of convection, one scenario of the cases described in Section 2.3 is first considered. In this scenario, a 2D model is considered which contains a single horizontal fault (i.e. zero dipping angle), 20m thick, present in the centre of the aquifer. The entire model is considered to be homogeneous, having a length and depth of 1000m and 500m respectively. The boundary conditions are prescribed for temperature and pressure on the top and bottom boundaries. The values for geometry, material properties, boundary conditions, and fluid properties can be found in Table 5.1.

5.2 Shear Heating Changes the Onset of Convection

The heat impact of creeping faults is represented by the numerical value of the Gruntfest number Gr uniformly across the entire fault, and in order to observe the effect of varying Gr values on the onset of convection, the numerical continuation method presented in Section 3 is applied to scenarios where Le is taken as the continuation parameter to investigate its effect on convection. Results presented in Figure 5.2a demonstrate that this continuation method is able to effectively identify the critical Lewis numbers Le_c predicted for each of the Gr values chosen.

For the reference case of $Gr = 0$, the critical Lewis number Le_c is approximately $Le_c = 4.9 \times 10^{-8}$, and represents the scenario where the fault is inactive. For increasing Gr values, it can be observed that Le_c required for the onset of convection is significantly lowered. Since permeability is approximately inverse to the Lewis number, this translates to a lower critical permeability needed for increasing values of Gr . A visual example is shown in Figure 5.3, where two steady state results are obtained for the same Lewis number ($Le = 5.5 \times 10^{-8}$). The first result obtained for $Gr = 0$ is of a non-convective solution, situated on the lower (diffusive) branch. The second result is of a slightly convective solution, for $Gr > 0$ and is located on the upper (convective) branch of the continuation curve. This indicates that convection in a reservoir containing creeping faults could be occurring for values of Le , which would otherwise only induce a purely diffusive pattern without the consideration of such creeping faults.

5.2 Shear Heating Changes the Onset of Convection

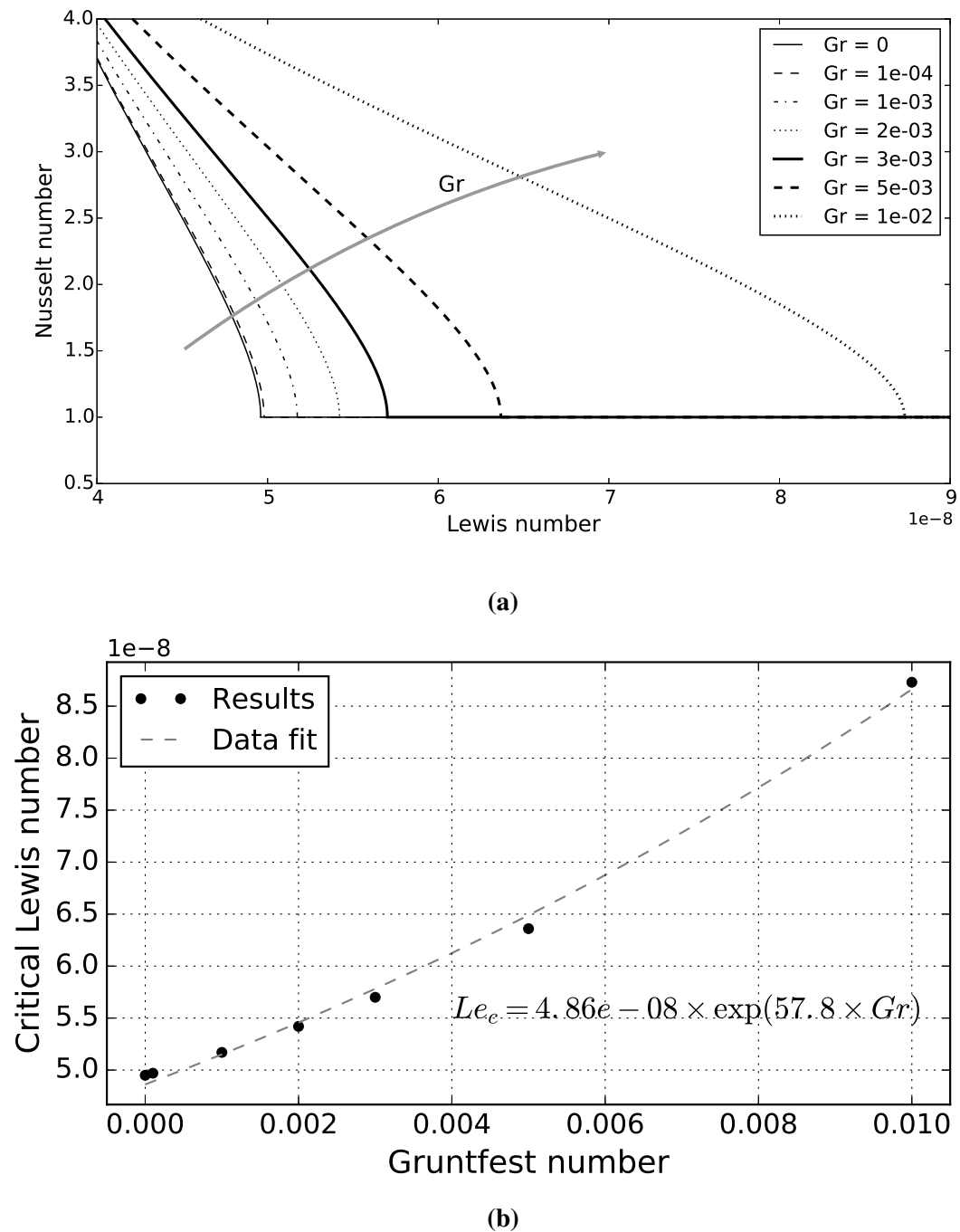


Fig. 5.2 Impact of the Gruntfest number on onset of convection. a) Continuation curves for various Gr values. The critical permeability required for the onset of convection is lowered with increasing Gr values. b) Exponential fit of Le_c with Gr , providing an analytical solution where the Le_c can be obtained for any Gr value.

5.2 Shear Heating Changes the Onset of Convection

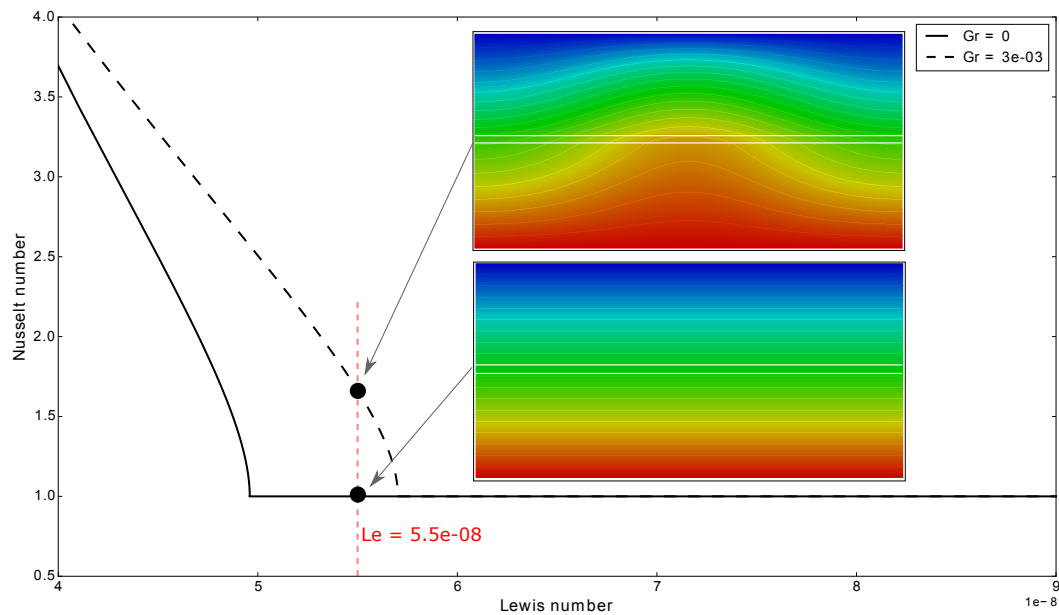


Fig. 5.3 Simulation results showing the effect of shear heating in a conceptual reservoir with model dimensions $x=1000\text{m}$, $y=500\text{m}$ containing a horizontal fault 20m thick in the centre of the model (outlined in white). At the same critical Lewis number, a purely diffusive scenario becomes convective when shear heating is present ($Gr = 3e-03$) in the fault. The fluid and material properties used in this simulation can be found in Table 5.1.

5.2 Shear Heating Changes the Onset of Convection

An exponential relationship between the critical value of Le_c with respect to Gr can be obtained from the various values of Gruntfest tested (Figure 5.2b):

$$Le_c = 4.86 \times 10^{-08} \times e^{(57.8 \times Gr)} \quad (5.1)$$

This pseudo-analytical solution provides the critical Lewis number for any value of Gruntfest, specific to the material properties and parameters (e.g. boundary condition, geometry, etc.) of this problem. This relationship can additionally be expressed as:

$$Le_c = Le_{c0} e^{\omega Gr} \quad (5.2)$$

where ω is a constant and $Le_{c0} = 4.9 \times 10^{-8}$ is the reference value at $Gr = 0$. For the values used in this example, in the case of a fault with $Gr = 0.1$ (i.e. under relatively fast tectonic loading of the order of $10^{-10} s^{-1}$), the permeability required for convection can be extrapolated and will be two times lower than without the shear heating contribution of the fault (when $Gr = 0$). This indicates that the introduction of a heat source from active faults can have a tremendous impact on the critical conditions required for the onset of convection, namely permeability. Shear heating increases the critical Lewis, which correspondingly *decreases* the permeability at which convection is predicted to occur. This renders settings that are considered stable and purely diffusive as potentially convective. Such an effect is expected to be of profound interest for geothermal applications, particularly in natural convection settings where active faults are usually present.

Numerical values of Gr for specific geological scenarios can only be derived through Equation 2.16 when all parameters are known. As an example, consider a shallow sandstone geothermal reservoir approximately 500m deep measured from the surface. For this scenario, a map of Gr values as a function of the shear stress on the fault (τ_n) and the yield stress (τ_Y) is plotted for a reference strain rate value of $\dot{\epsilon}_0 = 10^{-16} s^{-1}$ (see Figure 5.4). The values of yield stress used includes materials ranging from unconsolidated sand (kPa) to intact sandstone (MPa). The following indicative values are used: $\chi = 1$, $H = 500m$, $L = x_{ref} = 1000m$, $T_{ref} = 300K$, $\delta = 1/30$, $\kappa = 2.5W.m^{-1}.K^{-1}$, $\rho_0 = 1000kg.m^{-3}$, $Ar = 10$, $g = 9.81m.s^{-2}$ and $\sigma_{ref} = \rho_0 g H$, and all other parameters are detailed in Table 5.2. This map visually highlights increasing Gr for higher values of τ_n (larger tectonic stresses) and lower values of τ_Y (softer rocks). It also shows that Gr can actually become larger than 1×10^{-2} in active environments.

5.2 Shear Heating Changes the Onset of Convection

Indicative Parameters Gruntfest Map		
	Parameter	Values
Geometry	Height	500 (m)
	Length (σ_{ref})	1000 (m)
	Fault thickness	20 (m)
Boundary Conditions	Temperature top (T_{ref})	300 (K)
	Temperature bottom	310 (K)
	Pressure top	1e+05 (Pa)
	Gravity	9.81 ($m \cdot s^{-1}$)
	A_r (Arrhenius constant)	10
	χ (Taylor-Quinney coefficient)	1
Fluid Properties	Thermal expansion coefficient	7e-05 (K^{-1})
	Compressibility	4e-10 (Pa^{-1})
	Viscosity	1.2e-04 ($Pa \cdot s$)
	Density	1000 ($kg \cdot m^{-3}$)
	Specific heat	4186 ($J \cdot kg^{-1} \cdot K^{-1}$)
Solid Properties	Thermal expansion coefficient	1e-06 (K^{-1})
	Thermal conductivity	2.5 ($W \cdot m^{-1} K^{-1}$)
	Specific heat	920 ($J \cdot kg^{-1} \cdot K^{-1}$)
	Compressibility	2e-10 (Pa^{-1})
	Density	2500 ($kg \cdot m^{-3}$)
	Porosity	0.3

Table 5.2 Table of indicative parameters for the scenario produced in the map of Gruntfest with a reference strain rate of $\dot{\gamma}_0 = 10^{-16} s^{-1}$ (see Figure 5.4).

5.3 Shear Heating Changes the Pattern of Convection

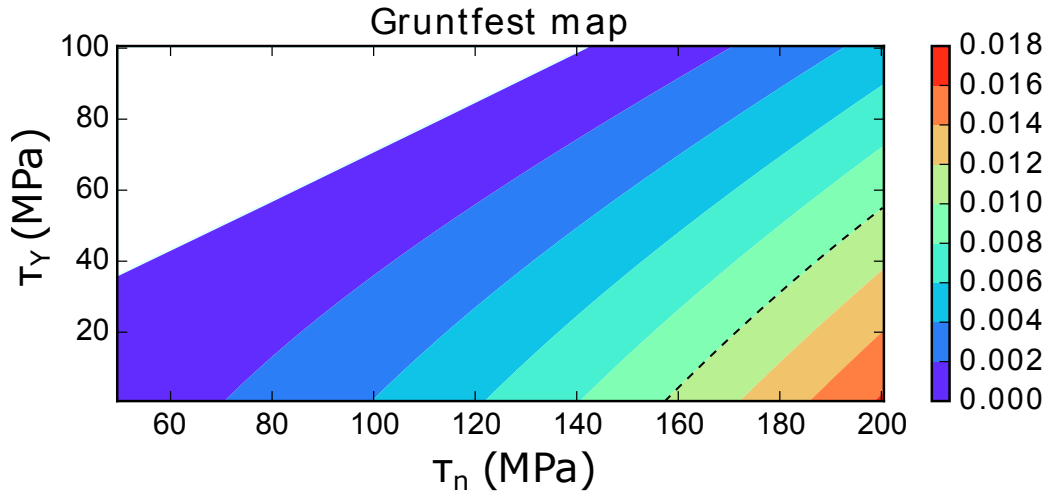


Fig. 5.4 Map of Gruntfest number as a function of the fault shear stress τ_n and yield stress for a reference strain rate of $\dot{\gamma}_0 = 10^{-16} s^{-1}$. Indicative values for this scenario are described in the text. Note that the range of yield stress values encompasses reservoir rocks as hard as consolidated sandstone (usually having a yield in shear of around 60 – 100 MPa) down to unconsolidated sand having a yield value of around 0.1 – 1 MPa. The white zone denotes the parameter space where $Gr = 0$, and the dotted line highlights the specific value $Gr = 1 \times 10^{-2}$, the maximum Gr used in Figure 5.2.

In addition to changing the critical value predicted for convection, is it postulated if shear heating can also alter convection patterns due to the break in symmetry introduced by the fault.

5.3 Shear Heating Changes the Pattern of Convection

To investigate the impact of shear heating on convection patterns, the spatial profile of temperature for the case of a horizontal fault is first discussed. This scenario presents the same problem described in the section above, and steady state results for four increasing Gr values are displayed in Figure 5.5. In this scenario, the fault has identical material properties as the reservoir, and it is noted that a calibration exercise could be performed to obtain the applicability of this workflow in specific scenarios, but lies beyond the scope of this Thesis. The aim of this investigation is to focus on the thermal effect of the fault, and this is characterised by a single Gruntfest number, for which a reference scenario of $Gr = 0$ represents the case where the fault is inactive. It can be observed that up to a certain value of $Gr = 1 \times 10^{-3}$ (which corresponds to a tectonic loading rate of $10^{-12} s^{-1}$ in this scenario), shear heating does not have any appreciable effect on the convection pattern.

For larger values of Gr ($Gr > 1 \times 10^{-3}$), Figure 5.5 shows the interaction between the heat generated from the fault and the overall convection pattern. For the case of

5.3 Shear Heating Changes the Pattern of Convection

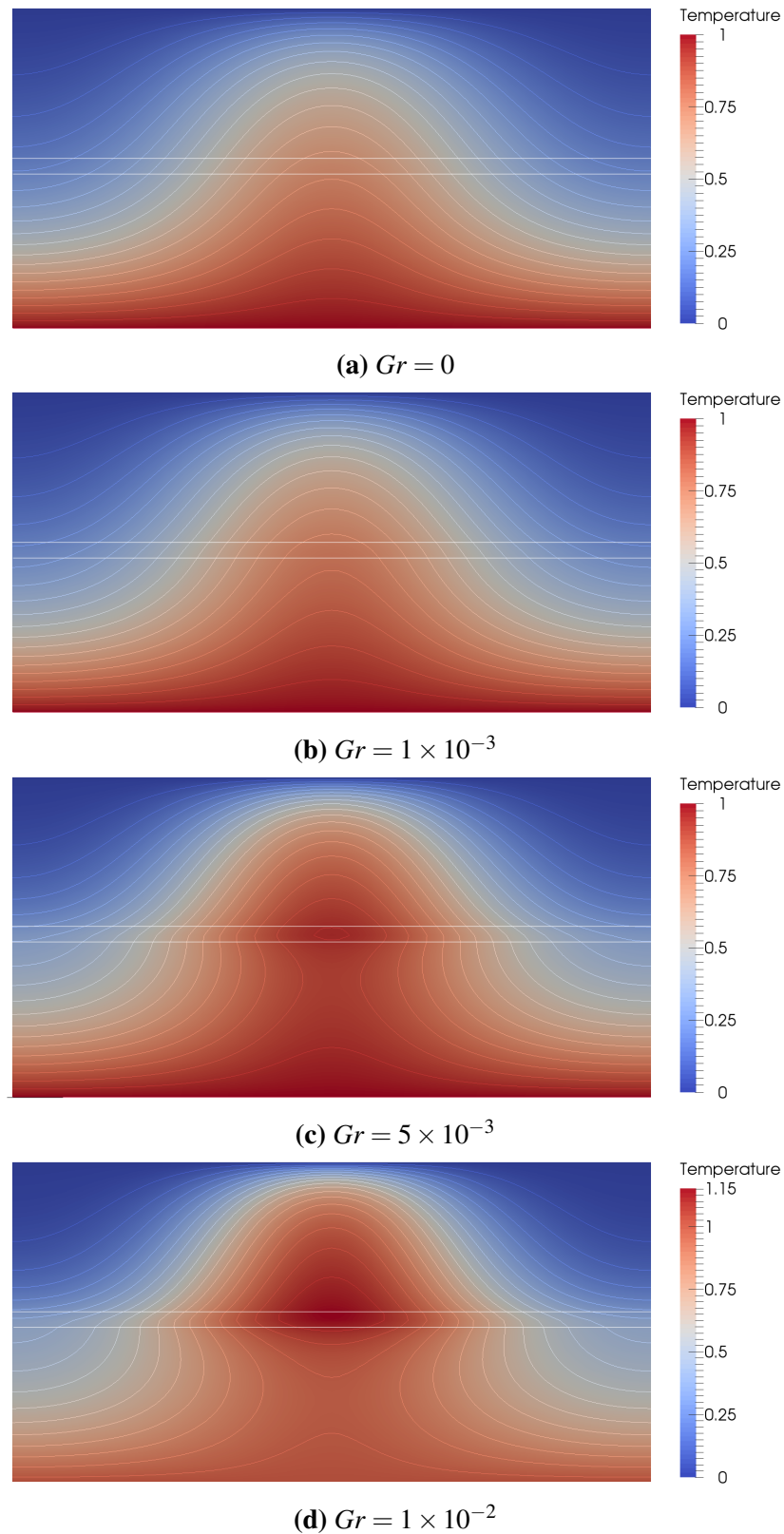


Fig. 5.5 Convection patterns for a horizontal fault in the middle of the reservoir for Gruntfest values of 0 , 1×10^{-3} , 5×10^{-3} , and 1×10^{-2} respectively. The fault is outlined in white. Shear heating is seen to change steady state convection patterns, where the heat generated exceeds the given temperature boundary conditions and localises around the fault for higher Gr values.

5.3 Shear Heating Changes the Pattern of Convection

Input File Parameters for Observing the Effects of Shear Heating in a Dipping Fault			
		Real Values	Dimensionless Values
Geometry	Height	1000 (m)	1.0
	Length	2000 (m)	2.0
	Fault thickness	10 (m)	1e-02
	Dipping Angle	10°	–
Boundary Conditions	Temperature top	300 (K)	0.0
	Temperature bottom	310 (K)	1.0
	Pressure top	1e+05 (Pa)	2e-02
	Gravity	9.81 (m·s ⁻¹)	1.96
Fluid Properties	Thermal expansion coefficient	7e-05 (K ⁻¹)	7e-04
	Compressibility	4e-10 (Pa ⁻¹)	2e-03
	Viscosity	1.2e-04 (Pa·s)	–
	Density	1000 (kg·m ⁻³)	1.0
	Specific heat	4186 (J·kg ⁻¹ ·K ⁻¹)	–
Solid Properties	Thermal expansion coefficient	1e-06 (K ⁻¹)	1e-05
	Specific heat	920 (J·kg ⁻¹ ·K ⁻¹)	–
	Compressibility	2e-10 (Pa ⁻¹)	1e-03
	Density	2500 (kg·m ⁻³)	2.5
	Porosity	0.3	0.3

Table 5.3 Table of input parameters for the example of observing the effect of shear heating in a reservoir containing a dipping fault, listing the real values which correspond to the dimensionless values used in REDBACK.

$Gr = 1 \times 10^{-2}$, the heat is localised inside the fault, causing the upwelling plume to be slightly wider than the cases where $Gr < 1 \times 10^{-3}$. Shear heating significantly alters the convection patterns especially for $Gr = 1 \times 10^{-2}$, where the maximum temperature exceeds the given temperature boundary conditions and is localised around the fault. In this case, the peak of the convection cell has also moved closer to the extents of the model. This result is not particularly intuitive and could have significant implications in geothermal applications, as such effects could drastically influence drilling decisions and production operations.

Another question arises as to the role of fault orientation in the reservoir. It was previously discussed that the contribution of the geometry on the stresses in Equation 2.9 can be considered negligible. The bifurcation curves are not expected to differ even with the inclusion of a dipping fault, and would follow those in Figure 5.2a. Following this analysis, steady state convection patterns would not be expected to differ from the cases where horizontal faults are considered. However with the discovery of heat localisation at higher Gruntfest numbers in the previous section, it is observed that shear heating dramatically affects the steady state convective patterns in the system. The results are not mesh-sensitive and has been proven in mesh sensitivity analyses presented in earlier chapters (see Figure 3.6). In this analysis, a near-surface reservoir with dimensions 1000m and 2000m (width and length, respectively) containing a single fault dipping at shallow angles (10°) is considered. Table 5.3 details the parameters used in this scenario.

5.3 Shear Heating Changes the Pattern of Convection

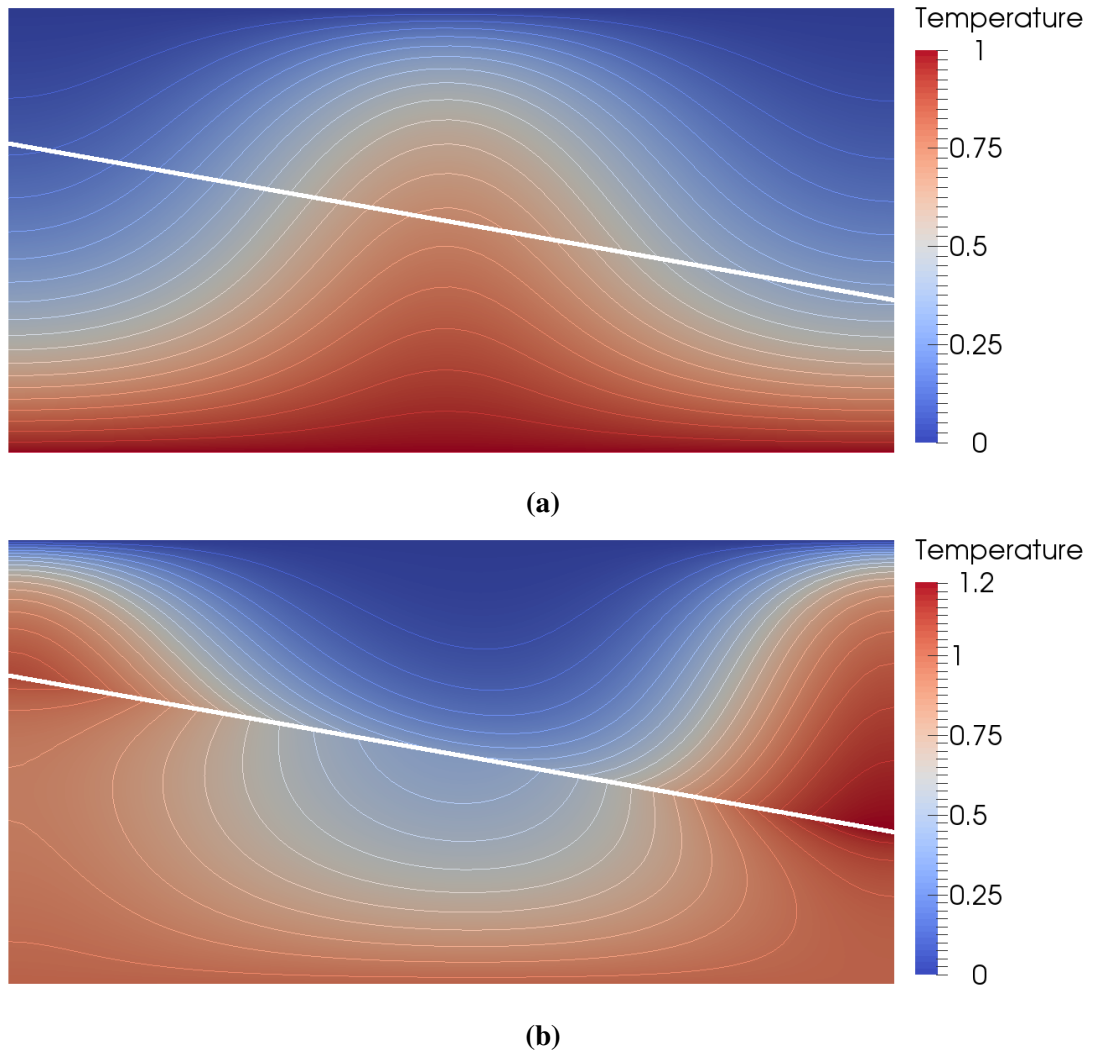


Fig. 5.6 Temperature profiles illustrating different convection patterns and normalised temperature isotherms with and without the presence of shear heating. The white gap between the reservoirs outline the fault of thickness 10m, and isotherms follow the temperature profiles. a) Convection profile for the case of no shear heating (i.e. $Gr = 0$). In this solution, the geometry of the fault is not acknowledged. b) Steady state temperature for $Gr = 1 \times 10^{-2}$. Note the non-symmetrical convection cells due to heat localising along the fault, as well as the upwelling plumes rising closer to the surface of the model.

5.4 Discussion

The steady state temperature profiles obtained for this problem are shown in Figure 5.6, highlighting the obvious differences with and without the consideration of shear heating. In the first example devoid of mechanical dissipation, the expected convective pattern is obtained. The presence and geometry of the fault is not seen to affect the steady state solution (Figure 5.6a). The second scenario is of $Gr = 1 \times 10^{-2}$, and this result shows that shear heating has dramatically changed the expected steady state convective patterns of the system. In particular, this specific example displays a localised hot zone where the temperature in the fault has exceeded the given boundary condition ($T > 1$), displayed in Figure 5.6b. The convective flow strongly affects the heat signature of the fault and does not lead to the expected hot zone around the fault, but rather concentrates the heat in a particular area. Such a temperature profile, if it had been inferred from geophysical data, could have been easily interpreted as an indication of a radiogenic heat source at that particular location. This interesting finding draws attention to the importance of understanding the impact of creeping faults in reservoirs.

5.4 Discussion

Shear heating has been shown to exceed the given temperature boundary conditions at given Gr values (see Figure 5.6b and 5.5). It is postulated if the fault could become the primary heat source for convection in a reservoir, instead of the classical scenario where heat from basement rocks are taken as boundary conditions? If so, what are the velocities, geological conditions, and material properties required for such systems? The ability to constrain such questions and the identification of key parameters have been made possible with the development and use of this novel stability analysis method, detailed in Section 3.2.

In this section, the results for the effect of shear heating from a steadily creeping fault are presented, on both the onset and pattern of convection. Firstly, shear heating is found to lower the critical permeability needed for convection to occur. This new finding has significant implications, especially in geological reservoirs where creeping faults may be present. Secondly, the coupling of advective and diffusive processes can cause heat to localise along the fault. These results differ from the traditional patterns expected around the critical permeability values of the system for systems where shear heating is not considered.

This fundamental study has opened the door to many potential future investigations. In particular is the consideration of multiple faults. In this study, only a single fault is considered for both the horizontal and dipping cases, but the the role of multiple faults in a reservoir is speculated. It was observed that heat localisation could occur in the scenario of both a horizontal fault (Figure 5.5) and dipping fault (Figure 5.6). Whilst the boundary conditions and material properties (i.e. fluid and solid properties) were identical to each other (see Table 5.1 and Table 5.3 for comparison), slightly

5.4 Discussion

varying geometrical conditions drastically changed the expected steady state solution (see Section 5.3). Following this outcome, it would be valuable to investigate the scenario where multiple creeping faults are present, and their relationship to the diffusive and advective processes in the reservoir. These results could have considerable significance for geothermal settings located in a graben, for instance, where the system is characterised by actively creeping faults. Building on these findings could lay the foundation for more questions and the possibility of future work to investigate the short term effects at engineering timescales. For example, what would be the response of the reservoir when production and injection wells are introduced into the system, if production wells are located close to the localised heat source from creeping faults? If heat rejection wells are placed in convective downwellings, how sustainable would the system be? Understanding such relationships in complex reservoirs can greatly contribute to optimising injection/extraction protocols in geothermal operations, for which the methodology now exists to investigate such questions.

In this thesis, one of the major assumptions is that the fault's total displacement is considered to be negligible compared to the overall length of the reservoir, but moving at a sufficient velocity to generate enough heat (see Section 5.1). The question then arises as to the behaviour of convection when the rate of creep becomes significant, and convection cells are displaced by the moving fault. It would be interesting to investigate if this problem has a steady state solution, and what key parameters govern the fault in such a case. Such findings could be meaningful especially when the location of the convective upwellings is desired, as it could influence the placement of injection and extraction wells.

This chapter demonstrates that the consideration of shear heating could have significant implications for geothermal operations as the evidence of preexisting physical processes could optimise energy production. The understanding of past physical processes provide information of in-situ conditions, and this knowledge coupled with the physical processes occurring at engineering timescales, can facilitate efficient energy extraction and production in geothermal reservoirs.

Chapter 6

Towards THMC: A Soultz-sous-Forêts Case Study

Faults have been shown to geometrically play a role in pinning convection cells (Reid et al., 2012), and steadily creeping faults have a considerable impact in altering the onset and pattern of convection (see Chapter 5). These two aspects can fundamentally influence the modelling of faulted geothermal reservoirs. In this chapter, such a case is investigated in a realistic geological setting at Soultz sous Forêts from a coupled thermo-hydro-mechanical (THM) perspective. This chapter focuses on a specific fracture zone and its effects on the heat and fluid flow processes in the reservoir.

6.1 Geological Setting and Geothermal Observations

The Soultz-sous-Forêts geothermal resource is located in the Rhine Graben in Europe, and represents the target of the European Hot Dry Rock project. The Graben was formed as a result of alpine orogeny in the European Cenozoic rift system (Ziegler, 1992). Mesozoic and Cenozoic sediments overlay the top 1400m of a Paleozoic granitic basement, which extends down to 5000m (Cautru, 1988; Pribnow and Schellschmidt, 2000). Prominent large-scale north-south striking faults are identified to originate in the granitic basement and extend up through the sedimentary cover (Rousset et al., 1993). The large quantity of temperature data, fracture networks, seismic activity, and chemical alteration history obtained from geophysical data and borehole logs indicate that coupled thermo-hydro-mechanical-chemical (THMC) processes are present in such a setting. Field evidence of these processes have been thoroughly analysed and a brief summary is presented below.

6.1.1 Evidence of Mechanical Deformation

Since the formation of the Rhine Graben, various rift segments have experienced changes in the stress field and still remain tectonically active today (Ziegler, 1992).

6.1 Geological Setting and Geothermal Observations

Recent seismic data indicate that vertical movement in the graben is attributed to ongoing subcrustal upwelling, supported by the presence of geothermal anomalies, seismic activity, and recent neotectonic movements (Buchmann and Connolly, 2007; Illies, 1972). The four major stress field re-orientations which alternated between the compressional and extensional regime could have triggered the reactivation of prior fault margins (Bergerat, 1987; Larroque and Laurent, 1988), and active faults appear to creep at a continuous rate without any major seismic activity (Illies, 1972; Illies and Greiner, 1978). Albeit the many stress re-orientations since the creation of the graben, the southern Rhine Graben area is currently characterised by normal and strike-slip faulting movements (Plenefisch and Bonjer, 1997).

Various scales of deformation are present at Soultz, ranging from large scale faults (e.g. Soultz and Kutzenhausen) to small scale fractures observed in borehole imaging techniques. The aperture and orientations of fracture clusters found in boreholes indicate complex deformation history and stress fields (Sausse et al., 2010). Although major large scale faults play a role in enhancing heat and fluid flow in the Graben, of particular interest are the small scale fractures in the granitic basement. Structural and geometrical data of these fractures obtained from well log analyses, microseismicity interpretation and hydraulic well stimulation (Dezayes et al., 2010; Sausse et al., 2010) confirm the presence of fluid flow circulating within faults and fracture zones, interpreted from a temperature profile obtained from well GPK2 (Figure 8 of Genter et al. (2010)). Due to the focus on hydrothermal flow, the terms 'fracture zone' and 'fault' are often used interchangeably. This points to the need to investigate the role of faults on hydrothermal convection.

6.1.2 Evidence of Hydrothermal Convection

At Soultz, prominent hot and cold upwellings are found at both regional and local scales. Homogeneously paired hot-cold patterns at depths of 800m are approximately 20km apart on a regional scale (Pribnow and Schellschmidt, 2000), but exhibit different characteristics on a local scale. A non-homogeneous distribution of convective up- and down-wellings are found at a scale of a few kilometres (see Figure 6.1), where hot upwellings are seen to concentrate around fault zones (Bächler et al., 2003).

Temperature information obtained from well data (GPK2) confirms the presence of hydrothermal convection and asserts the influential role of faults acting as pathways for heat and fluid transport. Heated fluid travels upwards through sub-vertical fracture networks and is circulated in the sediments (Pribnow and Schellschmidt, 2000). In Figure 6.2, temperature gradients are approximated at three instances along the profile. The highest branch (closest to the surface) has the highest thermal gradient, which has been interpreted as the diffusion of heat from a high convective heat source below (Vidal et al., 2015). The middle branch has an extremely low thermal gradient, implying the vertical flow of fluid up to the sediments, and the lower branch has a gradient

6.1 Geological Setting and Geothermal Observations

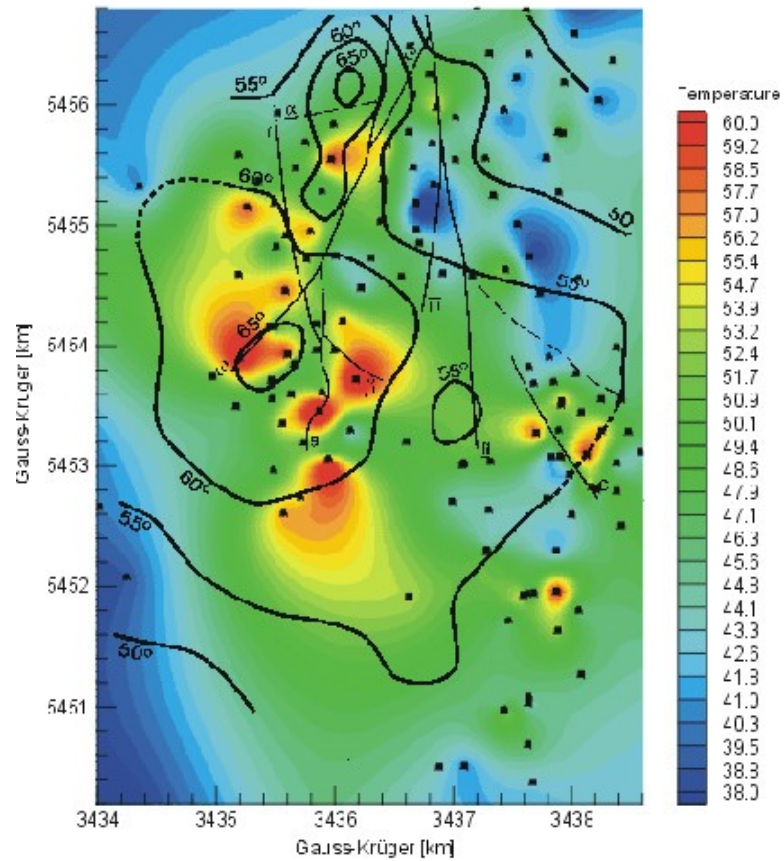


Fig. 6.1 Local temperature scale of Soultz; 1km scale, 500m depth. (Coloured version from (Bächler et al., 2003), personal communication.)

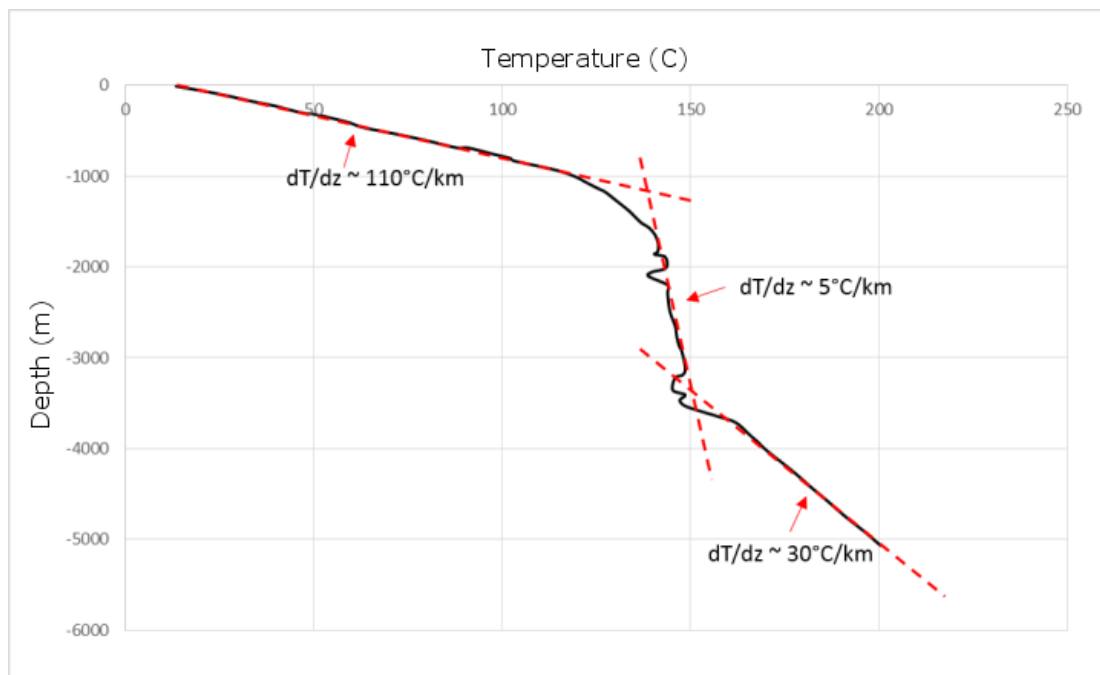


Fig. 6.2 Temperature profile obtained from well GPK2, data source from Genter et al. (2010).

6.2 Compilation of Previous Models

similar to the normal geothermal gradient. The backflow of temperature located at depths of approximately 2100m and 3500m are thermal signature of fault zones (Vidal et al., 2015). The change in geothermal gradient at approximately 1400m depth could most probably be attributed to the contrast in permeability and thermal conductivity of the sediment-basement interface, where a highly altered granitic basement is overlaid by clay sediments (Pribnow and Clauser, 2000; Pribnow and Schellschmidt, 2000; Schellschmidt and Clauser, 1996).

Of particular interest is the fault located at 3500m depth. It is coincidentally located at the interface between two changing geothermal gradients, without any major changes in geological units or material properties (Hooijkaas et al., 2006). It is investigated whether this fault could be the key parameter that governs the existence of convection.

6.1.3 Convection in the Upper Reservoir

Vidal et al. (2015) proposes a conceptual model of a local convective cell with a sub-vertical fracture network controlling fluid circulation, especially between 1400m and 3500m depth in the granite, termed as the 'upper reservoir'. This corresponds to the upflow of hot fluid through the granite and its diffusion into the sediments, seen in Figure 6.2. The lithology of these upper-lying sediments, sediment-granite interface at 1400m, and granitic host rock have been studied extensively through petrographical sections of lithology, fracture orientation, aperture, and hydrothermal alterations (Dezayes et al., 1995; Hooijkaas et al., 2006; Sausse, 2002; Sausse et al., 2006; Vidal et al., 2017, 2015). Additionally, considerable information is present and various models have been analysed to understand physical processes occurring in the lower reservoir (Dezayes et al., 2004, 2010; Ledésert et al., 2010; Sausse et al., 2010). However, the interface between the upper and lower reservoir has not yet been fully understood, particularly the fault at 3500m depth.

The fracture conditions at this interface documented by Sausse et al. (2010) and Dezayes et al. (2010) indicate a contrast in hydrothermally altered granite, where the upper boundary predominantly consists of abundant vein alterations while biotite-amphibole rich granite dominates the lower boundary.

6.2 Compilation of Previous Models

Extensive studies have investigated the behaviour of convection on both regional and local scales using numerical models (Benderitter and Elsass, 1996; Bächler et al., 2003; Carlier et al., 1994; Clauser and Villinger, 1990; Kohl et al., 2000; Pribnow and Schellschmidt, 2000). In these studies, there have been two main approaches: a homogeneous approach in which convection is dependent on the average permeability of geological units (e.g. Carlier et al., 1994; Magnenet et al., 2014), and a fractured

6.3 Motivation and Aim for This Study

approach in which fault permeability is taken into account (e.g. Bächler et al., 2003). This section presents an overview and highlights the results of the two approaches.

6.2.1 Homogeneous vs. Fractured Approaches

Numerical studies have been performed to understand the effect of convection in large-scale geometries, where homogeneous (i.e. single) permeability values were assigned to a single strata to represent various geological lithologies. Carlier et al. (1994) investigated the permeability required for convection to occur in the reservoir was in the order of $k = 10^{-14}m^2$, with the reservoir dimensions measuring approximately 60km in length and 5km in depth.

At Soultz, Magnenet et al. (2014) examined a steady state solution of a convective system from a simplified two-dimensional numerical model, with dimensions 10km in length and 5.3km in depth. Focusing on the rich rheologies of rocks and brine, the model assumed homogenized horizontal layers. For natural convection to occur in this reservoir, the minimum permeability required was also in the order of $k = 10^{-14}m^2$, where a periodic pair of convection cells measured approximately 2.6km in width. Whilst this approach captures the essential mode of heat transfer in the Rhine Graben on a regional scale, it is at odds with the observation on the smaller scales where localised upwellings and downwellings can be identified at much shorter wavelengths (Bächler et al., 2003). This is particularly obvious around fault zones and their intersections (Figure 6.1).

In the fractured modelling approach, numerical models considering fault geometry and material properties were included in order to observe its effects on convection in the reservoir. The work of Bächler et al. (2003) highlights the importance of fault permeability at Soultz, particularly in subvertical faults which facilitate natural up- and down-welling flow in the Rhine Graben. In this study, convection was found to occur at values of $k = 4.8 \times 10^{-14}m^2$ for a fault width of 200m. Geophysical evidence from gravity data also support fractures controlling fluid flow (Baillieux et al., 2014), and large-scale temperature anomalies can be attributed to the intersection of several highly permeable sub-vertical faults, notably the Kutzenhausen and Soultz Fault Systems, for instance.

6.3 Motivation and Aim for This Study

Figure 6.2 indicates temperature deviations at depths of approximately 3242m and 3514m from the GPK2 wellbore. These correspond to major fracture zones which, interestingly, exhibited low permeability during low-pressure hydraulic tests (Jung et al., 1995). Information from the GPK1 wellbore identifies a fracture zone at 3492m which was a dominant permeable structure (Evans et al., 2005). Although this fracture zone is not recorded in GPK2 logs, its location at the intersection of changing temperature

6.4 Materials and Methods

gradients is notable.

The aim for this study is to investigate how this fracture zone may or may not control the character of convection in the upper-lying strata.

6.4 Materials and Methods

The numerical tool used in this study is REDBACK (Poulet et al., 2016), following the workflow described in Chapters 4 and 5. This study investigates the physical processes responsible for the convection pattern observed, trying to first explain it from a simple hydrothermal perspective, and with the consideration of more processes as required. All equations solved (i.e. mass and energy balance) are detailed in Section 2.3.

6.4.1 Model Parameterisation

In order to investigate the effects of THM couplings without the additional complexity and drivers from the geometry and boundary conditions of the real geological scenario, this modelling study is based on a representative but simplified convection cell pinned by sub-vertical fracture zones. As such, the geological drivers are parameterised by the homogeneous material properties of these fracture zones, mainly by their dimensionless numbers (Le , Gr). The sub-vertical faults in the model are assumed to be made up of multi-scale fracture networks which connect the overlying sediments and permeate the granitic basement rock. For simplicity, a representative 2D vertical cross-section is taken through the faults, which are assumed to extend infinitely in the third dimension so any end-effects of the faults are ignored. In order to close the fault network, these sub-vertical faults are assumed to be connected horizontally at depths of 1400m and 3500m, respectively representing the interface between overlying sediment and granitic rock (1400m), and the fault of interest (3492m). In addition, the fracture network is homogenised by an effective permeability which is assumed to be isotropic.

Three rock lithologies are represented in the model; the granitic host rock and upper-lying sediments, the fracture network, and the granitic basement. In order to understand the role of the fracture network affecting fluid flow processes, the study focuses on a conceptualised zone of interest of 5km depth, including the representative convection cell described above (see model geometry in Figure 6.3).

At this depth, it is acknowledged that bottom boundary conditions are extremely complex and characterised by contrasting mineral assemblages and fracture clusters. However the primary focus is of the characteristics of the fracture zone located at 3492m depth and its influence on the convection processes above this depth, therefore a bottom temperature boundary condition generalised from the bottom hole temperature of GPK2 (Figure 6.2) is adequate. Material properties are chosen based on previous modelling studies (e.g. Bächler et al., 2003; Carrier et al., 1994; Magnenet et al., 2014),

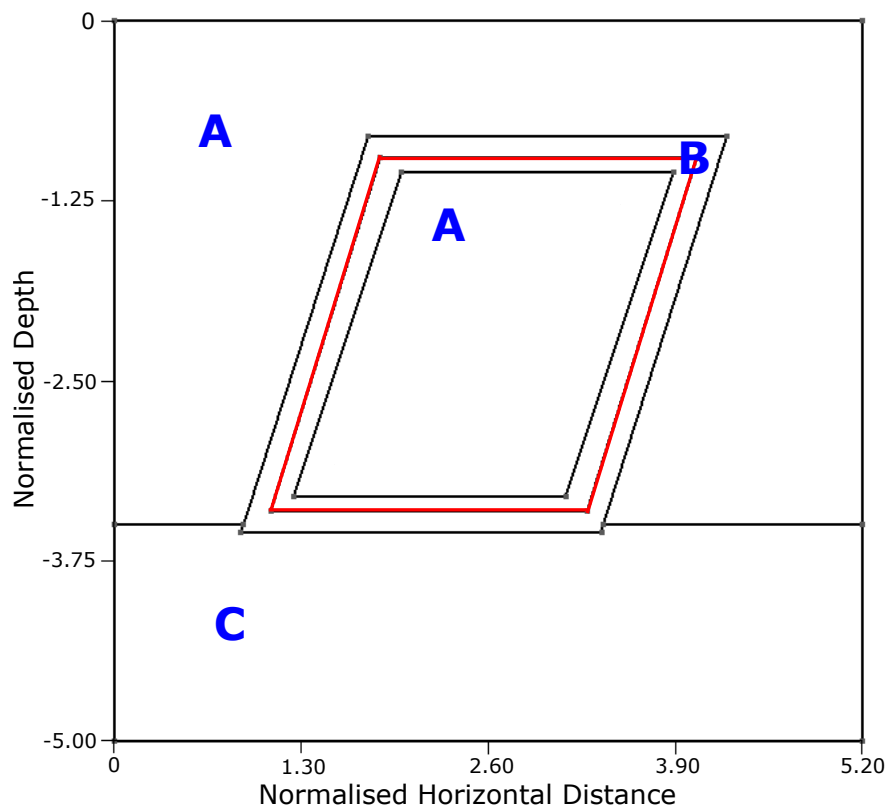


Fig. 6.3 Conceptual mesh geometry used in this study. Three rock lithologies represented in the model are: the granitic host rock (A), fault network (B) with the centre of the fault zone marked in red, and granitic basement (C). Model dimensions are 5km in depth and 5.2km in length, indicated by dimensionless values.

6.4 Materials and Methods

Table of Parameters for matching the Temperature Profile of GPK2			
		Real Values	Dimensionless Values
Geometry	Height	5000 (m)	5
	Length	5200 (m)	5.2
	Fault width	370 (m)	–
Boundary Conditions	Temperature top	293 (K)	0.0
	Temperature bottom	473 (K)	1.0
	Pressure top	1E+05 (Pa)	2.04E-03
	Gravity	9.8 ($m \cdot s^{-1}$)	-1.03
Fluid Properties	Thermal expansion coefficient	7E-05 (K^{-1})	1.26E-02
	Compressibility	4E-10 (Pa^{-1})	1.96E-02
	Viscosity	1.2E-04 ($Pa \cdot s$)	–
	Density	1000 ($kg \cdot m^{-3}$)	1.0
	Specific heat	1000 ($J \cdot kg^{-1} \cdot K^{-1}$)	–
	Permeability (A)	1.84E-17 (m^2)	1E-03
	Permeability (B)	2.30E-15 (m^2)	1e-05
	Permeability (C)	3.68E-16 (m^2)	5e-05
Solid Properties	Thermal expansion coefficient	1E-06 (K^{-1})	1.80E-04
	Specific heat	1000 ($J \cdot kg^{-1} \cdot K^{-1}$)	–
	Compressibility	2E-10 (Pa^{-1})	9.82E-03
	Density	2650 ($kg \cdot m^{-3}$)	2.5
	Porosity	0.01	0.01
	Thermal conductivity (A)	2 ($W \cdot m \cdot K$)	–
	Thermal conductivity (B)	2 ($W \cdot m \cdot K$)	–
	Thermal conductivity (C)	6 ($W \cdot m \cdot K$)	–

Table 6.1 Table of parameters used for the best fitting temperature profile, matching that of GPK2 (see Figure 6.5).

where permeability and thermal conductivity values are generalised over each rock type. Table 6.1 details the parameters used in this study.

This study follows the approach of Vidal et al. (2015), who showed that such parameterised models are well suited to understand the driving phenomena at play. This prominent fracture zone at 3492m depth has been identified to have a thickness of 8m (Dezayes et al., 2010). No direct permeability values have been derived for this fracture zone, but an equivalent porous medium (EPM) permeability was obtained from spinner log analyses, performed in the open hole section containing this fault Evans et al. (2005). The EPM permeability of this section was $3 \times 10^{-16} m^2$, and decreased to $1.5 \times 10^{-17} m^2$ when the fault was excluded from hydraulic testing. Spinner logs indicate that almost all of the flow occurred at this fracture zone, therefore in this study, an end-member upper limit scenario is assumed where all the flow is entirely governed by this fault at 3492m. Following this, the permeability of this zone can be inferred from the difference between the inclusion and exclusion tests Evans et al. (2005), where the value of $2.85 \times 10^{-16} m^2$ can be taken as a reasonable estimate for this fracture zone.

6.4.2 Mesh Sensitivity Analysis

In order to trust the simulation results, a mesh sensitivity analysis for the geometry described (Figure 6.3) is performed beforehand in order to determine the number of elements in the mesh that should be used in this study. Of particular interest are the

6.5 Results

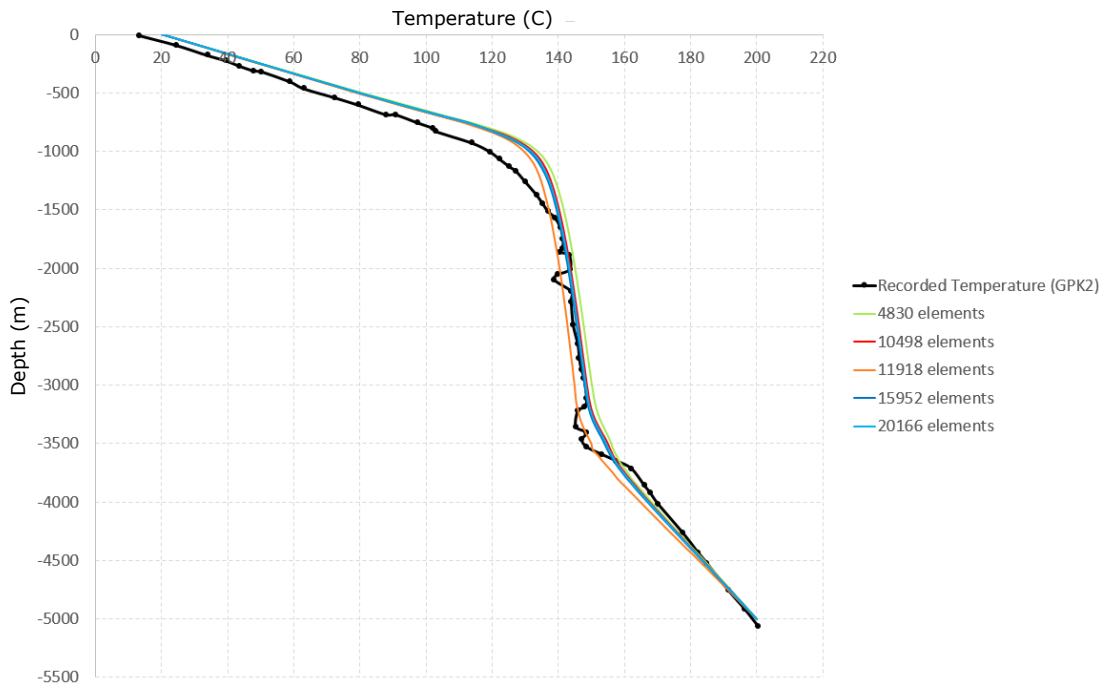


Fig. 6.4 Mesh sensitivity analyses performed on the mesh with geometrical dimensions listed in Table 6.1, plotted against the recorded temperature profile of GPK2. Numerical convergence of the solution is reached at approximately 11,000 elements.

fluid and heat flow processes within the fault, pointing to the necessity to sufficiently characterise this feature. For this sensitivity analysis, mesh geometry and values of material properties are kept constant while the number of elements in the mesh are varied, with extra focus on the fault.

In this model, the temperature profile of GPK2 is used to quantify numerical convergence. Steady state temperature results varying the number of mesh elements are plotted against GPK2 data and a slight oscillation of results is observed (see Figure 6.4). Numerical convergence is seen to occur with approximately 11,000 elements, however a value of 15,000 is used to ensure reliable results.

6.5 Results

This section presents the results of this study, first by matching the temperature profile of GPK2 using the traditional hydrothermal convection equations.

6.5.1 TH Model

In this fundamental analysis, the aim is to reconcile the permeability values used in previous studies ($1 \times 10^{-14} m^2$) to the inferred realistic value of $2.85 \times 10^{-16} m^2$, whilst fitting the temperature profile of GPK2 as closely as possible. An average value of the order of 10^{-15} is chosen as an initial attempt. In this scenario, temperature boundary

6.5 Results

conditions at the top and bottom of the model are imposed from GPK2 data, and a minimum width of 370m is derived by trial and error to sustain the temperature profile obtained in Figure 6.5. With these conditions, the temperature profile obtained sufficiently matches that of GPK2. Given the inverse relationship between fault width and permeability, the unrealistically large value of 370m was expected. Bächler et al. (2003) used a higher value for permeability, but still obtained a fault width of 200m. Clearly, some inconsistencies remain between the observations and the numerical models used to model hydrothermal convection.

Recent information of fracture aperture and thickness show that some of the model assumptions are not in agreement with the observed values. Firstly, fracture zone thickness derived from borehole images in Soultz have been averaged to be approximately 12m (Dezayes et al., 2010). Genter et al. (2000) illustrates a conceptual lithofacies of the granite, spanning approximately 10m in width, consisting of a quartz-filled fault core surrounded by cataclased brecciated granite. Particularly for the fracture zone at 3492m depth, the thickness is found to be 8m (Dezayes et al., 2010). This value is a stark contrast to the 370m fault width used in the numerical model, which should therefore be reduced considerably. This would naturally require using higher permeabilities to compensate and still match the observed temperature profile. However, the permeability values used for the model are also relatively high ($2.30 \times 10^{-15} m^2$), and already fall outside the natural permeability estimated ($2.85 \times 10^{-16} m^2$) by one order of magnitude, even in the end-member scenario.

Another limitation to this approach is that the best fit for the temperature profile was obtained by directly plotting the temperature in the centre of the fault. This strongly idealised scenario remains an end-member case where the large vertical temperature gradient should be easily matched for realistic values of geometry and material properties. Realistic evidence suggests there is no 'single' fault zone, instead small fracture zones are interconnected to each other in small distances (e.g. Dezayes et al., 2010; Ledésert et al., 1993, 2010). Smaller widths however, will result in the localisation of fluid flow to thinner pathways. This decreased interaction with the rock mass/host rock will require higher temperatures and faster velocities to produce the same effect.

To address these issues, the permeability values required to produce the same temperature for decreasing fault widths are examined. The following section discusses the implementation and results of the analysis.

6.5.2 Fault Width and Permeability Analysis

Effect of Decreasing Permeability

As an initial study, the fault width of 370m is maintained whilst decreasing permeability values to observe its effect on the temperature profile. Figure 6.6 displays the temperature profiles taken at the core of the fault for decreasing permeability values.

6.5 Results

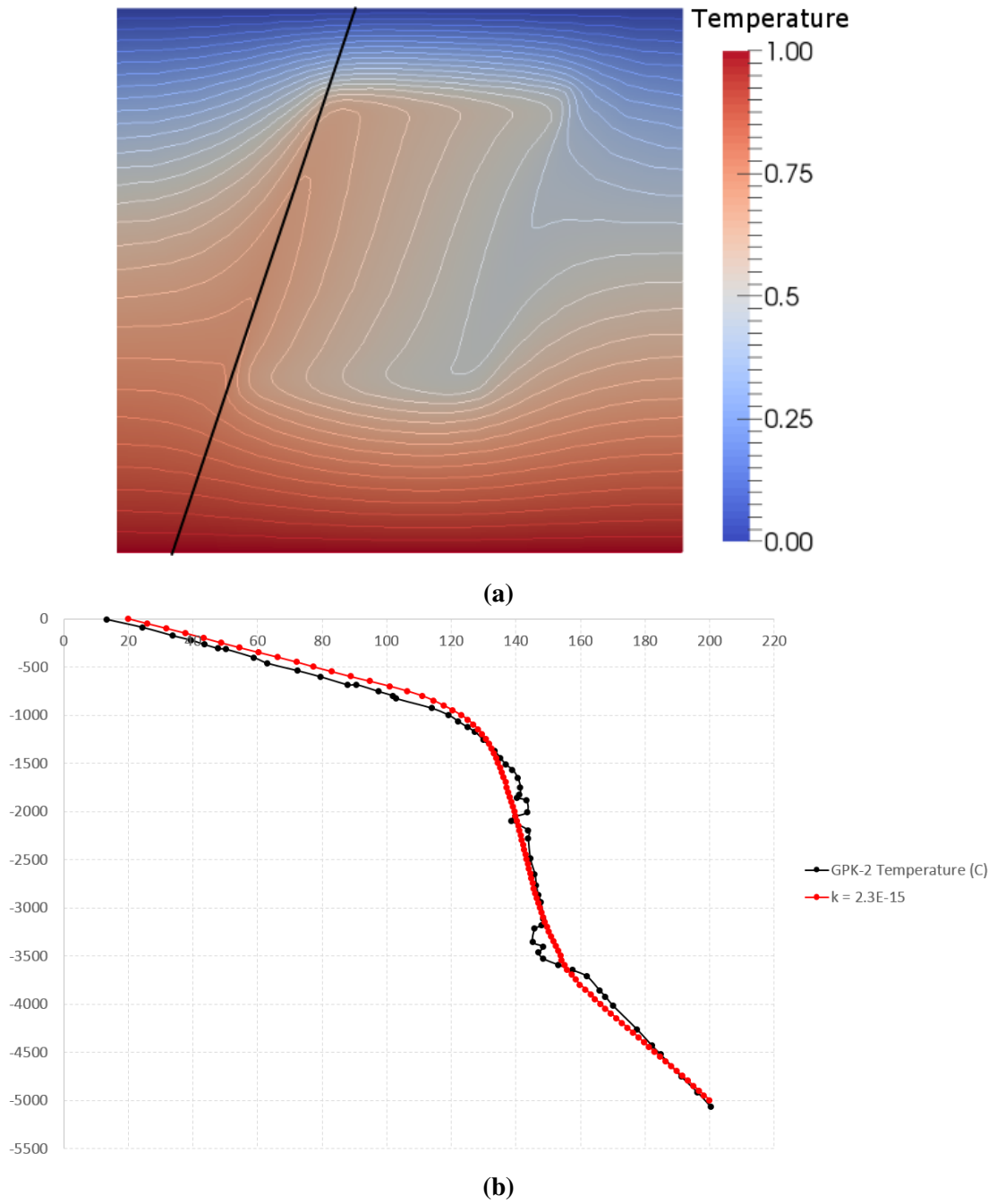


Fig. 6.5 Temperature profiles obtained using values provided in Table 6.1. a) Steady state simulation result using designated mesh geometry, displaying normalised temperature values and isotherms in the entire domain. Temperature values are taken along a digitised well bore, represented by the black line. b) Temperature profile of (a) plotted against GPK2 showing an adequate fit.

6.5 Results

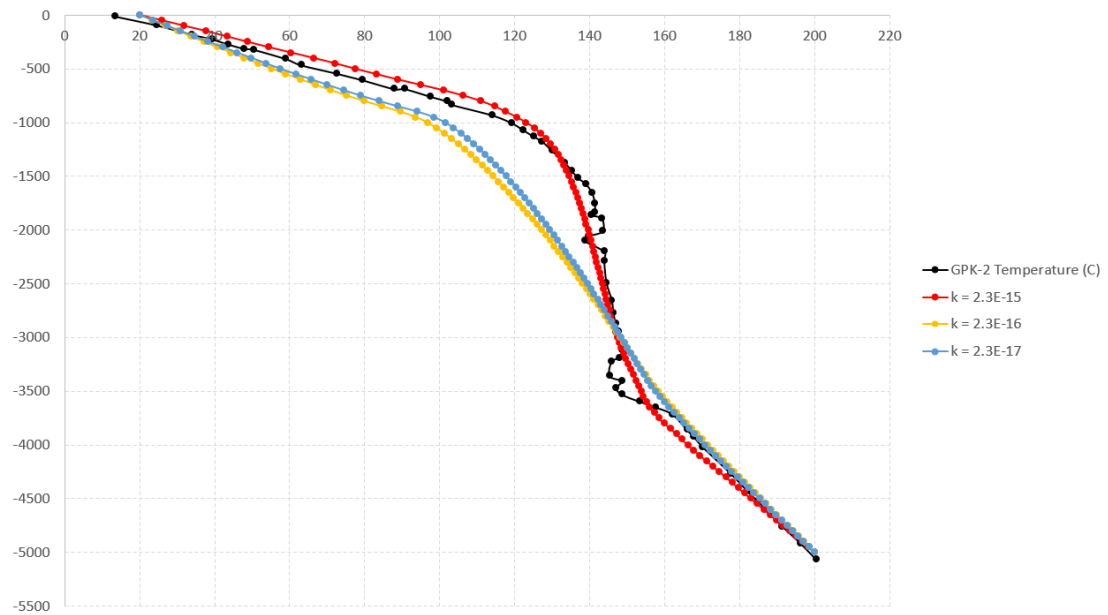


Fig. 6.6 Temperature profiles of decreasing permeability are plotted against the original well data of GPK2 (in black). In this scenario, the fault width is fixed at 370m and temperature data points are taken at the centre of the fault (see Figure 6.5a). With decreasing permeability, it can be observed that the behaviour of temperature tends towards the standard geothermal gradient, matching that of the [black] lower branch.

The best fitting temperature profile is the one presented in Section 6.5.1, obtained with a permeability value to the order of $10^{-15}m^2$. Although the temperature boundary conditions are fixed at the top and bottom of the model, the behaviour of the temperature profile significantly deteriorates with decreasing permeability, especially at depths between 1km and 3.5km. In these profiles, the gradient eventually diffuses to the standard geothermal gradient of approximately $30^{\circ}C/km$, matching that of the lower branch.

The permeability of the fracture at 3492m depth is approximated to be around the order of $10^{-16}m^2$, inferred in Section 6.5.1. Using this value, the temperature profile matches the lower branch but falls short of the profile obtained from GPK2 by almost 20° in other parts (see Figure 6.6). The next section presents the investigation of the permeabilities required for decreasing fault widths, with the consideration of only thermal and hydraulic (TH) processes.

Fault Width vs. Permeability Values

To perform such an analysis, a zone of 'diffused permeability' is first defined around the fault zone to match geological observations of damage zones around faults (e.g. Mitchell et al., 2011). This is represented using a bell-curve profile within the fault, where the largest value of permeability is in the centre and values gradually diffuse into the background value of the host rock. This portrayal of permeability allows the

6.5 Results

narrowing of fault widths without excessively refining the mesh, as well as accounting for the damage zone and/or hydrothermally altered permeabilities, following [Mitchell et al. \(2011\)](#) and [Genter et al. \(2000\)](#).

To obtain such a permeability profile, normalised permeability boundary conditions are first assigned to the background ($k = 0$) and centre of the fault ($k = 1$), outlined in red in Figure 6.3. The diffusion equation is then solved for the permeability variable over a transient simulation, where a fixed value of permeability is imposed as a boundary condition at the center of the bell-curve. The desired width can then be extracted by hand-picking a given timestep, and be read as an initial solution for a transient simulation. Real values of permeability can be computed by using the [real] permeabilities assigned to the fault and basement:

$$k_{real} = \frac{k_{fault} - k_{basement}}{\alpha}$$

where k is the permeability and α the constant of the Lewis number,

$$\alpha = \frac{\mu_{fo} \times c_{th} \times \beta_m^*}{\sigma_{ref}}$$

Single simulations are then run for each value of maximum permeability assigned to the centre of the fault. The methodology described allows the definition of a fracture zone with varying permeability (using a bell shaped distribution) over any desired total width. The value of the maximum permeability at the center of that fracture zone can then be selected independently.

This process is used to determine the total width W required for a given value of maximum permeability (k_c assigned to the center) to match the temperature profile at GPK2. In this analysis, three data points are obtained. For decreasing values of W from 370m, 309m and 275m, the permeability k_c is found to increase from $2 \times 10^{-15}m^2$ to $8 \times 10^{-15}m^2$ and $2 \times 10^{-14}m^2$ respectively (see Table 6.2). The high value of permeability for $W = 275m$ points to the futility of continuing this matching exercise for narrower values of W . Instead, the existing data points are then used to infer a power law relationship between k_c and W of the form $k_c = 163939W^{-7.754}$ (see Figure 6.7). In turn, this relationship indicates the incredibly high ranges of numerical values likely to be required for smaller values of W .

From this analysis, it can be seen that unrealistically high permeabilities are obtained for widths below 100m, which exceeds the derived value of the order $10^{-16}m^2$ by several orders of magnitude.

Therefore, the question remains unanswered: how is it possible to match the current temperature profile of GPK2 with a fracture zone of 8m, especially if the permeability of best case scenario is inferred permeability is at best in the order of $10^{-16}m^2$. The consideration of purely TH-processes is insufficient to explain such a phenomenon and obviously points to the presence of other physical processes that have been so far

6.5 Results

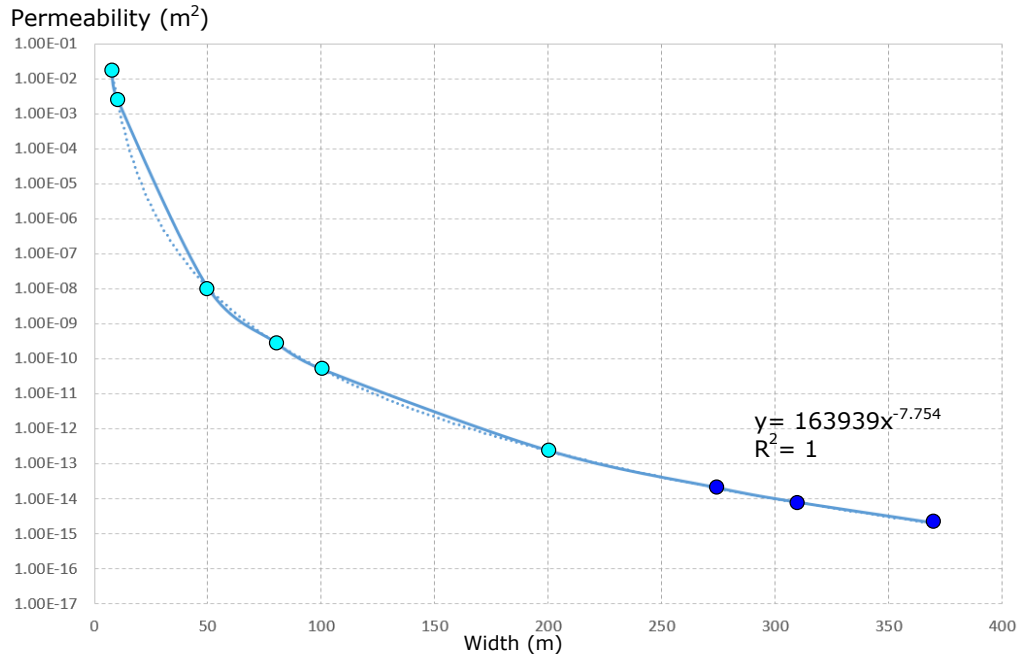


Fig. 6.7 Relationship of varying fault width to required permeability for sustainable convection. Data points obtained from simulations are indicated in dark blue and approximated permeability values are displayed in light blue, obtained using a power law relationship. Trendline and R-squared coefficient are displayed on the graph.

Width (m)	Permeability (m ²)
370	2.00×10^{-15}
309	8.00×10^{-15}
275	2.00×10^{-14}
200	12.36×10^{-13}
100	5.08×10^{-11}
80	2.87×10^{-10}
50	1.10×10^{-8}
10	2.89×10^{-3}
8	1.63×10^{-2}

Table 6.2 Table displaying data points obtained from simulations (black) and calculated permeability values (grey) using a power law fit. Fault width values range from what was used in the model (370m) to realistic values observed in well logs (8m). Permeability values obtained for widths below 100m are unrealistic.

6.5 Results

Table of Averaged Mechanical Values			
	Values Used in This Study	Documented Values	References
Frictional Coefficient	0.5	0.10 - 0.64	Plenefisch and Bonjer (1997)
Angle of Fault (°)	63	63	Dezayes et al. (2010)
Slip Rates ($mm \cdot yr^{-1}$)	0.5	0.1 - 0.7	Ahorner (1975), Buchmann and Connolly (2007)

Table 6.3 Table of mechanical parameters used to calculate values for Gruntfest. Values used in this study are representative and an averaged from those documented in literature.

neglected. The next step in this study is to consider mechanical deformation through the presence of creeping faults.

6.5.3 THM Model

Soultz is located in an active graben setting (Evans et al., 2005) and subsidence and slip rates of the Rhine Graben have been calculated to be in the order of $0.1mm/yr$ to a maximum of $0.5mm/yr$, with observed rates between $0.2mm/yr - 0.7mm/yr$ (Ahorner, 1975; Buchmann and Connolly, 2007). Well log data also identifies clusters of cataclastic shear structures around fracture zones in the reservoir (Evans, 2005). Following the study and results from Chapter 5, it was observed that the steady creep of active faults could trigger convection at lower permeabilities. This section investigates the effect of heat generated from realistic slip rate velocities and its effect on the overall convection behaviour in the model.

The introduction of mechanical deformation is expressed using the Gruntfest number Gr , defined in Equation 2.16. Following the assumptions for a fault experiencing steady creep described in Section 2.3, realistic slip rates can be expressed using Gr values (see map of Gruntfest numbers in Figure 5.4 documented in Chapter 5).

For this model, a reference slip rate of 10^{-16} is assumed, calculated from the averaged slip velocities Ahorner (1975) and lithospheric thickness (Geissler et al., 2010). Values for fault shear stress were calculated from averaged literature values (see Table 6.3), resulting in $\tau_n = 76.26MPa$. The yield stress can be determined using $\tau_y = C_0 + \mu(\tau_n - P_0)$, where C_0 is the cohesive strength, μ the frictional coefficient, and P_0 the pore pressure. Following the assumptions of (Plenefisch and Bonjer, 1997), the cohesive strength is assumed to be zero, thereby obtaining $\tau_y = 45.75MPa$. From these parameters, a Gruntfest number of $Gr = 6.84 \times 10^{-10}$ is determined (using Equation 2.16) for averaged values documented in literature.

6.5 Results

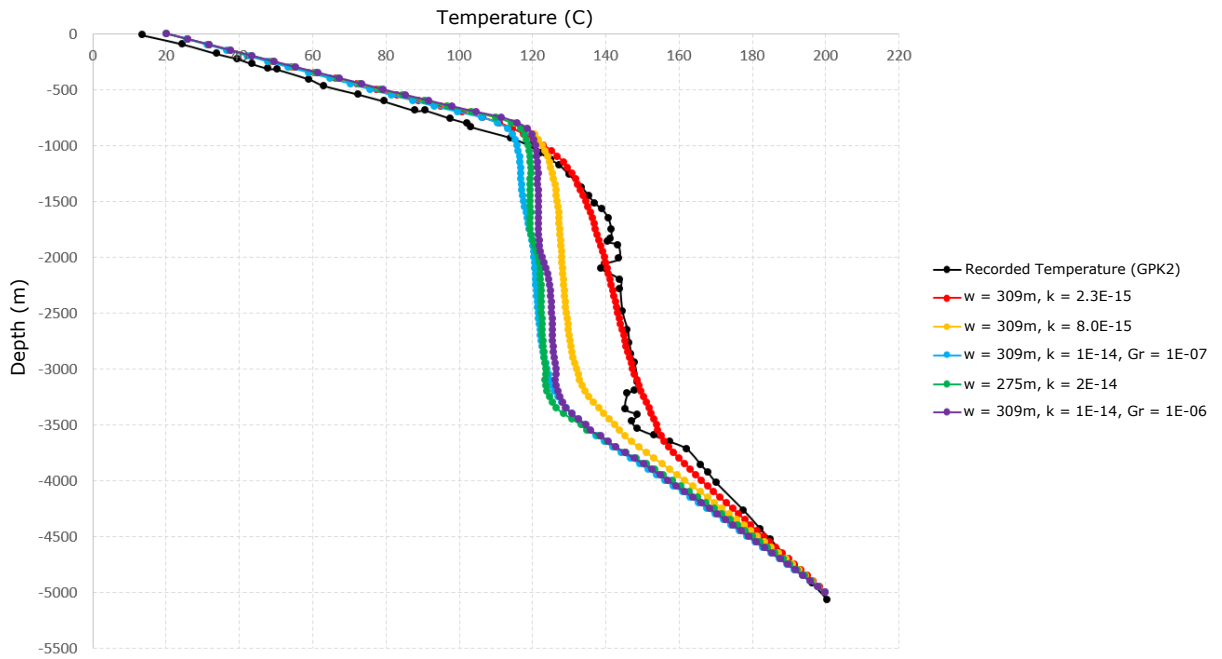


Fig. 6.8 Temperature profiles of varying fault widths and permeabilities. GPK2 temperature profile is displayed in black, and it is noted that the higher permeabilities required for narrower fault zones are numerically impossible to attain without upwinding schemes.

The results are displayed in Figure 6.8, where temperature profiles are plotted for some varying fault widths and permeabilities. In this figure, it is obvious that the temperature profiles are lacking in similarity compared to well data. Temperature discrepancies vary up to 20°C in some areas, especially in the vertical upflow. With the introduction of shear heating from averaged realistic parameters (Table 6.3), the temperature profile improves marginally but is still inadequate to suitably match the well data. Note the contrast in the orders of magnitude simulated for Gr values, where averaged realistic parameters give $Gr \sim 10^{-10}$ while values of $Gr \sim 10^{-06}$ and $Gr \sim 10^{-07}$ were used in the simulations. Attempts were made to run narrower widths, higher permeabilities and higher Gruntfest numbers, but could not match the temperature profile adequately with realistic values of material properties. This however, is not the focus of the study as the goal is to investigate and identify the key parameters of the driving processes in a system.

From this analysis of THM processes, it is apparent that shear heating is not the main driver characterising the heat and fluid flow processes in the reservoir. Rather, more complex processes are at play and the next step would be to consider chemical processes. It has been observed that chemistry plays an influential role in these settings, as hydrothermally altered zones are most prevalently found in and around fault zones (Ledéser et al., 1999, 2010; Schleicher et al., 2006).

6.6 Discussion

The aim of this study is to identify the driving parameters of the fracture zone at approximately 3500m depth. The exclusive simulation of TH processes in the reservoir was insufficient to adequately characterise the heat and fluid flow observations. It was observed that unrealistic high permeability values were required for sustaining convection in the reservoir when realistic fault widths were considered (see Table 6.2). Mechanical deformation was then included into the model, expressed by steadily creeping faults. Using values of slip rates documented in literature, the temperature profile was marginally improved but still failed to match the well data, differing by 20° particularly in the up-flow of fluid in the sub-vertical fault network. This study affirms the lack of physics represented by purely THM processes, and indicates the need of a THMC approach to describe such complex geothermal settings.

6.6.1 Evidence of Hydrothermal Alterations

Thorough analysis of macroscopic fractures at Soultz-sous-Forêts suggests that the granitic basement has experienced three hydrothermal alteration events (Genter and Traineau, 1996). Of particular interest is the alteration sequence which produced localised fractures. These organised clusters of fractures collectively characterises a structural trend which is evidence of extensive shear and have also been reactivated since the Tertiary (Dezayes et al., 1995; Genter et al., 1996). Controlled by such dynamic tectonism, these extensive fractured clusters have been identified as the main pathways through which fluid flows and circulation in the granitic basement is promoted (Evans, 2005; Kohl et al., 1995a; Lampe and Person, 2000).

Major pathways of fluid flow in the Soultz reservoir at have been identified to be through hydrothermally altered granite, localised around fracture zones. (Dezayes et al., 1995; Genter et al., 1996; Ledésert et al., 1999; Schleicher et al., 2006). Fluid circulation in these fracture zones have resulted in strong dissolution of primary minerals and precipitation/deposition of some altered minerals (Genter et al., 2010). Surprisingly, the most efficient fractures are characterised by a wide halo of alteration on either side of the fracture, even though poor connectivity exists between such fractures (Ledésert et al., 1993). The core of these fractures have been found to be filled with various hydrothermal minerals, consisting predominantly quartz, carbonates, clay minerals, and chlorite (Genter and Traineau, 1996).

6.6.2 Towards a THMC-Coupled Approach in Geothermal Settings

The identification of key parameters which govern the chemical processes in a tightly coupled system can be challenging. Lampe and Person (2000) suggest a fully-coupled

6.6 Discussion

THMC system where frequent reactivation of faults assists fluid flow, while the episodic mineralisation along and within faults obstructs flow through the reservoir. This concept is further investigated in this section. The use of a stability analysis such as the pseudo-arclength continuation method presented in Chapter 3 can help determine the critical value of key parameters once they are identified.

Shear heating and pore fluid pressurisation have been documented to be primary mechanisms resulting in fault slip (e.g. Garagash, 2012; Garagash and Rudnicki, 2003; Rice, 2006). Following this, in addition to the THM processes considered so far in this study, the idea of a mechanical-chemical oscillator (Alevizos et al., 2014) is proposed for the chemical process governing the fracture zone at 3492m. In this model, a fluid-saturated, steadily creeping fault under shear experiences fluid-release reactions triggered by the shear heating generated from the creeping faults. The theoretical conditions which govern this model are the dehydration of minerals and an endothermic chemical reaction, which could be found in realistic conditions at Soultz. At Soultz, strong dissolution and precipitation of minerals have indeed been found around fracture zones. Specifically, the fracture zone at 3492m depth contains precipitated clays and has been found to have experienced shear deformation, from the presence of illite and the evidence of cataclastic fragments, respectively (Evans, 2005; Genter and Traineau, 1996). Many geochemical studies have been performed to investigate the main chemical reactions occurring, and in particular the reaction $\text{K-feldspar} + \text{Al-clays} \rightarrow \text{illite} + \text{quartz}$ has been previously indicated as predominant in this particular fracture zone (Ledéseret et al., 1999) in order to apply this oscillatory model. The presence of illite can be expected to contribute to lowering the frictional coefficient of the fault, which could cause more slip on the fracture zone, which suggests an application of the chemo-mechanical oscillator. Higher shear heating temperatures could result from this slip, therefore triggering the $\text{K-feldspar} + \text{Al-clays} \rightarrow \text{illite} + \text{quartz}$ reaction.

The model in (Alevizos et al., 2014) describes a system where the fault movement and chemical reactions occur periodically due to the chemical and thermal feedback loops. From the evidence of cataclastic sheared features, episodic fault reactivation is proposed for the fracture zone located at 3492m depth. In such a model, the fault is stationary for most of the time which results in ambient low permeability. During its reactivation however, permeability could temporarily increase by several orders of magnitude, and fluid is driven through the fault. The presence of illite suggests a dissolution/precipitation reaction where more illite would contribute to more slip, until the heat from the reaction is depleted and the fault enters a stationary regime. Some of the compulsory conditions for the chemo-mechanical oscillator are deep, tectonically active environments (e.g. subduction zones), and despite the publications on the applications of this oscillator, none have been applied to such shallow environments. As such, the investigation of this fault in Soultz could be challenging as the environment

6.6 Discussion

is too shallow for the phenomenon to be confidently identified, and would have subtle signature should it be present. Although the use of a numerical stability analysis can assist to identify the key driving processes, the full study of such chemical processes is extremely complex and hence lies outside the scope of this thesis, but is proposed as future work. This study could be extended to simulating and evaluating the behaviour of the vertical fault network, to investigate if the temperature profile obtained from GPK2 is reproducible with a fully coupled THMC modelling approach. Such studies could greatly contribute to the understanding of a time-dependent permeability structure of the processes occurring at Soultz.

Chapter 7

Conclusions and Future Outlook

This thesis demonstrates the impact of active faults in geothermal environments, specifically on hydrothermal convection. The shear heating effect from a creeping fault's frictional resistance to movement is shown to play a significant role in changing the conditions for the onset of hydrothermal convection. The mechanical deformation of a creeping fault can be expressed as a heat source term in the temperature equation, characterised by the Gruntfest number Gr (Equation 2.16), defined as the ratio of heat generated from mechanical deformation to its thermal dissipation in the system. An exponential relationship is derived between Gr and the convection criterion (Equation 5.2), even for inappreciable deformation rates which are sufficient to lower the permeabilities at which convection is predicted to occur (Figure 5.2). This novel finding suggests that convection could be occurring in reservoirs where creeping faults are present, where for the same conditions the system would otherwise present a purely conductive pattern without the presence of such faults.

In addition to lowering the critical permeability predicted for the occurrence of convection, shear heating also changes the steady state pattern of convection (Figures 5.5 and 5.6). The coupling of advective and diffusive processes can result in the localisation of heat along the fault, which is particularly non-intuitive for a constant heat source. This can lead to a non-symmetrical solution of paired convective cells, where the extents of the convective upwelling shifts closer to the surface of the model at higher Gr values, with temperatures at the fault even exceeding given boundary conditions (Figures 5.5d and 5.6b). These results introduce a new possible interpretation for localised heat sources found in geophysical data. Instead of the classical interpretation of a radioactive heat source, such anomalies could be attributed to the coupled effects of creeping faults in hydrothermally active convective systems. These findings could be extended to investigate the competitive rates of heat generation, diffusion, and convective flow dominating heat localisation. In addition, further studies could be performed to investigate the behaviour of the pattern and onset of convection using more realistic geometries and material properties, to better understand the driving parameters behind extremely complex physical processes in realistic geothermal environments.

Quantitative assessments of the conditions required for the onset of hydrothermal convection were achieved using a numerical bifurcation analysis, with the implementation of a pseudo-arclength continuation method into a finite element geomechanics simulator, REDBACK, as discussed in Chapter 3. In harnessing both a mathematically-rigorous method and numerical capabilities of current simulators, the critical value required for the onset of convection can be identified (see Chapter 4), additionally tracing the evolution of the system from its diffusive to convective state. This method alleviates the issue of traditional numerical sensitivity analyses which are unable to accurately pinpoint the onset of convection, as a non-convecting transient simulation can be inconclusive especially when the system is close to criticality. The stability curves in Chapter 5 presented cases of perfect bifurcation which were in agreement with those previously derived using analytical methods (e.g. [Combarnous and Bories, 1975](#)), and furthermore showed a dependency on fluid compressibility where a pseudo-analytical solution (Figure 4.3b) was obtained (see Section 4.2). This workflow highlights the capability to identify the specific value of a critical parameter governing the instability of a system, and can be applied to a variety of other systems of interest.

The behaviour of convection investigated in non-symmetrical geometries showed that the onset of convection is not necessarily a single value, but is instead a transitional zone in the case of imperfect bifurcations (Section 3.5). In such cases, three behaviours were observed in the bifurcation curves with increasing amplitudes for non-symmetrical geometry (Figure 3.9). Firstly, no definite value can be determined for the onset of convection. Secondly, the curves diverge farther from the perfect bifurcation point (obtained with symmetrical geometry), and lastly, the mathematical solution along the supposedly diffusive branch is strictly $Nu > 1.00$ in such cases, as opposed to $Nu = 1.00$ for symmetrical geometries. This suggests that the solution for the onset of convection has to be arbitrarily defined through a visual analysis of the stability curves (see Figure 3.10). Indeed, there is no clear-cut mathematical value for the onset of convection in scenarios of non-symmetrical geometries, rather it is user-defined where the accuracy of Nu can be preserved (reducing decimals to $Nu = 1.00$) at the expense of lower permeability values (i.e. larger Le values), since the diffusive branch asymptotically tends to $Nu = 1.00$. These results imply that the classical solution of $Ra_c = 4\pi^2$, for example, is not valid when applied to realistic geometries.

This theoretical study of creeping faults was extended to a realistic geothermal setting at Soultz-sous-Forêts, where the influence of hydrothermal (TH) and hydrothermal-mechanical (THM) processes was investigated in the reservoir. In a conceptual case study, a specific fracture zone was investigated to determine the driving factors of convection occurring in the above reservoir (Chapter 6). Temperature profiles obtained from well data indicate the presence of hydrothermal convection from extremely high geothermal gradients (Figure 6.2), and the aim was to reconcile inferred numerical values of permeabilities (in the order of $10^{-14}m^2$) with those derived from hydraulic

tests ($10^{-16}m^2$) while producing the same temperature profile. The realistic profile was adequately matched (Figure 6.5) albeit with unrealistic fault widths. A permeability analysis suggests extremely high permeability values for convection to be sustainable at realistic fault widths (Table 6.7), which indicates that purely TH processes are insufficient to characterise the processes occurring in the reservoir. The inclusion of mechanics into the model was expressed by the constant heat source of creeping faults (Gr), but nevertheless could not reproduce the realistic temperature profile, falling short by $20^\circ C$ in some areas (Figure 6.8). Despite Soultz being in an active graben (Evans, 2005), this study indicates that shear heating is not the main driver in that reservoir. Finally, the contribution of chemical processes is investigated through the potential presence of a chemo-mechanical oscillator Alevizos et al. (2014), activated by fluid-release reactions within faults in the reservoir. A time-dependent permeability structure is proposed, which could be the driving mechanism at Soultz, where the heat generated from steadily creeping faults trigger chemical reactions. The dissolution of minerals significantly increases permeability for a limited time, which could explain the high permeabilities needed for convection to be sustainable in the reservoir at geological timescales.

This thesis has unravelled new understandings regarding the impact of creeping faults in geothermal reservoirs, the concept of the onset of convection, and also presented a numerical framework capable of quantitatively investigating the key parameters which govern instabilities in any given system. A preliminary case study of Soultz-sous-Forêts using such a tool proposed a novel concept in characterising the driving processes governing the reservoir. Such detailed understanding of complex THMC processes can be utilised to optimise injection and extraction protocols for geothermal energy production, and the methodology to tackle such questions now exists with the development of the workflow described in this thesis. In the future these tools can be used to provide insightful conclusions for currently poorly constrained field applications.

References

- Ahorner, L. (1975). Present-day stress field and seismotectonic block movements along major fault zones in Central Europe. *Tectonophysics*, 29(1-4):233–249. doi:[10.1016/0040-1951\(75\)90148-1](https://doi.org/10.1016/0040-1951(75)90148-1).
- Ahrens, J., Geveci, B., Law, C., Hansen, C., and Johnson, C. (2005). ParaView: An End-User Tool for Large-Data Visualization. In *Visualization Handbook*, pages 717–731. Elsevier. doi:[10.1016/b978-012387582-2/50038-1](https://doi.org/10.1016/b978-012387582-2/50038-1).
- Alevizos, S., Poulet, T., and Veveakis, E. (2014). Thermo-poro-mechanics of chemically active creeping faults. 1: Theory and steady state considerations. *Journal of Geophysical Research: Solid Earth*, 119(6):4558–4582. doi:[10.1002/2013jb010070](https://doi.org/10.1002/2013jb010070).
- Ayachit, U. (2015). *The Paraview Guide: A Parallel Visualization Application*. Kitware, Inc.
- Baillieux, P., Schill, E., Abdelfettah, Y., and Dezayes, C. (2014). Possible natural fluid pathways from gravity pseudo-tomography in the geothermal fields of Northern Alsace (Upper Rhine Graben). *Geothermal Energy*, 2(1). doi:[10.1186/s40517-014-0016-y](https://doi.org/10.1186/s40517-014-0016-y).
- Bartels, J., Cheng, L. Z., Clauser, C., Hurter, S., Kühn, M., Meyn, V., Pribnow, D., Ranalli, G., Schneider, W., and Stöfen, H. (2003). Applications. In *Numerical Simulation of Reactive Flow in Hot Aquifers*, pages 229–316. Springer Berlin Heidelberg. doi:[10.1007/978-3-642-55684-5_6](https://doi.org/10.1007/978-3-642-55684-5_6).
- Bénard, H. (1901). *Les tourbillons cellulaires dans une nappe liquide propageant de la chaleur par convection: en régime permanent*. Gauthier-Villars. doi:[10.1007/bf01703351](https://doi.org/10.1007/bf01703351).
- Benderitter, Y. and Elsass, P. (1996). Structural control of deep fluid circulation at the Soultz HDR site, France: a review. In *International Journal of Rock Mechanics and Mining Sciences and Geomechanics Abstracts*, volume 3, page 104A. doi:[10.1016/0148-9062\(96\)86872-0](https://doi.org/10.1016/0148-9062(96)86872-0).
- Bergerat, F. (1987). Stress fields in the European platform at the time of Africa-Eurasia collision. *Tectonics*, 6(2):99–132. doi:[10.1029/tc006i002p00099](https://doi.org/10.1029/tc006i002p00099).
- Bories, S. (1987). Natural Convection in Porous Media. In *Advances in Transport Phenomena in Porous Media*, volume 128, pages 77–141. Springer Netherlands. doi:[10.1007/978-94-009-3625-6_4](https://doi.org/10.1007/978-94-009-3625-6_4).
- Bower, K. and Zyvoloski, G. (1997). A numerical model for thermo-hydro-mechanical coupling in fractured rock. *International Journal of Rock Mechanics and Mining Sciences*, 34(8):1201–1211. doi:[10.1016/s1365-1609\(97\)80071-8](https://doi.org/10.1016/s1365-1609(97)80071-8).
- Browne, P. R. L. (1978). Hydrothermal Alteration in Active Geothermal Fields. *Annu. Rev. Earth Planet. Sci.*, 6(1):229–248. doi:[10.1146/annurev.ea.06.050178.001305](https://doi.org/10.1146/annurev.ea.06.050178.001305).

REFERENCES

- Buchmann, T. J. and Connolly, P. T. (2007). Contemporary kinematics of the Upper Rhine Graben: a 3D finite element approach. *Global and Planetary Change*, 58(1-4):287–309. doi:[10.1016/j.gloplacha.2007.02.012](https://doi.org/10.1016/j.gloplacha.2007.02.012).
- Bächler, D., Kohl, T., and Rybach, L. (2003). Impact of graben-parallel faults on hydrothermal convection—Rhine Graben case study. *Physics and Chemistry of the Earth, Parts A/B/C*, 28(9-11):431–441. doi:[10.1016/s1474-7065\(03\)00063-9](https://doi.org/10.1016/s1474-7065(03)00063-9).
- Carlier, C. L., Royer, J.-J., and Flores, E. (1994). Convective heat transfer at the Soultz-sous-Forêts Geothermal Site: implications for oil potential. *First Break*, 12(1285):553–560. doi:[10.3997/1365-2397.1994033](https://doi.org/10.3997/1365-2397.1994033).
- Cautru, J. P. (1988). *Coupe géologique passant par le forage GPK1 calée sur la sismique réflexion*.
- Charrier-Mojtabi, M.-C. and Mojtabi, A. (2005). Double-Diffusive Convection in Porous Media. In *Handbook of Porous Media, Second Edition*, pages 269–320. CRC Press. doi:[10.1201/9780415876384.pt3](https://doi.org/10.1201/9780415876384.pt3).
- Christensen, U. R. (2002). Zonal flow driven by strongly supercritical convection in rotating spherical shells. *Journal of Fluid Mechanics*, 470:115–133. doi:[10.1017/s0022112002002008](https://doi.org/10.1017/s0022112002002008).
- Christensen, U. R. and Aubert, J. (2006). Scaling properties of convection-driven dynamos in rotating spherical shells and application to planetary magnetic fields. *Geophysical Journal International*, 166(1):97–114. doi:[10.1111/j.1365-246x.2006.03009.x](https://doi.org/10.1111/j.1365-246x.2006.03009.x).
- Clauser, C. and Bartels, J. (2002). *Numerical Simulation of Reactive Flow in Hot Aquifers*. Springer Berlin Heidelberg.
- Clauser, C. and Villinger, H. (1990). Analysis of conductive and convective heat transfer in a sedimentary basin, demonstrated for the Rheingraben. *Geophysical Journal International*, 100(3):393–414. doi:[10.1111/j.1365-246x.1990.tb00693.x](https://doi.org/10.1111/j.1365-246x.1990.tb00693.x).
- Combarrous, M. A. and Bories, S. A. (1975). Hydrothermal Convection in Saturated Porous Media. In *Advances in Hydrosience*, volume 10, pages 231–307. Elsevier. doi:[10.1016/b978-0-12-021810-3.50008-4](https://doi.org/10.1016/b978-0-12-021810-3.50008-4).
- Coussy, O. (2003). *Poromechanics*. John Wiley & Sons, Ltd. doi:[10.1002/0470092718](https://doi.org/10.1002/0470092718).
- Degen, D., Veroy, K., and Wellmann, F. (2017). The Reduced Basis Method in Geosciences: Practical examples for numerical forward simulations. In *AGU Fall Meeting Abstracts*.
- Dezayes, C., Genter, A., and Gentier, S. (2004). Fracture network of the EGS geothermal reservoir at Soultz-sous-Forêts (Rhine Graben, France). *Geotherm. Resour. Council Trans*, 28:213–218. doi:[10.1016/j.jvolgeores.2010.07.001](https://doi.org/10.1016/j.jvolgeores.2010.07.001).
- Dezayes, C., Genter, A., and Valley, B. (2010). Structure of the low permeable naturally fractured geothermal reservoir at Soultz. *Comptes Rendus Geoscience*, 342(7-8):517–530. doi:[10.1016/j.crte.2009.10.002](https://doi.org/10.1016/j.crte.2009.10.002).
- Dezayes, C., Villemain, T., Genter, A., Traineau, H., and Angelier, J. (1995). Analysis of fractures in boreholes of Hot Dry Rock project at Soultz-sous-Forêts (Rhine graben, France). *Scientific Drilling*, 5(1):31–41. doi:[10.1029/97jb00626](https://doi.org/10.1029/97jb00626).

REFERENCES

- Diersch, H.-J. G. (2013). Variable-Density Flow, Mass and Heat Transport in Porous Media. In *FEFLOW*, pages 537–624. Springer Berlin Heidelberg. doi:[10.1007/978-3-642-38739-5_11](https://doi.org/10.1007/978-3-642-38739-5_11).
- Dieterich, J. H. (1978a). Preseismic fault slip and earthquake prediction. *Journal of Geophysical Research*, 83(B8):3940–3948. doi:[10.1029/jb083ib08p03940](https://doi.org/10.1029/jb083ib08p03940).
- Dieterich, J. H. (1978b). Time-Dependent Friction and the Mechanics of Stick-Slip. In *Rock Friction and Earthquake Prediction*, pages 790–806. Birkhäuser Basel. doi:[10.1007/978-3-0348-7182-2_15](https://doi.org/10.1007/978-3-0348-7182-2_15).
- Elder, J. W. (1967). Steady free convection in a porous medium heated from below. *Journal of Fluid Mechanics*, 27(1):29–48. doi:[10.1017/s0022112067000023](https://doi.org/10.1017/s0022112067000023).
- Evans, K. F. (2005). Permeability creation and damage due to massive fluid injections into granite at 3.5 km at Soultz: 2. Critical stress and fracture strength. *J. Geophys. Res.*, 110(B4):B04204. doi:[10.1029/2004jb003169](https://doi.org/10.1029/2004jb003169).
- Evans, K. F., Genter, A., and Sausse, J. (2005). Permeability creation and damage due to massive fluid injections into granite at 3.5 km at Soultz: 1. Borehole observations. *J. Geophys. Res.*, 110(B4):B04203. doi:[10.1029/2004jb003168](https://doi.org/10.1029/2004jb003168).
- Florio, B. J. (2013). The interaction of convection modes in a box of a saturated porous medium. *Journal of Engineering Mathematics*, 86(1):71–88. doi:[10.1007/s10665-013-9647-4](https://doi.org/10.1007/s10665-013-9647-4).
- Florio, B. J., Bassom, A. P., Fowkes, N., Judd, K., and Stemler, T. (2015). The nonlinear interaction of convection modes in a box of a saturated porous medium. *Physica D: Nonlinear Phenomena*, 301-302:48–58. doi:[10.1016/j.physd.2015.03.010](https://doi.org/10.1016/j.physd.2015.03.010).
- Florio, B. J., Bassom, A. P., Judd, K., and Stemler, T. (2017a). Interacting convection modes in a saturated porous medium of nearly square planform: a special case. *Journal of Engineering Mathematics*, 107(1):87–110. doi:[10.1007/s10665-017-9900-3](https://doi.org/10.1007/s10665-017-9900-3).
- Florio, B. J., Bassom, A. P., Sakellariou, K., and Stemler, T. (2017b). Interacting convection modes in a saturated porous medium of nearly square planform: four modes. *imamat*, 82(3):526–547.
- Garagash, D. I. (2012). Seismic and aseismic slip pulses driven by thermal pressurization of pore fluid. *Journal of Geophysical Research: Solid Earth*, 117(B4):n/a–n/a. doi:[10.1029/2011jb008889](https://doi.org/10.1029/2011jb008889).
- Garagash, D. I. and Rudnicki, J. W. (2003). Shear heating of a fluid-saturated slip-weakening dilatant fault zone 1. Limiting regimes. *Journal of Geophysical Research: Solid Earth*, 108(B2). doi:[10.1029/2001jb001653](https://doi.org/10.1029/2001jb001653).
- Gaston, D., Newman, C., Hansen, G., and Lebrun-Grandié, D. (2009). MOOSE: A parallel computational framework for coupled systems of nonlinear equations. *Nuclear Engineering and Design*, 239(10):1768–1778. doi:[10.1016/j.nucengdes.2009.05.021](https://doi.org/10.1016/j.nucengdes.2009.05.021).
- Geissler, W. H., Sodoudi, F., and Kind, R. (2010). Thickness of the central and eastern European lithosphere as seen by Receiver functions. *Geophysical Journal International*, 181(2):604–634. doi:[10.1111/j.1365-246x.2010.04548.x](https://doi.org/10.1111/j.1365-246x.2010.04548.x).

REFERENCES

- Genter, A., Evans, K., Cuenot, N., Fritsch, D., and Sanjuan, B. (2010). Contribution of the exploration of deep crystalline fractured reservoir of Soultz to the knowledge of enhanced geothermal systems (EGS). *Comptes Rendus Geoscience*, 342(7-8):502–516. doi:[10.1016/j.crte.2010.01.006](https://doi.org/10.1016/j.crte.2010.01.006).
- Genter, A. and Traineau, H. (1996). Analysis of macroscopic fractures in granite in the HDR geothermal well EPS-1, Soultz-sous-Forêts, France. *Journal of Volcanology and Geothermal Research*, 72(1-2):121–141. doi:[10.1016/0377-0273\(95\)00070-4](https://doi.org/10.1016/0377-0273(95)00070-4).
- Genter, A., Traineau, H., Dezayes, C., Elsass, P., Ledésert, B., Meunier, A., and Villemin, T. (1996). Fracture analysis and reservoir characterization of the granitic basement in the HDR Soultz project (France). In *International journal of rock mechanics and mining sciences & geomechanics abstracts*, volume 33, pages 69A–69A. Elsevier Science.
- Genter, A., Traineau, H., Ledésert, B., Bourguine, B., and Gentier, S. (2000). Over 10 years of geological investigations within the HDR Soultz project, France. In *Proceedings World Geothermal Congress*. Kyushu-Tohoku Japan.
- Gruntfest, I. J. (1963). Thermal Feedback in Liquid Flow: Plane Shear at Constant Stress. *Transactions of the Society of Rheology*, 7(1):195–207. doi:[10.1122/1.548954](https://doi.org/10.1122/1.548954).
- Hall, P. and Walton, I. C. (1979). Bénard convection in a finite box: secondary and imperfect bifurcations. *Journal of Fluid Mechanics*, 90(2):377–395. doi:[10.1017/s0022112079002275](https://doi.org/10.1017/s0022112079002275).
- Hayba, D. O. and Ingebritsen, S. E. (1994). The computer model HYDROTHERM, a three-dimensional finite-difference model to simulate ground-water flow and heat transport in the temperature range of 0 to 1,200 degrees C. Technical report, U.S. Geological Survey Water-Resources Investigations Report. doi:[10.1016/0022-1694\(86\)90106-x](https://doi.org/10.1016/0022-1694(86)90106-x).
- Hooijkaas, G. R., Genter, A., and Dezayes, C. (2006). Deep-seated geology of the granite intrusions at the Soultz EGS site based on data from 5km-deep boreholes. *Geothermics*, 35(5-6):484–506. doi:[10.1016/j.geothermics.2006.03.003](https://doi.org/10.1016/j.geothermics.2006.03.003).
- Horton, C. W. and Rogers, F. T. (1945). Convection Currents in a Porous Medium. *Journal of Applied Physics*, 16(6):367–370. doi:[10.1063/1.1707601](https://doi.org/10.1063/1.1707601).
- Hughes, J. D., Langevin, C. D., and Banta, E. R. (2017). Documentation for the MODFLOW 6 framework. doi:[10.3133/tm6a57](https://doi.org/10.3133/tm6a57).
- Huppert, H. E. and Turner, J. S. (1981). Double-diffusive convection. *Journal of Fluid Mechanics*, 106(-1):299–329. doi:[10.1017/s0022112081001614](https://doi.org/10.1017/s0022112081001614).
- IAPWS (2007). R7-97: Revised Release on the IAPWS Industrial Formulation 1997 for the Thermodynamic Properties of Water and Steam. *International Association for the Properties of Water and Steam (IAPWS)*, pages 1–48.
- Illies, J. H. (1972). The Rhine graben rift system-plate tectonics and transform faulting. *Geophysical Surveys*, 1(1):27–60. doi:[10.1007/bf01449550](https://doi.org/10.1007/bf01449550).
- Illies, J. H. and Greiner, G. (1978). Rhinegraben and the Alpine system. *Geological Society of America Bulletin*, 89(5):770–782. doi:[10.1130/0016-7606\(1978\)89<770:ratas>2.0.co;2](https://doi.org/10.1130/0016-7606(1978)89<770:ratas>2.0.co;2).
- Imperial College Consortium On Pore-Scale Modelling (2014). LV60A sandpack. doi:[10.6084/m9.figshare.1153795](https://doi.org/10.6084/m9.figshare.1153795).

REFERENCES

- IPGT (2012). Reservoir Modeling Working Group: Recommendations for Research and Development (white paper). *International Partnership for Geothermal Technology*.
- Jeffreys, H. (1926). LXXVI. The stability of a layer of fluid heated below. *The London, Edinburgh, and Dublin Philosophical Magazine and Journal of Science*, 2(10):833–844. doi:[10.1080/14786442608564114](https://doi.org/10.1080/14786442608564114).
- Jung, R., Willis-Richard, J., Nicholls, J., Bertozzi, A., and Heinemann, B. (1995). Evaluation of hydraulic tests at Soultz-sous-Forêts, European HDR Site. In *Proceedings of the world geothermal congress*, volume 4, pages 2671–2676. doi:[10.1016/j.geothermics.2006.11.007](https://doi.org/10.1016/j.geothermics.2006.11.007).
- Keller, H. B. (1979). Constructive methods for bifurcation and nonlinear eigenvalue problems. In *Lecture Notes in Mathematics*, pages 241–251. Springer Berlin Heidelberg. doi:[10.1007/bfb0063623](https://doi.org/10.1007/bfb0063623).
- Kipp, K. L., Hsieh, P. A., and Charlton, S. R. (2008). Guide to the revised ground-water flow and heat transport simulator: HYDROTHERM-Version 3. Technical report, U.S. Geological Survey Techniques and Methods. doi:[10.1111/j.1745-6584.2012.00993.x](https://doi.org/10.1111/j.1745-6584.2012.00993.x).
- Kohl, T., Bächler, D., and Rybach, L. (2000). Steps towards a comprehensive thermo-hydraulic analysis of the HDR test site Soultz-sous-Forêts. In *Proceedings World Geothermal Congress*, pages 2671–2676. Kyushu-Tohoku Japan. doi:[10.1016/s0375-6505\(03\)00069-5](https://doi.org/10.1016/s0375-6505(03)00069-5).
- Kohl, T., Evans, K. F., Hopkirk, R. J., Jung, R., and Rybach, L. (1995a). Modelling of turbulent flow transients within Hot Dry Rock fracture systems: Preliminary results. *Proc. World Geothermal Cong.*
- Kohl, T., Evans, K., Hopkirk, R., and Rybach, L. (1995b). Coupled hydraulic, thermal and mechanical considerations for the simulation of hot dry rock reservoirs. *Geothermics*, 24(3):345–359. doi:[10.1016/0375-6505\(95\)00013-g](https://doi.org/10.1016/0375-6505(95)00013-g).
- Kolditz, O., Böttcher, N., and Görke, U.-J. (2012). OpenGeoSys: an open-source initiative for numerical simulation of thermo-hydro-mechanical/chemical (THM/C) processes in porous media. In *Thermo-Hydro-Mechanical-Chemical Processes in Porous Media*, pages 9–59. Springer Berlin Heidelberg. doi:[10.1007/978-3-642-27177-9_2](https://doi.org/10.1007/978-3-642-27177-9_2).
- Korkine, A. (1869). Sur les intégrales des équations du mouvement d'un point matériel. *Mathematische Annalen*, 2(1):13–40. doi:[10.1007/bf01443913](https://doi.org/10.1007/bf01443913).
- Lachenbruch, A. H. and Sass, J. H. (1980). Heat flow and energetics of the San Andreas Fault Zone. *Journal of Geophysical Research: Solid Earth*, 85(B11):6185–6222. doi:[10.1029/jb085ib11p06185](https://doi.org/10.1029/jb085ib11p06185).
- Lampe, C. and Person, M. (2000). Episodic hydrothermal fluid flow in the Upper Rhinegraben (Germany). *Journal of Geochemical Exploration*, 69-70:37–40. doi:[10.1016/s0375-6742\(00\)00049-2](https://doi.org/10.1016/s0375-6742(00)00049-2).
- Lapwood, E. R. (1948). Convection of a fluid in a porous medium. *Mathematical Proceedings of the Cambridge Philosophical Society*, 44(4):508–521. doi:[10.1017/s030500410002452x](https://doi.org/10.1017/s030500410002452x).
- Larroque, J. and Laurent, P. (1988). Evolution of the stress field pattern in the south of the Rhine Graben from the Eocene to the present. *Tectonophysics*, 148(1-2):41–58. doi:[10.1016/0040-1951\(88\)90159-x](https://doi.org/10.1016/0040-1951(88)90159-x).

REFERENCES

- Ledéserf, B., Berger, G., Meunier, A., Genter, A., and Bouchet, A. (1999). Diagenetic-type reactions related to hydrothermal alteration in the Soultz-sous-Forêts granite, France. *European Journal of Mineralogy*, 11(4):731–742. doi:[10.1127/ejm/11/4/0731](https://doi.org/10.1127/ejm/11/4/0731).
- Ledéserf, B., Dubois, J., Velde, B., Meunier, A., Genter, A., and Badri, A. (1993). Geometrical and fractal analysis of a three-dimensional hydrothermal vein network in a fractured granite. *Journal of Volcanology and Geothermal Research*, 56(3):267–280. doi:[10.1016/0377-0273\(93\)90020-r](https://doi.org/10.1016/0377-0273(93)90020-r).
- Ledéserf, B., Hebert, R., Genter, A., Bartier, D., Clauer, N., and Grall, C. (2010). Fractures, hydrothermal alterations and permeability in the Soultz Enhanced Geothermal System. *Comptes Rendus Geoscience*, 342(7-8):607–615. doi:[10.1016/j.crte.2009.09.011](https://doi.org/10.1016/j.crte.2009.09.011).
- Leloup, P. H., Ricard, Y., Battaglia, J., and Lacassin, R. (1999). Shear heating in continental strike-slip shear zones: model and field examples. *Geophysical Journal International*, 136(1):19–40. doi:[10.1046/j.1365-246x.1999.00683.x](https://doi.org/10.1046/j.1365-246x.1999.00683.x).
- Magenet, V., Fond, C., Genter, A., and Schmittbuhl, J. (2014). Two-dimensional THM modelling of the large scale natural hydrothermal circulation at Soultz-sous-Forêts. *Geothermal Energy*, 2(1). doi:[10.1186/s40517-014-0017-x](https://doi.org/10.1186/s40517-014-0017-x).
- McDonald, J. M. and Harbaugh, A. W. (1988). MODFLOW, a modular 3D finite difference ground-water flow model. *US Geological Survey. Open File Report*, pages 83–875. doi:[10.1111/j.1745-6584.2003.tb02591.x](https://doi.org/10.1111/j.1745-6584.2003.tb02591.x).
- Mitchell, T., Ben-Zion, Y., and Shimamoto, T. (2011). Pulverized fault rocks and damage asymmetry along the Arima-Takatsuki Tectonic Line, Japan. *Earth and Planetary Science Letters*, 308(3-4):284–297. doi:[10.1016/j.epsl.2011.04.023](https://doi.org/10.1016/j.epsl.2011.04.023).
- Mohsen, A. (2014). A simple solution of the Bratu problem. *Computers & Mathematics with Applications*, 67(1):26–33. doi:[10.1016/j.camwa.2013.10.003](https://doi.org/10.1016/j.camwa.2013.10.003).
- Morrison, H. L. (1947). Preliminary Measurements Relative to the Onset of Thermal Convection Currents in Unconsolidated Sands. *Journal of Applied Physics*, 18(9):849–850. doi:[10.1063/1.1697857](https://doi.org/10.1063/1.1697857).
- Nield, D. A. (1968). Onset of Thermohaline Convection in a Porous Medium. *Water Resources Research*, 4(3):553–560. doi:[10.1029/wr004i003p00553](https://doi.org/10.1029/wr004i003p00553).
- Nield, D. A. and Bejan, A. (2013). *Convection in Porous Media*. Springer New York, fourth edition edition. doi:[10.1007/978-1-4614-5541-7](https://doi.org/10.1007/978-1-4614-5541-7). ISBN: 9781461455417.
- Nimmo, F., Spencer, J. R., Pappalardo, R. T., and Mullen, M. E. (2007). Shear heating as the origin of the plumes and heat flux on Enceladus. *Nature*, 447(7142):289–291. doi:[10.1038/nature05783](https://doi.org/10.1038/nature05783).
- Paesold, M., Bassom, A., Regenauer-Lieb, K., and Veveakis, M. (2016). Conditions for the localisation of plastic deformation in temperature sensitive viscoplastic materials. *Journal of Mechanics of Materials and Structures*, 11(2):113–136. doi:[10.2140/jomms.2016.11.113](https://doi.org/10.2140/jomms.2016.11.113).
- Plenefisch, T. and Bonjer, K.-P. (1997). The stress field in the Rhine Graben area inferred from earthquake focal mechanisms and estimation of frictional parameters. *Tectonophysics*, 275(1-3):71–97. doi:[10.1016/s0040-1951\(97\)00016-4](https://doi.org/10.1016/s0040-1951(97)00016-4).

REFERENCES

- Podgorney, R., Huang, H., and Gaston, D. (2010). Massively parallel fully coupled implicit modeling of coupled thermal-hydrological-mechanical processes for enhanced geothermal system reservoirs. Technical Report (No. INL/CON-10-17691), Idaho National Laboratory (INL). doi:[10.11128/sne.23.tn.10175](https://doi.org/10.11128/sne.23.tn.10175).
- Podgorney, R. K., Huang, H., Lu, C., Gaston, D., Permann, C., Guo, L., and Andrs, D. (2011). FALCON: A Physics-Based, Massively Parallel, Fully-Coupled, Finite Element Model for Simultaneously Solving Multiphase Fluid Flow, Heat Transport, and Rock Deformation for Geothermal Reservoir Simulation, Idaho National Laboratory Report INL. *Idaho National Laboratory Report INL/EXT-11-23351*. doi:[10.1016/j.advwatres.2012.10.010](https://doi.org/10.1016/j.advwatres.2012.10.010).
- Poulet, T., Paesold, M., and Veveakis, M. (2016). Multi-Physics Modelling of Fault Mechanics Using REDBACK: A Parallel Open-Source Simulator for Tightly Coupled Problems. *Rock Mechanics and Rock Engineering*, 50(3):733–749. doi:[10.1007/s00603-016-0927-y](https://doi.org/10.1007/s00603-016-0927-y).
- Poulet, T. and Veveakis, M. (2016). A viscoplastic approach for pore collapse in saturated soft rocks using REDBACK: An open-source parallel simulator for Rock mEchanics with Dissipative feedBACKs. *Computers and Geotechnics*, 74:211–221. doi:[10.1016/j.compgeo.2015.12.015](https://doi.org/10.1016/j.compgeo.2015.12.015).
- Pribnow, D. and Clauser, C. (2000). Heat and fluid flow at the Soultz hot dry rock system in the Rhine Graben. In *World Geothermal Congress, Kyushu-Tohoku, Japan*, pages 3835–3840.
- Pribnow, D. and Schellschmidt, R. (2000). Thermal tracking of upper crustal fluid flow in the Rhine graben. *Geophys. Res. Lett.*, 27(13):1957–1960. doi:[10.1029/2000g1008494](https://doi.org/10.1029/2000g1008494).
- Pruess, K. (1991). TOUGH2: A general-purpose numerical simulator for multiphase fluid and heat flow. Technical report, Ernest Orlando Lawrence Berkeley National Laboratory, Berkeley, CA (US). doi:[10.2172/5212064](https://doi.org/10.2172/5212064).
- Pruess, K., Oldenburg, C., and Moridis, G. (1999). TOUGH2 User's Guide Version 2. Technical report, Ernest Orlando Lawrence Berkeley National Laboratory, Berkeley, CA (US). doi:[10.2172/751729](https://doi.org/10.2172/751729).
- Rayleigh, L. (1916). LIX. On convection currents in a horizontal layer of fluid, when the higher temperature is on the under side. *The London, Edinburgh, and Dublin Philosophical Magazine and Journal of Science*, 32(192):529–546. doi:[10.1080/14786441608635602](https://doi.org/10.1080/14786441608635602).
- Regenauer-Lieb, K. and Yuen, D. (2003). Modeling shear zones in geological and planetary sciences: solid- and fluid-thermal–mechanical approaches. *Earth-Science Reviews*, 63(3-4):295–349. doi:[10.1016/s0012-8252\(03\)00038-2](https://doi.org/10.1016/s0012-8252(03)00038-2).
- Regenauer-Lieb, K. and Yuen, D. A. (1998). Rapid conversion of elastic energy into plastic shear heating during incipient necking of the lithosphere. *Geophysical Research Letters*, 25(14):2737–2740. doi:[10.1029/98g102056](https://doi.org/10.1029/98g102056).
- Reid, L. B., Corbel, S., Poulet, T., Ricard, L. P., Schilling, O., Sheldon, H. A., and Wellmann, J. F. (2012). Hydrothermal Modelling in the Perth Basin, Final Report of Project 3, Perth Basin Assessments Program. *WAGCoE Report EP121504*, page 202. doi:[10.1007/s10040-012-0945-0](https://doi.org/10.1007/s10040-012-0945-0).

REFERENCES

- Ricciardi, K. L., Pinder, G. F., and Belitz, K. (2005). Comparison of the lognormal and beta distribution functions to describe the uncertainty in permeability. *Journal of Hydrology*, 313(3-4):248–256. doi:[10.1016/j.jhydrol.2005.03.007](https://doi.org/10.1016/j.jhydrol.2005.03.007).
- Rice, J. R. (2006). Heating and weakening of faults during earthquake slip. *Journal of Geophysical Research: Solid Earth*, 111(B5). doi:[10.1029/2005jb004006](https://doi.org/10.1029/2005jb004006).
- Rousset, D., Bayer, R., Guillon, D., and Edel, J. B. (1993). Structure of the southern Rhine Graben from gravity and reflection seismic data (ecors-dekorp program). *Tectonophysics*, 221(2):135–153. doi:[10.1016/0040-1951\(93\)90329-i](https://doi.org/10.1016/0040-1951(93)90329-i).
- Sausse, J. (2002). Hydromechanical properties and alteration of natural fracture surfaces in the Soultz granite (Bas-Rhin, France). *Tectonophysics*, 348(1-3):169–185. doi:[10.1016/s0040-1951\(01\)00255-4](https://doi.org/10.1016/s0040-1951(01)00255-4).
- Sausse, J., Dezayes, C., Dorbath, L., Genter, A., and Place, J. (2010). 3D model of fracture zones at Soultz-sous-Forêts based on geological data, image logs, induced microseismicity and vertical seismic profiles. *Comptes Rendus Geoscience*, 342(7-8):531–545. doi:[10.1016/j.crte.2010.01.011](https://doi.org/10.1016/j.crte.2010.01.011).
- Sausse, J., Fourar, M., and Genter, A. (2006). Permeability and alteration within the Soultz granite inferred from geophysical and flow log analysis. *Geothermics*, 35(5-6):544–560. doi:[10.1016/j.geothermics.2006.07.003](https://doi.org/10.1016/j.geothermics.2006.07.003).
- Schatz, M. F., VanHook, S. J., McCormick, W. D., Swift, J. B., and Swinney, H. L. (1995). Onset of Surface-Tension-Driven Bénard Convection. *Phys. Rev. Lett.*, 75(10):1938–1941. doi:[10.1103/physrevlett.75.1938](https://doi.org/10.1103/physrevlett.75.1938).
- Schellschmidt, R. and Clauser, C. (1996). The thermal regime of the Upper Rhine Graben and the anomaly at Soultz. *Zeitschrift für Angewandte Geologie*, 42(1):40–44.
- Schilling, O., Sheldon, H. A., Reid, L. B., and Corbel, S. (2013). Hydrothermal models of the Perth metropolitan area, Western Australia: implications for geothermal energy. *Hydrogeology Journal*, 21(3):605–621. doi:[10.1007/s10040-012-0945-0](https://doi.org/10.1007/s10040-012-0945-0).
- Schleicher, A. M., Warr, L. N., Kober, B., Laverret, E., and Clauer, N. (2006). Episodic mineralization of hydrothermal illite in the Soultz-sous-Forêts granite (Upper Rhine Graben, France). *Contributions to Mineralogy and Petrology*, 152(3):349–364. doi:[10.1007/s00410-006-0110-7](https://doi.org/10.1007/s00410-006-0110-7).
- Scholz, C. H. (1980). Shear heating and the state of stress on faults. *Journal of Geophysical Research: Solid Earth*, 85(B11):6174–6184. doi:[10.1029/jb085ib11p06174](https://doi.org/10.1029/jb085ib11p06174).
- Scholz, C. H. (1998). Earthquakes and friction laws. *Nature*, 391(6662):37–42. doi:[10.1038/34097](https://doi.org/10.1038/34097).
- Sibson, R. H. (1982). Fault zone models, heat flow, and the depth distribution of earthquakes in the continental crust of the United States. *Bulletin of the Seismological Society of America*, 72(1):151–163.
- Stommel, H., Arons, A. B., and Blanchard, D. (1956). An oceanographical curiosity: the perpetual salt fountain. *Deep Sea Research (1953)*, 3(2):152–153. doi:[10.1016/0146-6313\(56\)90095-8](https://doi.org/10.1016/0146-6313(56)90095-8).
- Tsang, C.-F., Stephansson, O., Jing, L., and Kautsky, F. (2008). DECOVALEX Project: from 1992 to 2007. *Environmental Geology*, 57(6):1221–1237. doi:[10.1007/s00254-008-1625-1](https://doi.org/10.1007/s00254-008-1625-1).

REFERENCES

- Tung, R., Poulet, T., Alevizos, S., Veveakis, E., and Regenauer-Lieb, K. (2017). Shear heating in creeping faults changes the onset of convection . *Geophysical Journal International*, 211(1):270–283. doi:[10.1093/gji/ggx295](https://doi.org/10.1093/gji/ggx295).
- van Dyke, M. and White, F. M. (1982). An Album of Fluid Motion. *Journal of Fluids Engineering*, 104(4):542. doi:[10.1115/1.3241909](https://doi.org/10.1115/1.3241909).
- Veveakis, E., Alevizos, S., and Vardoulakis, I. (2010). Chemical reaction capping of thermal instabilities during shear of frictional faults. *Journal of the Mechanics and Physics of Solids*, 58(9):1175–1194. doi:[10.1016/j.jmps.2010.06.010](https://doi.org/10.1016/j.jmps.2010.06.010).
- Vidal, J., Genter, A., and Chopin, F. (2017). Permeable fracture zones in the hard rocks of the geothermal reservoir at Rittershoffen, France. *Journal of Geophysical Research: Solid Earth*. doi:[10.1002/2017jb014331](https://doi.org/10.1002/2017jb014331).
- Vidal, J., Genter, A., and Schmittbuhl, J. (2015). How do permeable fractures in the Triassic sediments of Northern Alsace characterize the top of hydrothermal convective cells? Evidence from Soultz geothermal boreholes (France). *Geothermal Energy*, 3(1). doi:[10.1186/s40517-015-0026-4](https://doi.org/10.1186/s40517-015-0026-4).
- Xia, Y., Podgorney, R., and Huang, H. (2016). Assessment of a Hybrid Continuous/Discontinuous Galerkin Finite Element Code for Geothermal Reservoir Simulations. *Rock Mechanics and Rock Engineering*, 50(3):719–732. doi:[10.1007/s00603-016-0951-y](https://doi.org/10.1007/s00603-016-0951-y).
- Yuen, D. A., Fleitout, L., Schubert, G., and Froidevaux, C. (1978). Shear deformation zones along major transform faults and subducting slabs. *Geophysical Journal International*, 54(1):93–119. doi:[10.1111/j.1365-246x.1978.tb06758.x](https://doi.org/10.1111/j.1365-246x.1978.tb06758.x).
- Yuen, D. A., Saari, M. R., and Schubert, G. (1986). Explosive Growth of Shear-Heating Instabilities in the Down-Slope Creep of Ice Sheets. *Journal of Glaciology*, 32(112):314–320. doi:[10.1017/s0022143000011977](https://doi.org/10.1017/s0022143000011977).
- Ziegler, P. A. (1992). European Cenozoic rift system. *Tectonophysics*, 208(1-3):91–111. doi:[10.1016/0040-1951\(92\)90338-7](https://doi.org/10.1016/0040-1951(92)90338-7).
- Zyvoloski, G., Dash, Z., and Kelkar, S. (1988). FEHM: finite element heat and mass transfer code. Technical report, Los Alamos National Laboratory (LANL). doi:[10.2172/5495517](https://doi.org/10.2172/5495517).
- Zyvoloski, G. A., Robinson, B. A., Dash, Z. V., and Trease, L. L. (1997). User's Manual for the FEHM Application-A Finite-Element Heat- and Mass-Transfer Code. Technical report, Los Alamos National Laboratory (LANL). doi:[10.2172/14902](https://doi.org/10.2172/14902).

Appendix A

Copyright Consent

This appendix contains proof to reproduce published content (including figures) in this dissertation.

RE: Permission to reproduce article in a PhD thesis

JOURNALS PERMISSIONS <Journals.Permissions@oup.com>

Thu 5/07/2018 5:38 PM

Inbox

To: Rebecca Tung <rebecca.tung@postgrad.curtin.edu.au>;

Self-Archiving Policy P

Dear Rebecca Tung,

RE. R. Tung et al. Shear heating in creeping faults changes the onset of convection. *Geophysical Journal International* (2017) 211 (1): 270-283

Thank you for your email requesting permission to reuse all or part of your article in a thesis/dissertation.

As part of your copyright agreement with Oxford University Press you have retained the right, after publication, to use all or part of the article and abstract, in the preparation of derivative works, extension of the article into a booklength work, in a thesis/dissertation, or in another works collection, provided that a full acknowledgement is made to the original publication in the journal. As a result, you should not require direct permission from Oxford University Press to reuse your article.

Authors may upload a PDF of the **accepted manuscript** to institutional and/or centrally organized repositories and/or in free public servers, upon acceptance for publication in the journal. Authors may upload the **version of record** to institutional and/or centrally organized repositories and/or in free public servers, upon publication in the journal.

Please Note: Inclusion under a Creative Commons License or any other Open-Access License allowing onward reuse is prohibited.

For full details of our publication and rights policy, including **credit-lines**, please see the attached link to our website:

https://academic.oup.com/journals/pages/access_purchase/rights_and_permissions/self_archiving_policy_p

If you have any other queries, please feel free to contact us.

Kind regards,
Katie

Katie Randall | Permissions Assistant | Rights Department
Academic and Journals Divisions | Global Business Development
Oxford University Press | Great Clarendon Street | Oxford | OX2 6DP



From: Rebecca Tung [mailto:rebecca.tung@postgrad.curtin.edu.au]

Sent: 05 July 2018 05:12

To: JOURNALS PERMISSIONS

Subject: Permission to reproduce article in a PhD thesis

Dear Publisher,

It is my understanding that Oxford Journals are the copyright holder for the following material:

**Tung, R., T. Poulet, S. Alevizos, E. Veveakis, and K. Regenauer-Lieb. "Shear heating in creeping faults changes the onset of convection." *Geophysical Journal International* 211, no. 1 (2017): 270-283.
DOI: 10.1093/gji/ggx295**

I would like to reproduce this work (figures, captions, and text) in a doctoral thesis which I am currently undertaking at Curtin University in Perth, Western Australia. I intend to integrate the article into a thesis chapter, so the formatting will be suited to my thesis layout. The current title of my thesis is "**On the onset of hydrothermal convection in porous media in the presence of creeping faults: numerical stability analysis and geological applications**". I am carrying out this research in my own right and have no association with any commercial organisation or sponsor.

Once completed, the thesis will be made available in online form via Curtin University's Institutional Repository espace (<http://espace.curtin.edu.au>). The material will be provided strictly for educational purposes and on a non-commercial basis.

I would be most grateful for your consent to the copying and communication of the work as proposed. Full acknowledgement of the ownership of the copyright and the source of the material will be provided with the material. I would be willing to use a specific form of acknowledgement that you may require to communicate any conditions relating to its use.

If you are not the copyright owner of the material in question, I would be grateful for any information you can provide as to who is likely to hold the copyright. I look forward to hearing from you and thank you in advance for your consideration of my request.

Yours sincerely,
Rebecca

Rebecca Tung

BSc (Geophysics) (Honours)

PhD Candidate

WA School of Mines: Minerals, Energy and Chemical Engineering (WASM-MECE)

Department of Exploration Geophysics

Curtin University

Tel | +61 8 9266 3408

Fax | +61 8 9266 3407

Email | rebecca.tung@postgrad.curtin.edu.au

Web | <http://geophysics.curtin.edu.au>



Curtin University is a trademark of Curtin University of Technology.

CRICOS Provider Code 00301J (WA), 02637B (NSW)

**JOHN WILEY AND SONS LICENSE
TERMS AND CONDITIONS**

Jun 04, 2019

This Agreement between Miss. Rebecca Tung ("You") and John Wiley and Sons ("John Wiley and Sons") consists of your license details and the terms and conditions provided by John Wiley and Sons and Copyright Clearance Center.

License Number	4601910733120
License date	Jun 04, 2019
Licensed Content Publisher	John Wiley and Sons
Licensed Content Publication	Wiley Books
Licensed Content Title	Bénard Convection
Licensed Content Author	E. L. Koschmieder
Licensed Content Date	Mar 14, 2007
Licensed Content Pages	36
Type of use	Dissertation/Thesis
Requestor type	University/Academic
Format	Print and electronic
Portion	Figure/table
Number of figures/tables	1
Original Wiley figure/table number(s)	Figure 4
Will you be translating?	No
Title of your thesis / dissertation	On the Onset of Hydrothermal Convection in Porous Media in the Presence of Creeping Faults: Numerical Stability Analysis and Geological Applications
Expected completion date	Jun 2019
Expected size (number of pages)	150
Requestor Location	Miss. Rebecca Tung Department of Exploration Geophysics ARRC 26 Dick Perry Ave Kensington, WA 6151 Australia Attn: Miss. Rebecca Tung
Publisher Tax ID	EU826007151
Total	0.00 AUD
Terms and Conditions	

TERMS AND CONDITIONS

This copyrighted material is owned by or exclusively licensed to John Wiley & Sons, Inc. or one of its group companies (each a "Wiley Company") or handled on behalf of a society with which a Wiley Company has exclusive publishing rights in relation to a particular work (collectively "WILEY"). By clicking "accept" in connection with completing this licensing transaction, you agree that the following terms and conditions apply to this transaction (along with the billing and payment terms and conditions established by the Copyright Clearance Center Inc., ("CCC's Billing and Payment terms and conditions"), at the time that you opened your RightsLink account (these are available at any time at <http://myaccount.copyright.com>).

Terms and Conditions

- The materials you have requested permission to reproduce or reuse (the "Wiley Materials") are protected by copyright.
- You are hereby granted a personal, non-exclusive, non-sub licensable (on a stand-alone basis), non-transferable, worldwide, limited license to reproduce the Wiley Materials for the purpose specified in the licensing process. This license, **and any CONTENT (PDF or image file) purchased as part of your order**, is for a one-time use only and limited to any maximum distribution number specified in the license. The first instance of republication or reuse granted by this license must be completed within two years of the date of the grant of this license (although copies prepared before the end date may be distributed thereafter). The Wiley Materials shall not be used in any other manner or for any other purpose, beyond what is granted in the license. Permission is granted subject to an appropriate acknowledgement given to the author, title of the material/book/journal and the publisher. You shall also duplicate the copyright notice that appears in the Wiley publication in your use of the Wiley Material. Permission is also granted on the understanding that nowhere in the text is a previously published source acknowledged for all or part of this Wiley Material. Any third party content is expressly excluded from this permission.
- With respect to the Wiley Materials, all rights are reserved. Except as expressly granted by the terms of the license, no part of the Wiley Materials may be copied, modified, adapted (except for minor reformatting required by the new Publication), translated, reproduced, transferred or distributed, in any form or by any means, and no derivative works may be made based on the Wiley Materials without the prior permission of the respective copyright owner. **For STM Signatory Publishers clearing permission under the terms of the [STM Permissions Guidelines](#) only, the terms of the license are extended to include subsequent editions and for editions in other languages, provided such editions are for the work as a whole in situ and does not involve the separate exploitation of the permitted figures or extracts,** You may not alter, remove or suppress in any manner any copyright, trademark or other notices displayed by the Wiley Materials. You may not license, rent, sell, loan, lease, pledge, offer as security, transfer or assign the Wiley Materials on a stand-alone basis, or any of the rights granted to you hereunder to any other person.
- The Wiley Materials and all of the intellectual property rights therein shall at all times remain the exclusive property of John Wiley & Sons Inc, the Wiley Companies, or their respective licensors, and your interest therein is only that of having possession of and the right to reproduce the Wiley Materials pursuant to Section 2 herein during the continuance of this Agreement. You agree that you own no right, title or interest in or to the Wiley Materials or any of the intellectual property rights therein. You shall have no rights hereunder other than the license as provided for above in Section 2. No right, license or interest to any trademark, trade name, service mark or other branding ("Marks") of WILEY or its licensors is granted hereunder, and you agree that you shall not assert any such right, license or interest with respect thereto
- NEITHER WILEY NOR ITS LICENSORS MAKES ANY WARRANTY OR REPRESENTATION OF ANY KIND TO YOU OR ANY THIRD PARTY, EXPRESS, IMPLIED OR STATUTORY, WITH RESPECT TO THE MATERIALS OR THE ACCURACY OF ANY INFORMATION CONTAINED IN THE MATERIALS, INCLUDING, WITHOUT LIMITATION, ANY IMPLIED WARRANTY OF MERCHANTABILITY, ACCURACY, SATISFACTORY QUALITY, FITNESS FOR A PARTICULAR PURPOSE, USABILITY, INTEGRATION OR NON-INFRINGEMENT AND ALL SUCH WARRANTIES ARE HEREBY EXCLUDED BY WILEY AND ITS LICENSORS AND WAIVED

BY YOU.

- WILEY shall have the right to terminate this Agreement immediately upon breach of this Agreement by you.
- You shall indemnify, defend and hold harmless WILEY, its Licensors and their respective directors, officers, agents and employees, from and against any actual or threatened claims, demands, causes of action or proceedings arising from any breach of this Agreement by you.
- IN NO EVENT SHALL WILEY OR ITS LICENSORS BE LIABLE TO YOU OR ANY OTHER PARTY OR ANY OTHER PERSON OR ENTITY FOR ANY SPECIAL, CONSEQUENTIAL, INCIDENTAL, INDIRECT, EXEMPLARY OR PUNITIVE DAMAGES, HOWEVER CAUSED, ARISING OUT OF OR IN CONNECTION WITH THE DOWNLOADING, PROVISIONING, VIEWING OR USE OF THE MATERIALS REGARDLESS OF THE FORM OF ACTION, WHETHER FOR BREACH OF CONTRACT, BREACH OF WARRANTY, TORT, NEGLIGENCE, INFRINGEMENT OR OTHERWISE (INCLUDING, WITHOUT LIMITATION, DAMAGES BASED ON LOSS OF PROFITS, DATA, FILES, USE, BUSINESS OPPORTUNITY OR CLAIMS OF THIRD PARTIES), AND WHETHER OR NOT THE PARTY HAS BEEN ADVISED OF THE POSSIBILITY OF SUCH DAMAGES. THIS LIMITATION SHALL APPLY NOTWITHSTANDING ANY FAILURE OF ESSENTIAL PURPOSE OF ANY LIMITED REMEDY PROVIDED HEREIN.
- Should any provision of this Agreement be held by a court of competent jurisdiction to be illegal, invalid, or unenforceable, that provision shall be deemed amended to achieve as nearly as possible the same economic effect as the original provision, and the legality, validity and enforceability of the remaining provisions of this Agreement shall not be affected or impaired thereby.
- The failure of either party to enforce any term or condition of this Agreement shall not constitute a waiver of either party's right to enforce each and every term and condition of this Agreement. No breach under this agreement shall be deemed waived or excused by either party unless such waiver or consent is in writing signed by the party granting such waiver or consent. The waiver by or consent of a party to a breach of any provision of this Agreement shall not operate or be construed as a waiver of or consent to any other or subsequent breach by such other party.
- This Agreement may not be assigned (including by operation of law or otherwise) by you without WILEY's prior written consent.
- Any fee required for this permission shall be non-refundable after thirty (30) days from receipt by the CCC.
- These terms and conditions together with CCC's Billing and Payment terms and conditions (which are incorporated herein) form the entire agreement between you and WILEY concerning this licensing transaction and (in the absence of fraud) supersedes all prior agreements and representations of the parties, oral or written. This Agreement may not be amended except in writing signed by both parties. This Agreement shall be binding upon and inure to the benefit of the parties' successors, legal representatives, and authorized assigns.
- In the event of any conflict between your obligations established by these terms and conditions and those established by CCC's Billing and Payment terms and conditions, these terms and conditions shall prevail.

-
- WILEY expressly reserves all rights not specifically granted in the combination of (i) the license details provided by you and accepted in the course of this licensing transaction, (ii) these terms and conditions and (iii) CCC's Billing and Payment terms and conditions.
 - This Agreement will be void if the Type of Use, Format, Circulation, or Requestor Type was misrepresented during the licensing process.
 - This Agreement shall be governed by and construed in accordance with the laws of the State of New York, USA, without regards to such state's conflict of law rules. Any legal action, suit or proceeding arising out of or relating to these Terms and Conditions or the breach thereof shall be instituted in a court of competent jurisdiction in New York County in the State of New York in the United States of America and each party hereby consents and submits to the personal jurisdiction of such court, waives any objection to venue in such court and consents to service of process by registered or certified mail, return receipt requested, at the last known address of such party.

WILEY OPEN ACCESS TERMS AND CONDITIONS

Wiley Publishes Open Access Articles in fully Open Access Journals and in Subscription journals offering Online Open. Although most of the fully Open Access journals publish open access articles under the terms of the Creative Commons Attribution (CC BY) License only, the subscription journals and a few of the Open Access Journals offer a choice of Creative Commons Licenses. The license type is clearly identified on the article.

The Creative Commons Attribution License

The [Creative Commons Attribution License \(CC-BY\)](#) allows users to copy, distribute and transmit an article, adapt the article and make commercial use of the article. The CC-BY license permits commercial and non-

Creative Commons Attribution Non-Commercial License

The [Creative Commons Attribution Non-Commercial \(CC-BY-NC\) License](#) permits use, distribution and reproduction in any medium, provided the original work is properly cited and is not used for commercial purposes.(see below)

Creative Commons Attribution-Non-Commercial-NoDerivs License

The [Creative Commons Attribution Non-Commercial-NoDerivs License \(CC-BY-NC-ND\)](#) permits use, distribution and reproduction in any medium, provided the original work is properly cited, is not used for commercial purposes and no modifications or adaptations are made. (see below)

Use by commercial "for-profit" organizations

Use of Wiley Open Access articles for commercial, promotional, or marketing purposes requires further explicit permission from Wiley and will be subject to a fee.

Further details can be found on Wiley Online Library
<http://olabout.wiley.com/WileyCDA/Section/id-410895.html>

Other Terms and Conditions:

v1.10 Last updated September 2015

Questions? customercare@copyright.com or +1-855-239-3415 (toll free in the US) or +1-978-646-2777.

This page is available in the following languages:



Creative Commons License Deed

Attribution 4.0 International (CC BY 4.0)



This is a human-readable summary of (and not a substitute for) the [license](#).

You are free to:

Share — copy and redistribute the material in any medium or format

Adapt — remix, transform, and build upon the material

for any purpose, even commercially.

The licensor cannot revoke these freedoms as long as you follow the license terms.

Under the following terms:

Attribution — You must give appropriate credit, provide a link to the license, and indicate if changes were made. You may do so in any reasonable manner, but not in any way that suggests the licensor endorses you or your use.

No additional restrictions — You may not apply legal terms or technological measures that legally restrict others from doing anything the license permits.

Notices:

You do not have to comply with the license for elements of the material in the public domain or where your use is permitted by an applicable exception or limitation.

No warranties are given. The license may not give you all of the permissions necessary for your intended use. For example, other rights such as publicity, privacy, or moral rights may limit how you use the material.

Help us build a vibrant, collaborative global commons



This page is available in the following languages:



Creative Commons Legal Code

Attribution 4.0 International

Official translations of this license are available [in other languages](#).

Creative Commons Corporation (“Creative Commons”) is not a law firm and does not provide legal services or legal advice. Distribution of Creative Commons public licenses does not create a lawyer-client or other relationship. Creative Commons makes its licenses and related information available on an “as-is” basis. Creative Commons gives no warranties regarding its licenses, any material licensed under their terms and conditions, or any related information. Creative Commons disclaims all liability for damages resulting from their use to the fullest extent possible.

Using Creative Commons Public Licenses

Creative Commons public licenses provide a standard set of terms and conditions that creators and other rights holders may use to share original works of authorship and other material subject to copyright and certain other rights specified in the public license below. The following considerations are for informational purposes only, are not exhaustive, and do not form part of our licenses.

Considerations for licensors: Our public licenses are intended for use by those authorized to give the public permission to use material in ways otherwise restricted by copyright and certain other rights. Our licenses are irrevocable. Licensors should read and understand the terms and conditions of the license they choose before applying it. Licensors should also secure all rights necessary before applying our licenses so that the public can reuse the material as expected. Licensors should clearly mark any material not subject to the license. This includes other CC-licensed material, or material used under an exception or limitation to copyright. [More considerations for licensors.](#) ▼

Considerations for the public: By using one of our public licenses, a licensor grants the public permission to use the licensed material under specified terms and conditions. If the licensor’s permission is not necessary for any reason—for example, because of any applicable exception or limitation to copyright—then that use is not regulated by the license. Our licenses grant only permissions under copyright and certain other rights that a licensor has authority to grant. Use of the licensed material may still be restricted for other reasons, including because others have copyright or other rights in the material. A licensor may make special requests, such as asking that all changes be marked or described. Although not required by our licenses, you are encouraged to respect those requests where reasonable. [More considerations for the public.](#) ▼

Creative Commons Attribution 4.0 International Public License

By exercising the Licensed Rights (defined below), You accept and agree to be bound by the terms and conditions of this Creative Commons Attribution 4.0 International Public License (“Public License”). To the extent this Public License may be interpreted as a contract, You are granted the Licensed Rights in consideration of Your acceptance of these terms and conditions, and the Licensor grants You such rights in consideration of benefits the Licensor receives from making the Licensed Material available under these terms and conditions.

Section 1 – Definitions.

- a. **Adapted Material** means material subject to Copyright and Similar Rights that is derived from or based upon the Licensed Material and in which the Licensed Material is translated, altered, arranged, transformed, or otherwise modified in a manner requiring permission under the Copyright and Similar Rights held by the Licensor. For purposes

-
- of this Public License, where the Licensed Material is a musical work, performance, or sound recording, Adapted Material is always produced where the Licensed Material is synched in timed relation with a moving image.
- b. **Adapter's License** means the license You apply to Your Copyright and Similar Rights in Your contributions to Adapted Material in accordance with the terms and conditions of this Public License.
 - c. **Copyright and Similar Rights** means copyright and/or similar rights closely related to copyright including, without limitation, performance, broadcast, sound recording, and Sui Generis Database Rights, without regard to how the rights are labeled or categorized. For purposes of this Public License, the rights specified in Section 2(b)(1)-(2) are not Copyright and Similar Rights.
 - d. **Effective Technological Measures** means those measures that, in the absence of proper authority, may not be circumvented under laws fulfilling obligations under Article 11 of the WIPO Copyright Treaty adopted on December 20, 1996, and/or similar international agreements.
 - e. **Exceptions and Limitations** means fair use, fair dealing, and/or any other exception or limitation to Copyright and Similar Rights that applies to Your use of the Licensed Material.
 - f. **Licensed Material** means the artistic or literary work, database, or other material to which the Licensor applied this Public License.
 - g. **Licensed Rights** means the rights granted to You subject to the terms and conditions of this Public License, which are limited to all Copyright and Similar Rights that apply to Your use of the Licensed Material and that the Licensor has authority to license.
 - h. **Licensor** means the individual(s) or entity(ies) granting rights under this Public License.
 - i. **Share** means to provide material to the public by any means or process that requires permission under the Licensed Rights, such as reproduction, public display, public performance, distribution, dissemination, communication, or importation, and to make material available to the public including in ways that members of the public may access the material from a place and at a time individually chosen by them.
 - j. **Sui Generis Database Rights** means rights other than copyright resulting from Directive 96/9/EC of the European Parliament and of the Council of 11 March 1996 on the legal protection of databases, as amended and/or succeeded, as well as other essentially equivalent rights anywhere in the world.
 - k. **You** means the individual or entity exercising the Licensed Rights under this Public License. **Your** has a corresponding meaning.

Section 2 – Scope.

- a. **License grant.**
 - 1. Subject to the terms and conditions of this Public License, the Licensor hereby grants You a worldwide, royalty-free, non-sub licensable, non-exclusive, irrevocable license to exercise the Licensed Rights in the Licensed Material to:
 - A. reproduce and Share the Licensed Material, in whole or in part; and
 - B. produce, reproduce, and Share Adapted Material.
 - 2. Exceptions and Limitations. For the avoidance of doubt, where Exceptions and Limitations apply to Your use, this Public License does not apply, and You do not need to comply with its terms and conditions.
 - 3. Term. The term of this Public License is specified in Section 6(a).
 - 4. Media and formats; technical modifications allowed. The Licensor authorizes You to exercise the Licensed Rights in all media and formats whether now known or hereafter created, and to make technical modifications necessary to do so. The Licensor waives and/or agrees not to assert any right or authority to forbid You from making technical modifications necessary to exercise the Licensed Rights, including technical modifications necessary to circumvent Effective Technological Measures. For purposes of this Public License, simply making modifications authorized by this Section 2(a)(4) never produces Adapted Material.
 - 5. Downstream recipients.
 - A. Offer from the Licensor – Licensed Material. Every recipient of the Licensed Material automatically receives an offer from the Licensor to exercise the Licensed Rights under the terms and conditions of this Public License.
 - B. No downstream restrictions. You may not offer or impose any additional or different terms or conditions on, or apply any Effective Technological Measures to, the Licensed Material if doing so restricts exercise of the Licensed Rights by any recipient of the Licensed Material.
 - 6. No endorsement. Nothing in this Public License constitutes or may be construed as permission to assert or imply that You are, or that Your use of the Licensed Material is, connected with, or sponsored, endorsed, or granted official status by, the Licensor or others designated to receive attribution as provided in Section 3(a)(1)(A)(i).

b. Other rights.

1. Moral rights, such as the right of integrity, are not licensed under this Public License, nor are publicity, privacy, and/or other similar personality rights; however, to the extent possible, the Licensor waives and/or agrees not to assert any such rights held by the Licensor to the limited extent necessary to allow You to exercise the Licensed Rights, but not otherwise.
2. Patent and trademark rights are not licensed under this Public License.
3. To the extent possible, the Licensor waives any right to collect royalties from You for the exercise of the Licensed Rights, whether directly or through a collecting society under any voluntary or waivable statutory or compulsory licensing scheme. In all other cases the Licensor expressly reserves any right to collect such royalties.

Section 3 – License Conditions.

Your exercise of the Licensed Rights is expressly made subject to the following conditions.

a. Attribution.

1. If You Share the Licensed Material (including in modified form), You must:
 - A. retain the following if it is supplied by the Licensor with the Licensed Material:
 - i. identification of the creator(s) of the Licensed Material and any others designated to receive attribution, in any reasonable manner requested by the Licensor (including by pseudonym if designated);
 - ii. a copyright notice;
 - iii. a notice that refers to this Public License;
 - iv. a notice that refers to the disclaimer of warranties;
 - v. a URI or hyperlink to the Licensed Material to the extent reasonably practicable;
 - B. indicate if You modified the Licensed Material and retain an indication of any previous modifications; and
 - C. indicate the Licensed Material is licensed under this Public License, and include the text of, or the URI or hyperlink to, this Public License.
2. You may satisfy the conditions in Section 3(a)(1) in any reasonable manner based on the medium, means, and context in which You Share the Licensed Material. For example, it may be reasonable to satisfy the conditions by providing a URI or hyperlink to a resource that includes the required information.
3. If requested by the Licensor, You must remove any of the information required by Section 3(a)(1)(A) to the extent reasonably practicable.
4. If You Share Adapted Material You produce, the Adapter's License You apply must not prevent recipients of the Adapted Material from complying with this Public License.

Section 4 – Sui Generis Database Rights.

Where the Licensed Rights include Sui Generis Database Rights that apply to Your use of the Licensed Material:

- a. for the avoidance of doubt, Section 2(a)(1) grants You the right to extract, reuse, reproduce, and Share all or a substantial portion of the contents of the database;
- b. if You include all or a substantial portion of the database contents in a database in which You have Sui Generis Database Rights, then the database in which You have Sui Generis Database Rights (but not its individual contents) is Adapted Material; and
- c. You must comply with the conditions in Section 3(a) if You Share all or a substantial portion of the contents of the database.

For the avoidance of doubt, this Section 4 supplements and does not replace Your obligations under this Public License where the Licensed Rights include other Copyright and Similar Rights.

Section 5 – Disclaimer of Warranties and Limitation of Liability.

-
- a. Unless otherwise separately undertaken by the Licensor, to the extent possible, the Licensor offers the Licensed Material as-is and as-available, and makes no representations or warranties of any kind concerning the Licensed Material, whether express, implied, statutory, or other. This includes, without limitation, warranties of title, merchantability, fitness for a particular purpose, non-infringement, absence of latent or other defects, accuracy, or the presence or absence of errors, whether or not known or discoverable. Where disclaimers of warranties are not allowed in full or in part, this disclaimer may not apply to You.
- b. To the extent possible, in no event will the Licensor be liable to You on any legal theory (including, without limitation, negligence) or otherwise for any direct, special, indirect, incidental, consequential, punitive, exemplary, or other losses, costs, expenses, or damages arising out of this Public License or use of the Licensed Material, even if the Licensor has been advised of the possibility of such losses, costs, expenses, or damages. Where a limitation of liability is not allowed in full or in part, this limitation may not apply to You.
- c. The disclaimer of warranties and limitation of liability provided above shall be interpreted in a manner that, to the extent possible, most closely approximates an absolute disclaimer and waiver of all liability.

Section 6 – Term and Termination.

- a. This Public License applies for the term of the Copyright and Similar Rights licensed here. However, if You fail to comply with this Public License, then Your rights under this Public License terminate automatically.
- b. Where Your right to use the Licensed Material has terminated under Section 6(a), it reinstates:
1. automatically as of the date the violation is cured, provided it is cured within 30 days of Your discovery of the violation; or
 2. upon express reinstatement by the Licensor.
- For the avoidance of doubt, this Section 6(b) does not affect any right the Licensor may have to seek remedies for Your violations of this Public License.
- c. For the avoidance of doubt, the Licensor may also offer the Licensed Material under separate terms or conditions or stop distributing the Licensed Material at any time; however, doing so will not terminate this Public License.
- d. Sections 1, 5, 6, 7, and 8 survive termination of this Public License.

Section 7 – Other Terms and Conditions.

- a. The Licensor shall not be bound by any additional or different terms or conditions communicated by You unless expressly agreed.
- b. Any arrangements, understandings, or agreements regarding the Licensed Material not stated herein are separate from and independent of the terms and conditions of this Public License.

Section 8 – Interpretation.

- a. For the avoidance of doubt, this Public License does not, and shall not be interpreted to, reduce, limit, restrict, or impose conditions on any use of the Licensed Material that could lawfully be made without permission under this Public License.
- b. To the extent possible, if any provision of this Public License is deemed unenforceable, it shall be automatically reformed to the minimum extent necessary to make it enforceable. If the provision cannot be reformed, it shall be severed from this Public License without affecting the enforceability of the remaining terms and conditions.
- c. No term or condition of this Public License will be waived and no failure to comply consented to unless expressly agreed to by the Licensor.
- d. Nothing in this Public License constitutes or may be interpreted as a limitation upon, or waiver of, any privileges and immunities that apply to the Licensor or You, including from the legal processes of any jurisdiction or authority.

Creative Commons is not a party to its public licenses. Notwithstanding, Creative Commons may elect to apply one of its public licenses to material it publishes and in those instances will be considered the "Licensor." The text of the Creative Commons public licenses is dedicated to the public domain under the [CC0 Public Domain Dedication](#). Except for the limited purpose of indicating that material is shared under a Creative Commons public license or as otherwise permitted by the Creative Commons policies published at creativecommons.org/policies, Creative Commons does not authorize the use of the trademark "Creative Commons" or any other trademark or logo of Creative Commons without its prior written consent including, without limitation, in connection with any unauthorized modifications to any of its public licenses or any

other arrangements, understandings, or agreements concerning use of licensed material. For the avoidance of doubt, this paragraph does not form part of the public licenses.

Creative Commons may be contacted at creativecommons.org.

Additional languages available: [Bahasa Indonesia](#), [eesti keel](#), [euskara](#), [Deutsch](#), [Español](#), [français](#), [hrvatski](#), [italiano](#), [latviski](#), [Lietuvių](#), [Nederlands](#), [norsk](#), [polski](#), [português](#), [suomeksi](#), [svenska](#), [te reo Māori](#), [Türkçe](#), [Ελληνικά](#), [русский](#), [українська](#), [العربية](#), [日本語](#). Please read the [FAQ](#) for more information about official translations.








Except where otherwise [noted](#), content on this site is licensed under a [Creative Commons Attribution 4.0 International license](#). [Icons](#) by The Noun Project.

[Contact](#) | [Privacy](#) | [Policies](#) | [Terms](#)

Paper: "Shear heating in creeping faults changes the onset of convection." Geophysical Journal International 211, no. 1 (2017): 270-283. DOI: 10.1093/gji/ggx295

Authors: Ms. R. Tung (Curtin University, Australia)
 Dr. T. Poulet (CSIRO, Australia)
 Dr. S. Alevizos (UNSW, Australia)
 Dr. E. Veveakis (UNSW, Australia)
 Prof K. Regenauer-Lieb (UNSW, Australia)

Co-author	Conception and design	Literature review	Experimental methods and data acquisition / generation	Analysis of results and discussion	Paper writing and editing
Ms. R Tung	x	x	x	x	x
I acknowledge that these represent my contribution to the above research output.					
 Signature					
Dr. T. Poulet	x	x	x	x	x
I acknowledge that these represent my contribution to the above research output.					
 Signature					
Dr. S. Alevizos		x	x	x	x
I acknowledge that these represent my contribution to the above research output.					
 Signature					
Dr. E. Veveakis	x		x	x	
I acknowledge that these represent my contribution to the above research output.					
 Signature					
Prof K. Regenauer-Lieb	x			x	x
I acknowledge that these represent my contribution to the above research output.					
 Signature					